New Applications That Come From Extending Seismic Networks Into Buildings

Thesis by
Ming Hei Cheng

In Partial Fulfillment of the Requirements for the degree
of
Doctor of Philosophy

CALIFORNIA INSTITUTE OF TECHNOLOGY
Pasadena, California
2014
(Defended February 26, 2014)

ACKNOWLEDGEMENT

First, I would like to acknowledge my PhD research advisor, Prof. Thomas Heaton, for his support and valuable guidance throughout all my years at Caltech. I would always gain new insights on the topics that I discussed with him. His out-of-the-box thinking always drives me to drill deep into problems for innovative solutions.

I want to express my sincere gratitude to Prof. James Beck, Prof. Mani Chandy, Prof. Robert Clayton, Dr. Robert Graves, Prof. John Hall, Dr. Monica Kohler, and Dr. Swami Krishnan. I learned a lot from them, from seismology to structural engineering, to applied mathematics, and to computer science. My thesis could not be completed without their collaborations. I also want to thank my undergraduate research advisor, Dr. Ray Su, for introducing me to the research world.

Special thanks to the Croucher Foundation, the Fred L. Hartley Family Foundation, the Moore Foundation, and the National Science Foundation for their generous support on my research. Thank you to all the team members in the CSN project, including Julian Bunn, Matt Faulkner, Richard Guy, Annie Liu, Michael Olson, and Leif Strand. I will never forget our sensor assembling parties. Thank you the administrative staff in Thomas Building, including Cheryl Geer, Carolina Oseguera, and Christine Silva. Also, my life would be totally different without my fellow graduate students in the MCE department, including In-Ho Cho, Vanessa Heckman, Andrea Leonard, Ramses Mourhatch, Shi-Yan Song, Hemanth Siriki, Daniel Sutoyo, and Stephen Wu.

Finally, the understanding and encouragement of my family helped me a lot to work through the years and pursue my goals. I want to express my deepest gratitude to my mother (Michelle) and my grandmother (Shuet-Chun) for their support.

ABSTRACT

This thesis describes engineering applications that come from extending seismic networks into building structures. The proposed applications will benefit the data from the newly developed crowd-sourced seismic networks which are composed of low-cost accelerometers. An overview of the Community Seismic Network and the earthquake detection method are addressed. In the structural array components of crowd-sourced seismic networks, there may be instances in which a single seismometer is the only data source that is available from a building. A simple prismatic Timoshenko beam model with soil-structure interaction (SSI) is developed to approximate mode shapes of buildings using natural frequency ratios. A closed form solution with complete vibration modes is derived. In addition, a new method to rapidly estimate total displacement response of a building based on limited observational data, in some cases from a single seismometer, is presented. The total response of a building is modeled by the combination of the initial vibrating motion due to an upward traveling wave, and the subsequent motion as the low-frequency resonant mode response. Furthermore, the expected shaking intensities in tall buildings will be significantly different from that on the ground during earthquakes. Examples are included to estimate the characteristics of shaking that can be expected in mid-rise to high-rise buildings. Development of engineering applications (e.g., human comfort prediction and automated elevator control) for earthquake early warning system using probabilistic framework and statistical learning technique is addressed.

TABLE OF CONTENTS

LIST OF FIGURES

LIST OF TABLES

Chapter 1

INTRODUCTION

A new crowd-sourced seismic network, namely the Community Seismic Network (CSN), is currently being developed at the California Institute of Technology in the United States. This network aims to provide a dense array of low-cost accelerometers whose data can be sent via the Internet to a cloud-based center. The goal of this project is to measure ground and building shaking at a large scale of sites in urban areas. The recorded data can be used to provide emergency response information in the case of large earthquakes as well as to study the Earth's structure and the earthquake process. When deployed in buildings, the network can be used to monitor their state of health. Chapter 2 presents an overview of the network and the earthquake detection method.

In the structural array components of crowd-sourced seismic networks, there may be instances in which a single seismometer is the only data source that is available from a building. Chapter 3 presents a simple prismatic Timoshenko beam model with soil-structure interaction (SSI) to approximate the dynamic linear elastic behavior of buildings. A closed form solution with complete vibration modes is derived. It is demonstrated that building properties, including mode shapes, can be estimated from the knowledge of the natural frequencies of the first two translational modes in a particular direction and the building dimensions. In many cases, the natural frequencies of the first two vibrational modes of a building can be determined from data recorded by a single seismometer. If the ground excitation is available, the building's total vibration response can then be simulated by appropriate modal summation. Preliminary analysis is performed on Caltech's Millikan Library, which has significant bending deformation since it is much stiffer in shear.

Chapter 4 presents a new method to rapidly estimate total displacement response of a building based on limited observational data, in some cases from a single seismometer. The total response of a building is modeled by the combination of the initial vibrating motion due to an upward traveling wave, and the subsequent motion as the low-frequency resonant mode response. It is demonstrated that resonant mode response alone may not adequately capture the full building response and that a transient traveling wave comprises a significant part of the total response. This study builds upon the mode shape estimation technique developed in Chapter 3. Seismic records from a 54-story building in downtown Los Angeles and dynamic response computations using a finite-element model of the 17-story Factor building at UCLA are used to verify the method. Also, numerical results demonstrate how the relative significance of the traveling wave component of building response is dependent on the frequency content of the input excitation.

Chapter 5 presents the development of engineering applications in earthquake early warning system using a probabilistic framework with statistical learning techniques. In California, an earthquake early warning system is currently being tested as part of the California Integrated Seismic Network (CISN). The system aims to provide warnings in seconds to tens of seconds prior to the occurrence of ground shaking at a site; since the system broadcasts the location and time of the earthquake, user software can estimate the arrival time and intensity of the expected S-wave. However, the shaking experienced by a user in a tall building will be significantly different from that on the ground. Examples are included to estimate the characteristics of shaking that can be expected in mid-rise to high-rise buildings. Potential engineering applications (e.g., human comfort prediction and automated elevator control) for buildings in earthquake early warning system are addressed.

Future work and a summary of the contributions of this thesis are presented in Chapters 6-7.

Chapter 2

COMMUNITY SEISMIC NETWORK

Community seismic network (CSN), a new earthquake monitoring system, is composed of a dense array of low-cost acceleration sensors. The data is sent via the Internet to a cloud-based center. The design of the network aims to produce the following products: rapid detailed shake map that shows maximum acceleration on a block-by-block scale; detailed subsurface map which concludes subsurface structures and soil conditions that enhance ground shaking; images of fault rupture showing slip propagation along the fault during an earthquake; structural health monitoring that accesses the structural integrity of buildings or bridges after earthquakes; and earthquake early warning which provides rapid warnings based on early detection of ground shaking. In this chapter, an overview of the network and the earthquake detection method is presented.

2.1 CSN SENSOR

The current CSN sensors are produced by Phidgets Inc. (http://www.phidgets.com) (Figure 2.1). The sensors have an analog-to-digital converter resolution of 16-bit and a maximum acceleration measurement of +/- 2g. Table 2.1 compares the characteristics of the CSN sensor with other instruments, including the accelerometer in an Android smartphone produced in 2010 and the high quality 24-bit Episensor seismometer. On June 8th, 2011, the noise level of a CSN sensor and an Episensor (station PASC in the Southern California Seismic Network) were measured in the USGS Pasadena vault. The place was chosen because it was easily accessible and

quiet enough to examine the instrumental noise without considerable disturbance from the surrounding environment. Comparison of the noise envelopes is included in Figure 2.2.

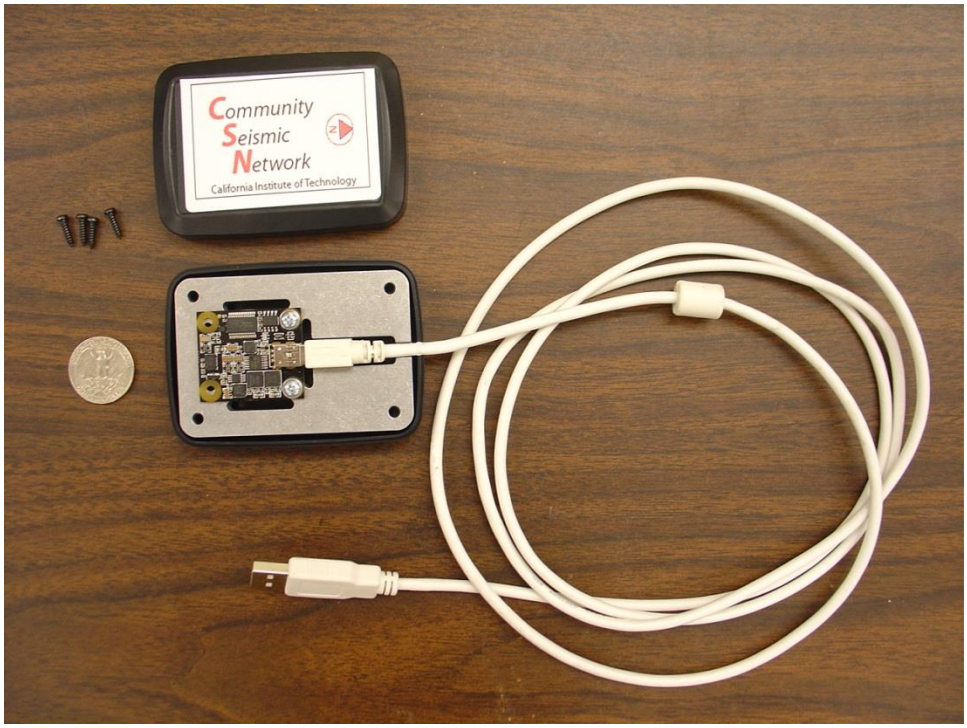

Figure 2.1: CSN accelerometer.

Table 2.1: Characteristics of different instruments.

	Clipping Level	Digitizer	Noise Level*	Dynamic Range	Sampling Rate
CSN Phidgets	2g	16bits	~2.8×10^{-4}g	77.1dB (7.1×10^{3})	250Hz (constant)
Android Phone produced in 2010	8g	14bits	~6×10^{-3}g	62.1dB (1.3×10^{3})	~90Hz
Episensor	2g	24bits	~3.9×10^{-7}g	133.7dB (5.1×10^{6})	200Hz (constant)

*Noise level is defined by the root mean square (rms) of the ambient noise data.

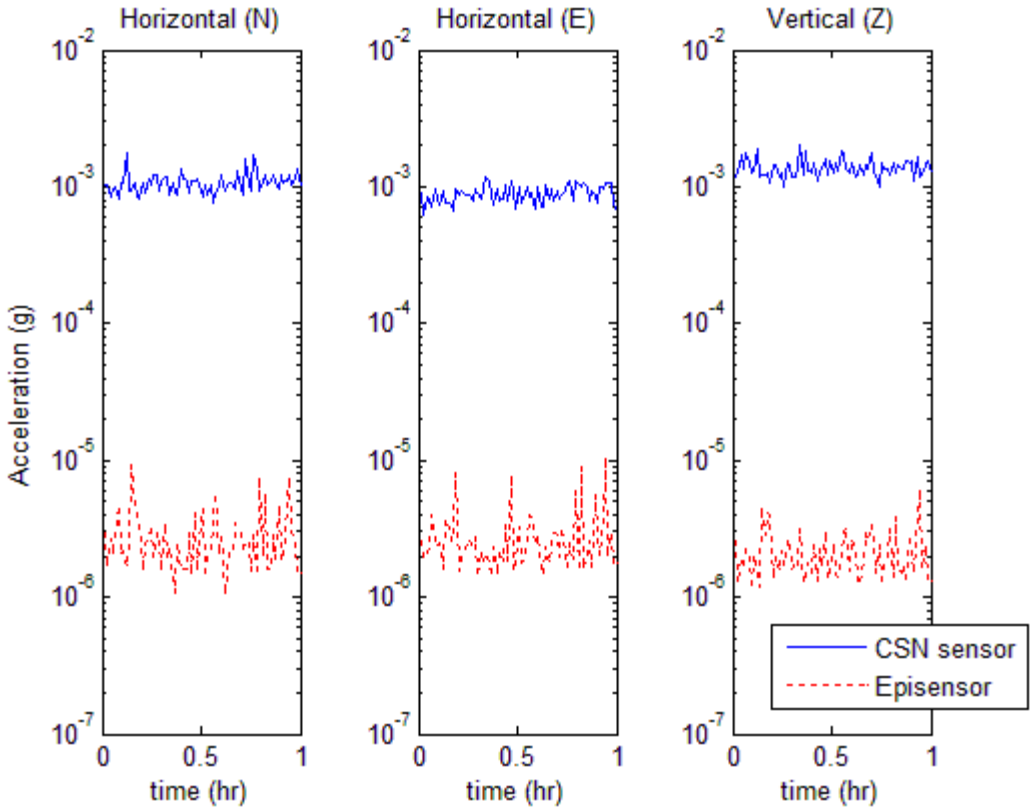

Figure 2.2: Comparison of noise envelope between a CSN sensor and an Episensor in the USGS Pasadena vault. (Log scale on the y-axis).

Each CSN sensor is connected to a computer by a USB cable. The CSN sensor is made up of a microelectromechanical systems (MEMS) device, which takes power via the USB cable. In such case, the quality of the USB port on a connecting computer has significant impact on the instrumental noise level of the CSN sensor. With two CSN sensors placed on a stationary table in the laboratory at Caltech, a comparison was made of the noise level between a sensor connected to a generic 10" netbook and another sensor connected to a 15" IBM laptop. Figure 2.3 shows that the CSN sensor connected to the generic netbook has additional induced noise. Based on some experiments, it was concluded that this problem was generated by the connecting computer and that it can be solved by using a USB cable with external power supply.

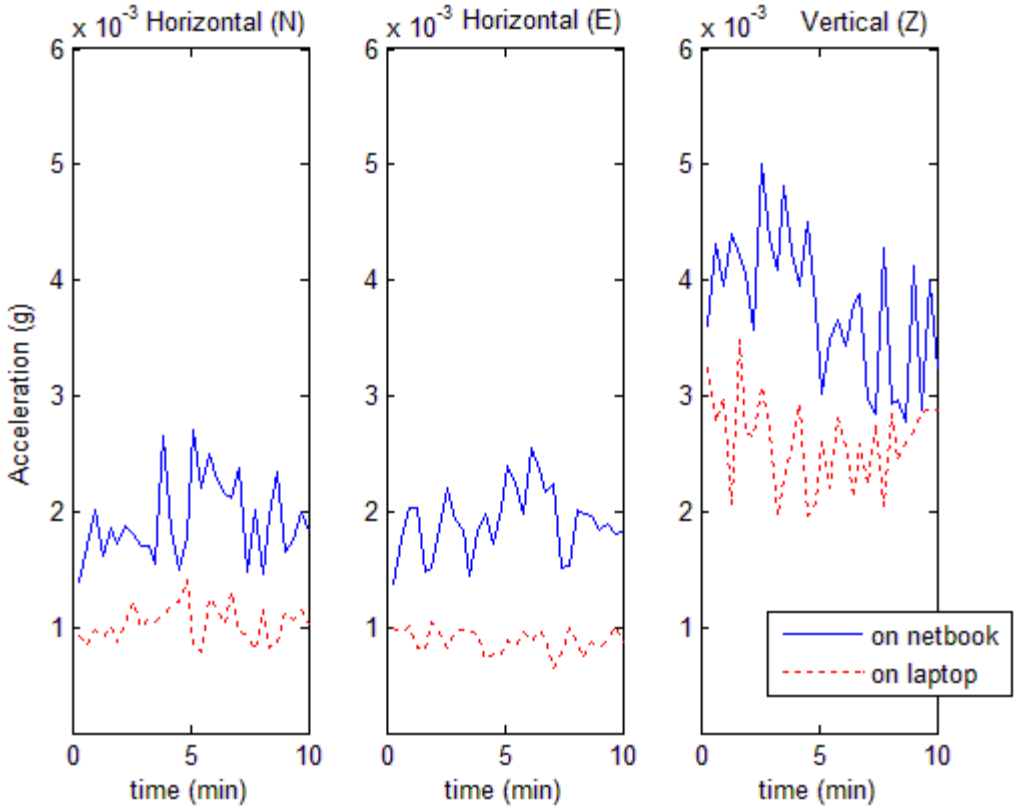

Figure 2.3: Comparison of ambient noise envelope between a CSN sensor connected to a generic netbook and another sensor connected to a 15" IBM laptop in the laboratory. The problem of additional induced noise can be solved by using a USB cable with external power supply.

2.2 EXTRACTING NATURAL FREQUENCIES OF BUILDINGS

In this section, CSN sensors are shown to be capable of extracting the natural frequencies of buildings. Caltech's Millikan Library (Figure 2.4) is a nine-story reinforced-concrete building with one level of basement embedded in stiff soil whose shear wave velocity is about 300m/s. The building has both moment resisting frames as well as a very stiff core-wall in both the NS and EW directions. More details can be found in Section 3.3. On August 5th, 2010, a 10-hour time history of ambient vibration acceleration data was recorded using a CSN sensor placed on the 9th floor of

Millikan Library. By a peak-picking method, the fundamental natural frequencies of Millikan Library during the experiment were determined as 1.2Hz in the EW direction and 1.75Hz in the NS direction (Figures 2.5-2.6). These values match with the ambient vibration frequencies reported in the literature for this building (see Section 3.3).

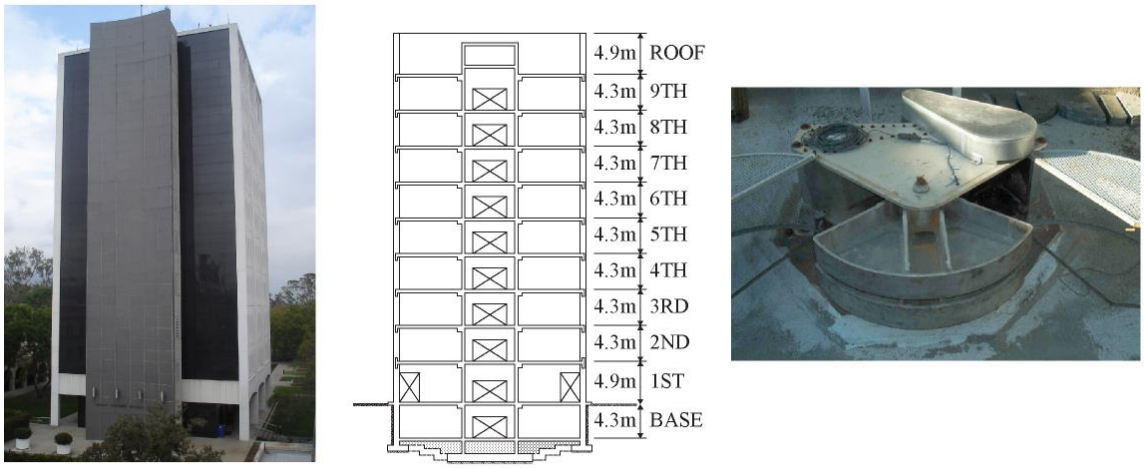

Figure 2.4: Millikan library profile and shaker on the roof (from Bradford, 2006).

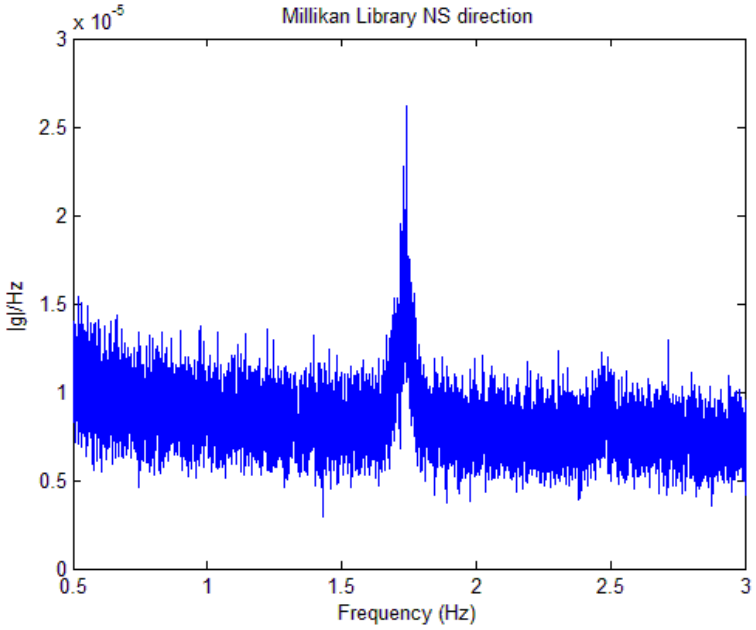

Figure 2.5: Fourier spectrum (NS direction) of a 10-hour acceleration record from a CSN sensor on the 9th floor of Millikan Library under ambient vibration.

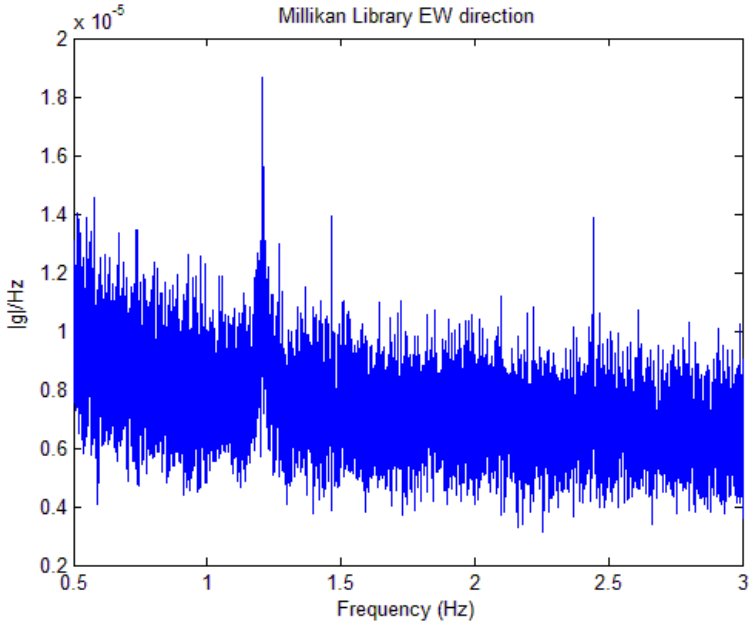

Figure 2.6: Fourier spectrum (EW direction) of a 10-hour acceleration record from a CSN sensor on the 9th floor of Millikan Library under ambient vibration.

2.3 CORRECT TIME STAMP ERROR

During the September 1st, 2011 M4.2 Newhall, California earthquake (epicentral distance of 39.2 km), eight CSN sensors were running on some public computers in Millikan Library for prototype building monitoring. The sensors were located at the basement, 1st, 2nd, 3rd, 6th, 7th, 8th and 9th floors. Although this is in general a reliable way to obtain time accuracy to within 100msec, it is found that occasionally time synchronization errors appear in the earthquake records and the seismic data becomes incoherent. This problem occurred for the 2011 Newhall earthquake records, and was reflected in widely varying time lags between different floors for the propagating wave. Since the total time difference between floors is made up of the wave travel time (as a function of average shear-wave velocity) and the time stamp error, one way to resolve the problem is to use the property of the building's fundamental vibrating modes.

Vibrating motions of a building are in-phase when the building is excited in its fundamental natural frequency. To obtain the fundamental modal response of Millikan Library, a fourth-order Butterworth band-pass filter with corner frequencies at 1.58Hz and 1.78Hz was applied to the NS data, and a filter with corner frequencies at 1.08Hz and 1.28Hz was applied to the EW data. A Hilbert transform was applied to find the envelope of the filtered data, and cross-correlation is used to calculate the time stamp error of all the floors relative to the 9th floor. The results are presented in Table 2.2. The cross-correlation result of the filtered time series for any single sensor in the NS direction should match with the corresponding one in the EW direction, since they are all stamped by the same clock. This condition is necessary in identifying the time offset.

The method presented here primarily applies to the data from the 6th and higher floors during the 2011 Newhall earthquake. Note that no data were available from the 3rd to 5th floors due to a system error. Since the building response of lower floors was weak and the earthquake was a

broadband excitation, the coherent fundamental response did not show up on the 2nd and lower floors. An approximation using a constant shear-wave velocity is adopted to address the time stamp error in the lower floors. The earthquake response in Millikan Library was also captured by the Southern California Seismic Network station MIK which is located on the ceiling of the 9th floor and station MIKB which is located in the basement. The roof and basement data streams were GPS time synchronized. A fourth-order high-pass Butterworth filter with a corner frequency at 2.5Hz was applied to the data to remove the fundamental mode effect. A Hilbert transform was used to find the envelope of the filtered data, and cross-correlation was applied to estimate the shear-wave travel time from basement to roof. The wave travel time is 0.26sec and the building height is about 44m, so the wave velocity is determined as 169m/s. This is different from the shear-wave velocity of 322m/s found by Snieder and Safak (2006) because their deconvolved wave impulses include the fundamental modes. Figure 2.7 shows the adjusted acceleration time series of Millikan Library in the NS direction during the Newhall earthquake. Other effects, such as measurement noise and non-linearity in the concrete shear wall running along the NS direction, could cause a difference in the time lag between the NS and EW directions. Here, the average of the two values is adopted. The time adjustments for all floors relative to the 9th floor are shown in Table 2.2.

Table 2.2: Time (sec) adjustments for CSN data.

Fundamental mode cross-correlation

	Base	1/F	2/F	6/F	7/F	8/F	9/F
NS	0.56	4.16	-0.14	-0.14	-0.1	-0.14	0
EW	5.54	5.44	0.96	-0.16	-0.12	-0.16	0
Difference	4.98	1.28	1.1	0.02	0.02	0.02	-
Chosen value	-	-	-	-0.16	-0.12	-0.16	0

High-pass filtered cross-correlation

	Base	1/F	2/F
NS	-0.34	-0.1	-0.26
EW	0.06	-0.08	-0.28
Difference	0.4	0.02	0.02
Chosen value	-0.14	-0.08	-0.28

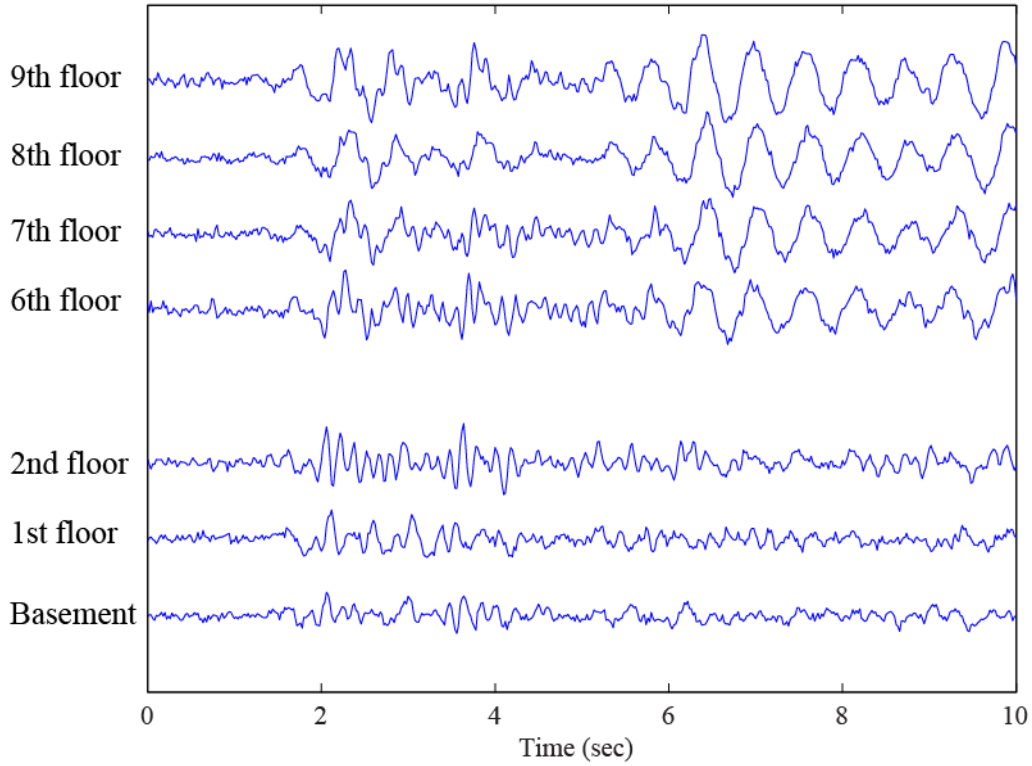

Figure 2.7: Adjusted acceleration time series in the NS direction for the 2011 M4.2 Newhall earthquake recorded by the CSN array in Millikan Library.

2.4 EARTHQUAKE DETECTION

In this section, seismic energy of the data recorded by CSN sensors is shown to be concentrated in certain frequency band. The earthquake detection algorithm can be improved using this information. As of February 2014, most of the CSN sensors are distributed in Pasadena, California area (Figure 2.8). The current earthquake detection algorithm used in the CSN network is based on event-picking from individual stations. An event-pick is issued when the short term acceleration mean exceeds k standard deviations of the long term acceleration mean. The value k = 1.5 is currently used. More details can be found in Olson (2014). Mean μ_l and standard deviation σ_l are

determined from the long term acceleration with an interval of 10sec. The end value of the 10-second interval can influence the following 0.5sec, and so a 1-second gap is placed after the 10-second interval. Mean μ_s is determined from the short term acceleration with an interval of 0.5sec.

Figure 2.8: CSN sensor locations (as of February 2014).

Mathematically, an event-pick is issued when:

$$\mu_s \geq \mu_l + k\,\sigma_l \tag{2.1}$$

Figures 2.9-2.11 show the frequency content of the acceleration records from a CSN station (station number 171 is picked as an example). The sampling rate of the sensor is 50 samples per second, and the Nyquist frequency is 25Hz. Frequency content is defined as the proportion of Fourier spectral energy in the corresponding frequency bucket. Frequency buckets of 0-2Hz, 2-4Hz,

4-6Hz, 6-8Hz, 8-10Hz and 10-25Hz are considered. If a uniform spectrum is considered, the frequency content is 0.08 (= 2/25) for all the frequency buckets, except 0.6 (= 15/25) for the 10-25Hz bucket. Fourier spectral energy is calculated using FFT on a 30-second acceleration time series. Some 30-second data is queried from the CSN network every two hours for ambient vibration samples; four weekdays (August 1st, 2nd, 5th and 6th, 2013) and a weekend (August 3rd and 4th, 2013) are selected. Five earthquakes recorded by the CSN in 2012 are also selected in this study (Table 2.3), and the first 30-second of each earthquake is used to calculate the Fourier spectral energy.

Table 2.3: Five earthquakes recorded by CSN in 2012.

Date	Magnitude	Location
June 14th, 2012	4.0	Yorba Linda, California
August 8th, 2012	4.5	Yorba Linda, California
August 8th, 2012	4.3	Yorba Linda, California
August 29th, 2012	4.1	Yorba Linda, California
October 28th, 2012	3.9	Newhall, California

No major difference is observed in the frequency content distribution between the data from weekdays and weekends. Data from the two horizontal components (North direction and East direction) of CSN sensors suggests that spectral energy concentrates in 4-10Hz during earthquakes, while it is more or less uniform during ambient periods. However, such observation does not apply to the vertical component. Let's focus on the two horizontal components in this study. Let μ_e be the mean of the frequency content during earthquakes; μ_0 and σ_0 be the mean and standard deviation of the frequency content during ambient periods. Figure 2.12 shows the statistical test result on $(\mu_e - \mu_0) / \sigma_0$ among all the 167 CSN sensors. These stations are currently operating in the network, and they have recorded all five earthquakes in Table 2.3. Almost all of

the stations give positive values on the test statistic, giving the conclusion that spectral energy concentrates in 4-10Hz during earthquakes. `

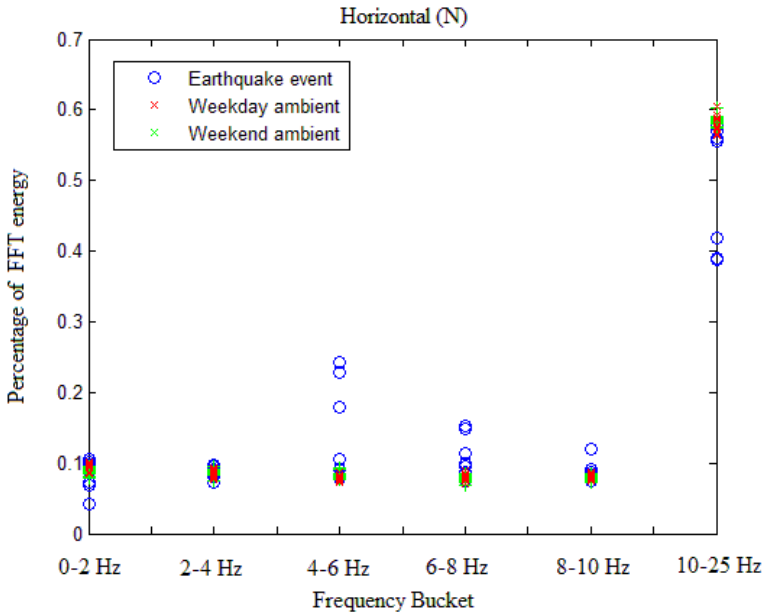

Figure 2.9: Comparison of frequency content on the horizontal component (North direction) of a CSN sensor between earthquakes and ambient periods.

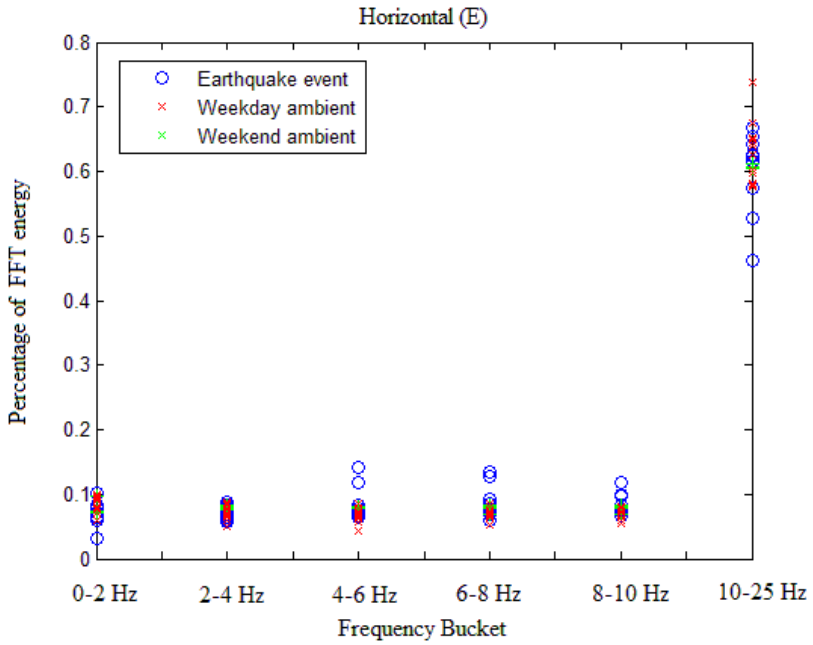

Figure 2.10: Comparison of frequency content on the horizontal component (East direction) of a CSN sensor between earthquakes and ambient periods.

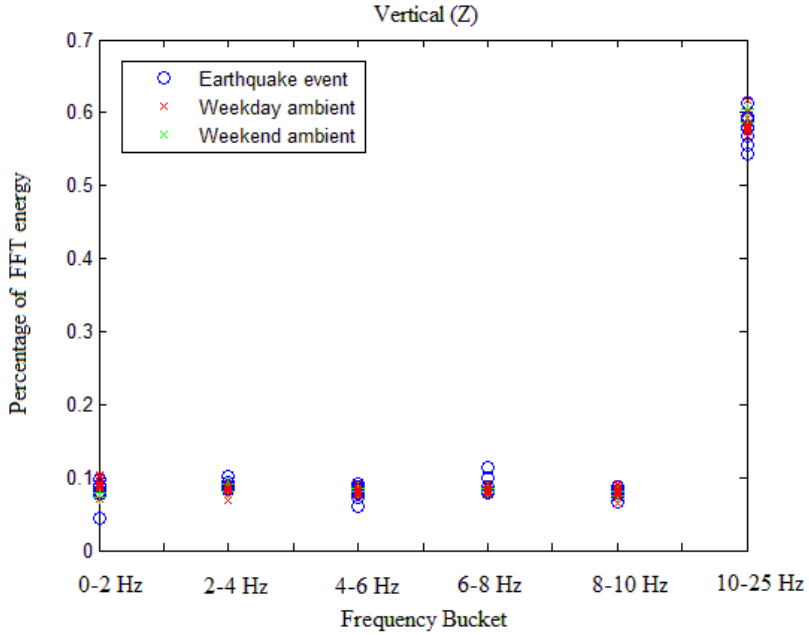

Figure 2.11: Comparison of frequency content on the vertical component of a CSN sensor between earthquakes and ambient periods.

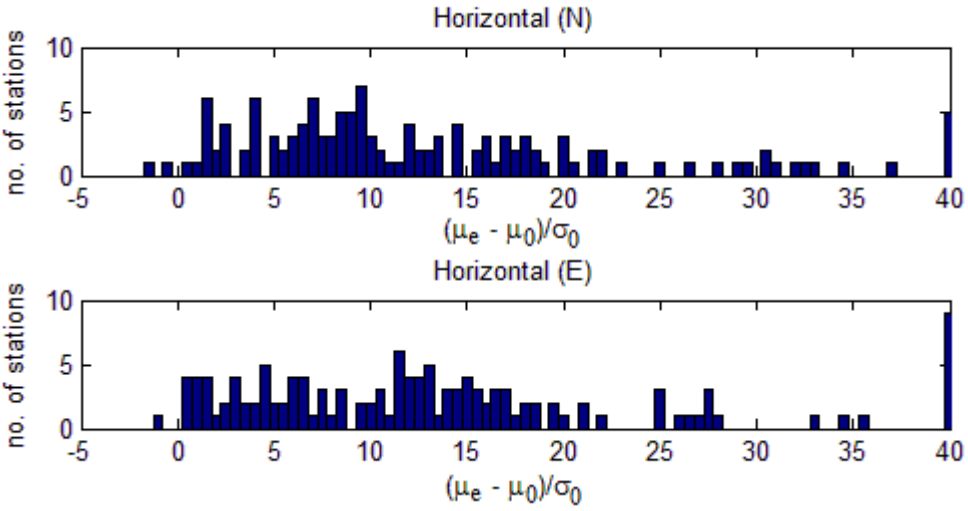

Figure 2.12: Statistical test on the 4-10Hz frequency content in CSN stations. μ_e is the mean of frequency content during earthquakes; μ_0 and σ_0 are the mean and standard deviation of the frequency content during ambient periods.

Spectrum analysis depends on time resolution of the recorded data. In other words, a certain amount of time length is needed for the spectral frequency concentration to occur. However, from the perspective of earthquake early warning, we wish to detect earthquakes as soon as they occur. To compensate for the time delay issue in spectrum analysis, a 4-10Hz band-pass filter is used to facilitate the development of a real-time earthquake detection algorithm. There were 214 CSN stations operating during the July 24th, 2013 M4.3 Weldon earthquake. Figure 2.13a shows the event-picks based on the original time series using Equation 2.1. Theoretically, the P-wave oscillates vertically and the S-wave oscillates horizontally, when seismic waves travel from the inner Earth. The P-wave is expected to show up mainly in the vertical component of a seismic station, while the S-wave is expected to show up mainly in the two horizontal components of a seismic station. Here, the P-wave is hardly detected from the unmodified time series and the S-wave is marginally observed at time = 43sec in the plot. Figure 2.13b shows the event-picks after a 4-10Hz band-pass filter has been applied. The S-wave is clearly observed at time = 43sec and

an indication of the P-wave has been detected at time = 27sec. Most of the CSN sensors are distributed in the Pasadena, California area, and the average epicentral distance is about 148 km. Based on the wave detection time, the P-wave velocity can be estimated as 148km / 27sec = 5.5km/s; while the S-wave velocity can be estimated as 148km / 43sec = 3.4km/s. The improvement in earthquake detection may be due to the local site effect or the transformed energy content by soil-structure interaction since most of the CSN sensors are installed in buildings and houses. Sutoyo (2009) documented that fundamental natural frequency of wood-frame buildings was in the range of 3Hz to 9Hz. Further investigation is needed to understand the energy concentration in the range of 4-10Hz.

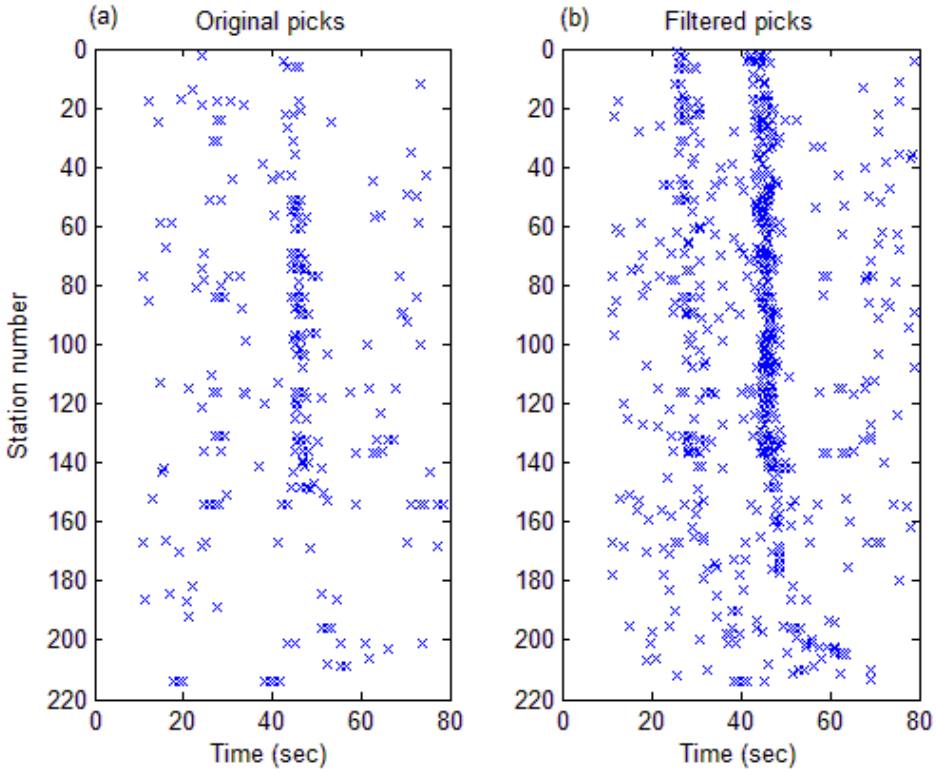

Figure 2.13: Event picks based on horizontal components of CSN stations during the 2013 M4.3 Weldon earthquake.

Figure 2.14 shows the approximate magnitude and distance envelope for signal detection by seismic instruments with digitizers designed to clip at 2g, assuming records with peak amplitude of 10 digital counts will be observed. Each envelope in the plot is a constant acceleration contour corresponding to 10 digital counts of the instrument. The plot provides us with a preliminary idea on the relation between minimum magnitude and maximum epicentral distance for observable earthquakes. The ground motion attenuation equation for soil sites by Cua (2005) is used to relate the magnitude and epicentral distance from root-mean-squared (rms) horizontal ground acceleration. Recorded seismic data is expected to be meaningful for geophysical analysis (e.g. to determine arrival time and seismic phase information) if the observed peak ground acceleration during earthquake is at least five times larger than the ambient noise level. With such criterion, CSN records for the five earthquakes in 2012 are included in Figure 2.14.

Possible future developments include the implementation of a band-pass filter in earthquake early warning using Geocells. Geocells are cells that divide a region through corresponding latitude and longitude pairs. An event is claimed in a Geocell if the number of event-picks (from individual stations) exceeds a certain threshold. Such a method can enhance the confidence in event detection using the low-quality data from low-cost sensors. More details about event detection using Geocells can be found in Olson (2014).

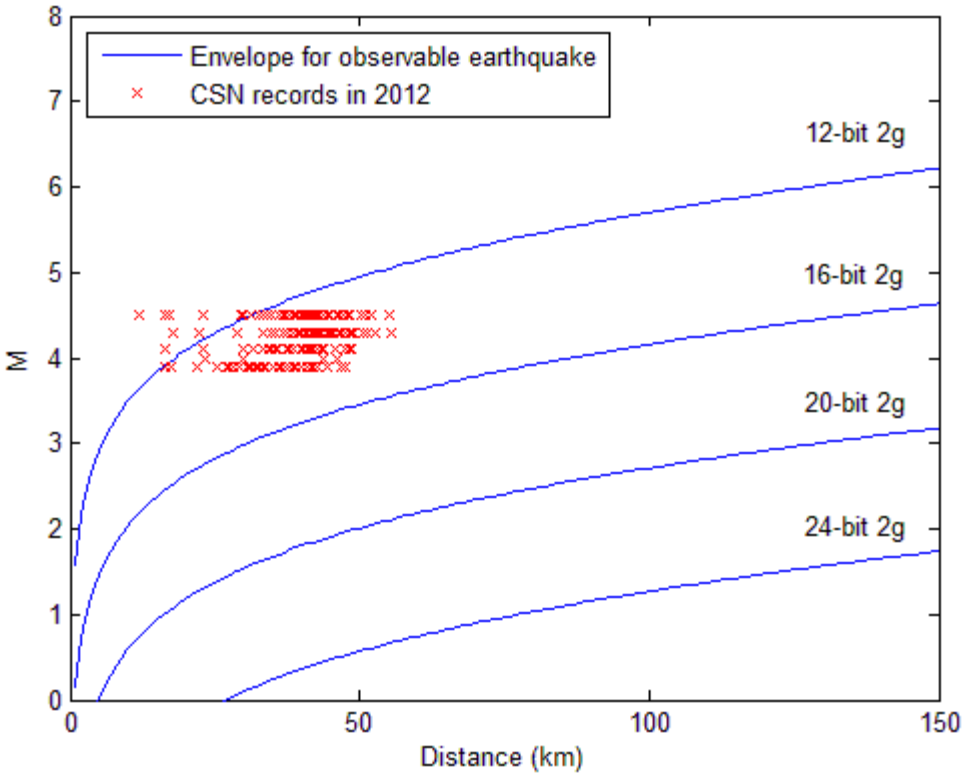

Figure 2.14: Magnitude and epicentral distance envelope for observable earthquakes, assuming records with peak amplitude of 10 digital counts will be observed. Ground motion attenuation equation for soil sites by Cua (2005) is used.

C h a p t e r 3

SIMULATING BUILDING MOTIONS USING NATURAL FREQUENCY RATIOS

Cheng, M. H. and T. H. Heaton, 2013. Simulating building motions using the ratios of its natural frequencies and a Timoshenko beam model, Earthquake Spectra, in press, DOI: http://dx.doi.org/10.1193/011613EQS003M.

The use of seismic data in buildings to study the deformations of a structure is a well-established study area in earthquake engineering (e.g. Skolnik et al., 2006; Kohler et al., 2007; Krishnan and Muto, 2013). Ideally, several stations are established in locations that can best describe the spatial/temporal pattern of building motions. However, a new type of seismic network is under development; these are the crowd-sourced seismic networks where volunteers install the seismometers. The Quake Catchers Network (Cochran et al., 2011) and the Community Seismic Network (Clayton et al., 2011) are examples. In a crowd-sourced network, station locations are typically chosen for reasons that are unrelated to the optimal design of a seismic network. In particular, there may be instances in which a single seismometer is the only data source that is available from a building. Furthermore, it may not be practical to construct a detailed finite-element model of the building; even if there were sufficient resources to construct a dynamic model, the structural design of the building may not be available. However, if the geometry of the building is known (e.g. obtained from Google Earth), then it may be feasible to infer the approximate deformations of the building using only a single seismic station. That is, seismologists have inferred the radial structure of the Earth using models that predict natural frequencies of the normal modes of the Earth (e.g. He and Tromp, 1996; Rosat et al., 2007; and Romanowicz et al., 2008). These frequencies are the same at all stations; that is, knowledge of the modal frequencies recorded at a single station is sufficient to infer the radial properties of a spheroid. In this chapter, a simple

methodology for obtaining the approximate motions of a building based on at least one seismogram and knowledge of the building geometry (especially the height) is presented.

Although buildings primarily consist of structural members (columns, walls, floors, etc.) separated by void spaces (rooms, doors, windows, etc.), the large scale deformation of the structure can often be approximately described by an equivalent homogeneous elastic continuum. In particular, many aspects of building motions can be understood in the context of a simple cantilevered elastic beam on an elastic half-space (i.e., the Earth). The strains that develop at the interface between the beam and the interface are quite complex. Fortunately, it has been possible to develop several methodologies to approximately model the mechanics of a cantilevered beam. The simplest approximation is to consider a beam that responds only in shear (e.g. Westergaard, 1933; Jennings and Newmark, 1960; and Iwan, 1997). This is often referred to as a shear beam. The shear beam is basically the same problem as a uniform layer on a half-space that is subject to only horizontal shear tractions. The effective density of the building can be simply calculated from an estimate of the building mass and total volume. The effective shear wave velocity in the building is $4Lf_1$, where L is the building height and f_1 is the frequency of the 1st mode (fundamental).

As a beam becomes very narrow compared to its length, the deformation primarily occurs as bending, that is, contraction on one side of the beam and extension on the opposite side. There is considerable knowledge of the technical theory of bending, which relates bending moment on a beam to the bending displacements of the beam. If shear deformations are negligible, then a beam can be simulated using the Bernoulli-Euler equation, which relates fourth order spatial derivatives of horizontal deflections to horizontal forces and inertial accelerations (e.g. Foutch and Jennings, 1978). Unlike shear waves, which have frequency independent wave velocities, bending waves are inherently dispersive; higher frequencies have higher wave speeds. While inter-story shearing

(Figure 3.1a) is the primary deformation mode of buildings that are wide compared to their height, tall and skinny buildings may experience significant bending (Figure 3.1b). This is especially true if the building has high shear stiffness, which is the case of Caltech's Millikan Library, a building with extensive shear walls. Models ignoring the effect of flexural deformation may cause noticeable errors. However, pure flexural models are rarely appropriate, even for buildings with high effective rigidity, e.g., shear walls as the main lateral load-resisting systems (Miranda, 1999). In reality, a building deforms in a mixture of flexural and shearing deflections (Figure 3.1c).

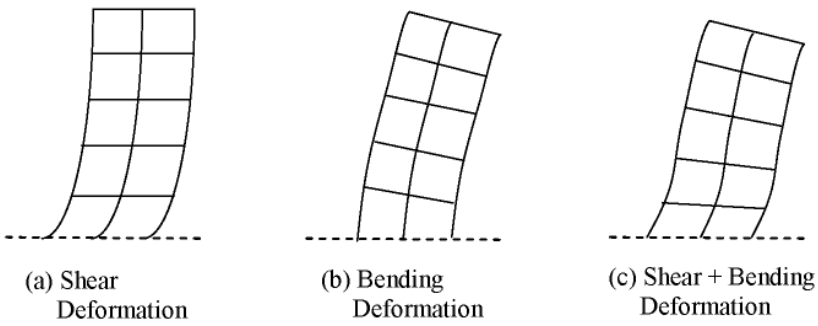

Figure 3.1: Building deformation. (a) Shear-beam type behavior (vertically propagating SH-waves) is expected when shear stiffness is less than flexural stiffness. (b) Bending-beam behavior (Bernoulli-Euler beam equation) is expected for tall and narrow buildings (small flexural stiffness). (c) Combined shearing and bending known as a Timoshenko beam.

Due to the deficiencies of simple pure-shear or pure-flexural models, researchers started using more complex models that incorporated more general building response. In particular, a Timoshenko beam (Timoshenko, 1937; Timoshenko and Goodier, 1951; Heidebrecht and Smith, 1973; and Rahgozar et al., 2004) is a computational model with differential equations coupling the effects of a shear beam and a bending beam, with the constraint that the total deflections are caused

by the sum of the shear deformations and the flexural deformations. Miranda (1999) used a continuum structural model consisting of a flexural cantilever beam and flexural shear beam to predict deformations in buildings. Miranda assumed the particular case of a Timoshenko beam model for which the roof deformations from flexure and shear are equal. Boutin et al. (2005) and Michel et al. (2006) suggested that mode shapes could be retrieved from the ratio of the first two natural frequencies of a building using a fixed-base Timoshenko beam model, but they have ignored section rotation inertia and soil-structure interaction. Soil-structure interaction could significantly affect the natural frequencies of a building. A simple consideration of the first two recorded natural frequencies of the system may lead to the misinterpretation of the properties of a fixed-base Timoshenko beam. Dynamic Timoshenko beam models are used in other engineering applications. For example, they are widely applied in the simulation of micro- or nano-beams (e.g. Hsu et al., 2007 and Wang et al., 2007).

In this chapter, a simple prismatic Timoshenko beam model with soil-structure interaction (SSI) is developed to approximate the dynamic linear elastic behavior of the buildings. A closed form response solution with complete vibration modes is derived. Once the dimensions of the building are specified, then the building properties, including mode shapes, can be derived by knowing the ratios of the frequencies of the first two normal modes in a particular direction. In many instances, the natural frequencies of the first two vibrational modes of a building can be identified by spectral analysis of data from a single seismometer. If the modes and mode shapes are known, the excitation of each mode can be determined from the analysis of a single building record. The entire spatial/temporal building vibration response can then be approximated by the appropriate modal summation. Preliminary analysis is performed on the Caltech's Millikan Library, which has high shear stiffness and consequently bending comprises a significant part of the overall deformation.

3.1 TIMOSHENKO BEAM WITH SOIL-STRUCTURE INTERACTION

A multi-story building can be modeled as an equivalent prismatic homogeneous Timoshenko beam with SSI, as shown in Figure 3.2. The building has a flexural rigidity of E^*I, where E^* is an effective Young's modulus and I is the 2nd areal moment about the neutral axis of bending (horizontal in this case). E^* is typically much lower than the intrinsic E of the structural materials since the volume of buildings is mostly comprised of air. Since bending obeys a 4th order differential equation, the overall flexural stiffness of a beam decreases rapidly with increasing length of the beam; that is; flexural stiffness is defined as $\frac{E^*I}{L^3}$, where L is the building height. The effective shear modulus of the building is $G^*$and it is useful to compare overall building stiffness with soil stiffness to assess the importance of soil-structure interaction. In this case, G^* can be much lower than G of the building materials. In particular, moment resisting frame buildings are often designed to be flexible in shear, in which case G^* can be very small. The overall shear stiffness of the building is defined as $\frac{kG^*A}{L}$, where A is the cross-sectional area and k is the shear factor (to adjust for different cross-sectional shapes; $k=\frac{2}{3}$ for rectangular cross-section). The building considered here is assumed to have uniform stiffness and mass along its height, and remains linearly elastic. The effect of the soil is to cause both horizontal motions of the building's base as well as rocking about a horizontal axis. To simulate the effect of soil-structure interaction, a translational spring with stiffness K_T and a rotational spring with stiffness K_R are incorporated at the base of the building. Balendra et al. (1982) studied the responses of a linear N-story shear building sitting on an elastic homogeneous half space and showed that K_T and K_R can be estimated from the soil properties; that is $K_T=\frac{32(1-\upsilon)}{7-8\upsilon}G_{soil}r_o$ and $K_R=\frac{8}{3(1-\upsilon)}G_{soil}r_o^3$, where G_{soil} is the shear

modulus of the soil, υ is the Poisson's ratio of the soil, and r_o is the equivalent radius of the foundation.

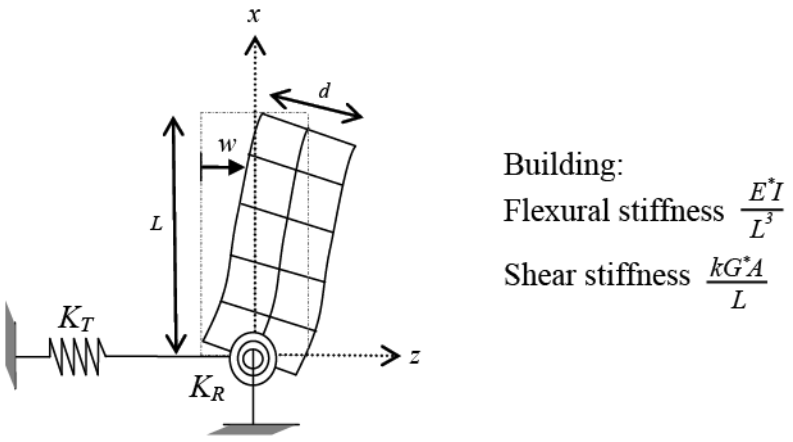

Figure 3.2: Timoshenko beam with soil-structure interaction. Horizontal spring K_T simulates the difference in horizontal ground motion of the base of the building caused by the inertial forces of the building on the ground. This effect is typically minor since the average density of the building is small compared to the ground. The rotational spring K_R simulates the rocking rotation of the base of the building.

Given the flexural stiffness and shear stiffness of a building, together with the soil spring stiffness, a closed-form free vibrational response is expressed as follows (the derivation is given in Appendix):

$$w = C_1 cosh\left(\alpha\frac{x}{L}\right) + C_2 sinh\left(\alpha\frac{x}{L}\right) + C_3 cos\left(\beta\frac{x}{L}\right) + C_4 sin\left(\beta\frac{x}{L}\right) \tag{3.1}$$

where w is the horizontal deflection; x is the distance along the vertical axis; α and β depend on the natural frequencies ω of the building.

The natural frequency ratio of the i^{th} mode is defined as f_i/f_1. In this study, the proposed method focuses on the frequency ratios estimated using the Timoshenko beam. A pure shear beam with a rigid base exhibits its first three natural frequency ratios as 1, 3, and 5, while a pure Euler-Bernoulli bending beam with a rigid base exhibits its first three natural frequency ratios as 1, 6.27, and 17.55. With the effect of soil-structure interaction, frequency ratio f_2/f_1 will not necessarily be bounded between 3 (pure shear type building on a fixed base) and 6.27 (pure bending type building on a fixed base) (refer to Figures 3.3-3.7 that will be explained in the following paragraphs). Timoshenko beams that have the same ratios between flexural stiffness, shear stiffness, and soil stiffness exhibit the same frequency ratios; that is, the frequency ratios are only functions of the stiffness ratios (G^*: E^*: G_{soil}) and the dimensions of the building (L, d). In other words, given the aspect ratio of the building, the stiffness ratio between shearing, bending and soil can be determined from the ratios of the frequencies of the normal modes. Here, shear stiffness-to-flexural stiffness ratios r is defined as follows:

$$r = \frac{\textit{shear stiffness}}{\textit{flexural stiffness}} = \frac{\frac{kG^*A}{L}}{\frac{E^*I}{L^3}} = \frac{kG^*AL^2}{E^*I} = \frac{8G^*L^2}{E^*d^2} \text{ for rectangular cross-section with } k = \frac{2}{3} \tag{3.2}$$

To investigate the dynamic behaviors of buildings on different soil conditions, three soil types with shear wave velocities V_s of 60m/s (very soft soil), 300m/s (stiff soil) and 1000m/s (fixed base) are chosen (Table 3.1). Soil with shear wave velocity V_s = 60m/s is considered as the very soft end of soft soil. In practice, buildings typically will not be constructed on such soil type. In this study, this very soft soil is considered to investigate the magnified effect of soil-structure interaction. Other parameters are arbitrarily chosen. This study will investigate how model parameters, including aspect ratio L/d, stiffness ratio r and building density $\rho_{building}$, are related to natural frequency ratios. In this sensitivity analysis, the effective shear modulus of the building is assumed to be $G^* = \rho_{building}\left(4Lf_1\right)^2 = \rho_{building}\left(4L\frac{30}{L}\right)^2 = 14400\rho_{building}$, where a story height of 3m is used and a fundamental period of 1sec is assumed for every 10 stories (i.e. $f_1 = 30/L$). Building density $\rho_{building}$ is assumed to be the order of 200kg/m^3 and the ratio E^*/G^* to be the order of 30 for frame buildings.

Table 3.1: Parametric study for Timoshenko beam model.

S-wave velocity V_s	60m/s (Very soft soil)	300m/s (Stiff soil)	1000m/s (Fixed base)
Soil density ρ_{soil}	1850kg/m^3		
Poisson's ratio υ	0.33		
Building width d	30m		
Aspect ratio L/d	1 to 10		
Building density $\rho_{building}$	200kg/m^3		
Equivalent foundation radius r_o	16.9m		
Soil shear modulus G_{soil}	6.67x10^{6}Pa	1.67x10^{8}Pa	1.85x10^{9}Pa
Soil translational stiffness K_T	5.54x10^{8}N/m	1.39x10^{10}N/m	1.54x10^{11}N/m
Soil rotational stiffness K_R	1.29x10^{11}Nm/rad	3.21x10^{12}Nm/rad	3.57x10^{13}Nm/rad
Effective shear modulus G^*	2.88x10^{6}Pa		
Effective Young's modulus E^*	8.64x10^{7}Pa		
Stiffness ratio r	varies		

Figure 3.3 (frame building, $\rho_{building}$ = 200kg/m^3) describes the effect of aspect ratio (by varying the building height L) on the frequency ratio. The frequency ratio of the Timoshenko beam with $L/d < 2$ cannot be computed because of the limitation in numerical computation (see Appendix A). The Timoshenko beam (considering shear deformation, as well as deformation due to bending moment and rotational inertia) that represents a frame building with a small aspect ratio (L/d = 2) behaves like a shear beam (considering shear deformation only), while the one with large aspect ratio (L/d = 10) does not necessarily behave like an Euler-Bernoulli bending beam (considering deformation due to bending moment only). This behavior of the frame building deviates from that of a solid beam; shear deformation of a long and thin (large L/d) solid beam can usually be ignored. For illustration, the frequency ratios of a solid beam with $\rho_{building}$ = 400kg/m^3 and the ratio E^*/G^* = 1 are presented in Figure 3.4. In such case, the Timoshenko beam with small aspect ratio (L/d = 1) behaves like a shear beam, while the one with large aspect ratio (L/d = 10) behaves like an Euler-Bernoulli bending beam.

For a fixed E^*/G^* ratio, stiffness ratio r depends on L/d (see Equation 3.2). In other words, given a fixed E^*/G^* ratio, a Timoshenko beam with large r is needed to achieve bending beam behavior. Also, due to the consideration of rotational inertia, the Timoshenko beam reacts like a Rayleigh bending beam (considered deformation due to bending moment and rotational inertia) when r is large. On the other hand, the effect of soil-structure interaction depends on the overall building stiffness (shear stiffness + bending stiffness) with respect to the soil stiffness. In other words, if the building is stiff relative to the soil, no matter the building behaves like a shear beam or a bending beam, soil-structure interaction effect will be significant.

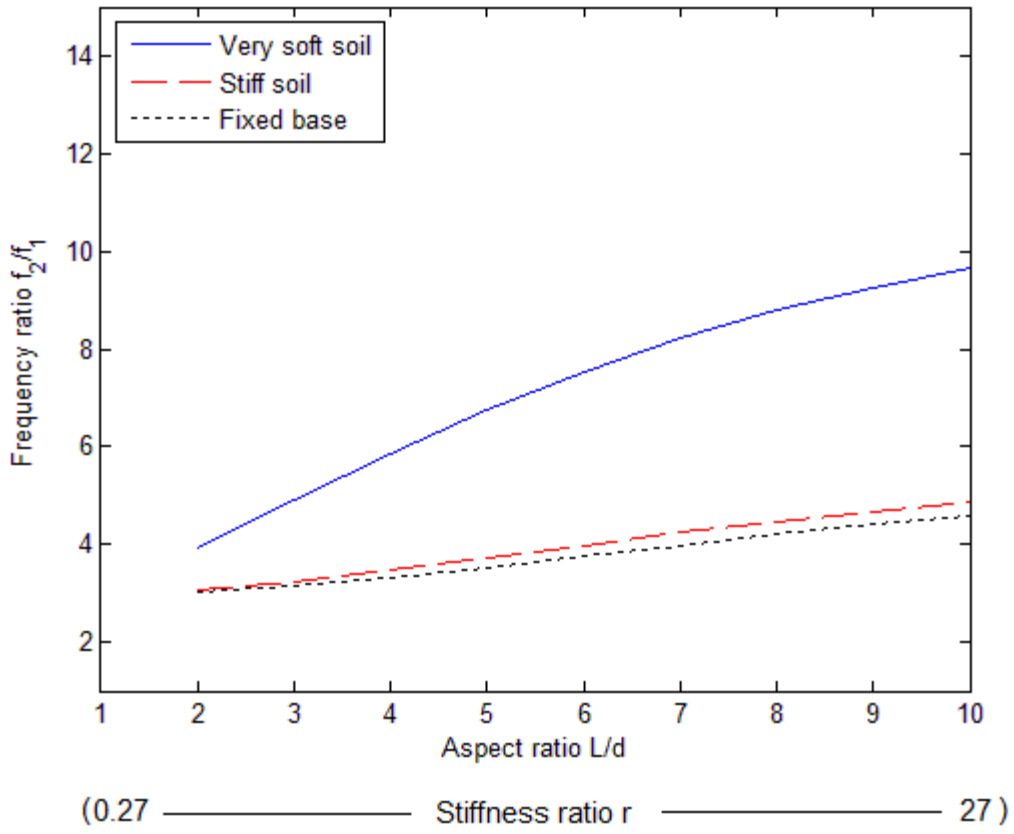

Figure 3.3: Effect of aspect ratio L/d on frequency ratio of buildings with $\rho_{building} = 200 kg/m^3$ and $E^*/G^* = 30$ (frame building).

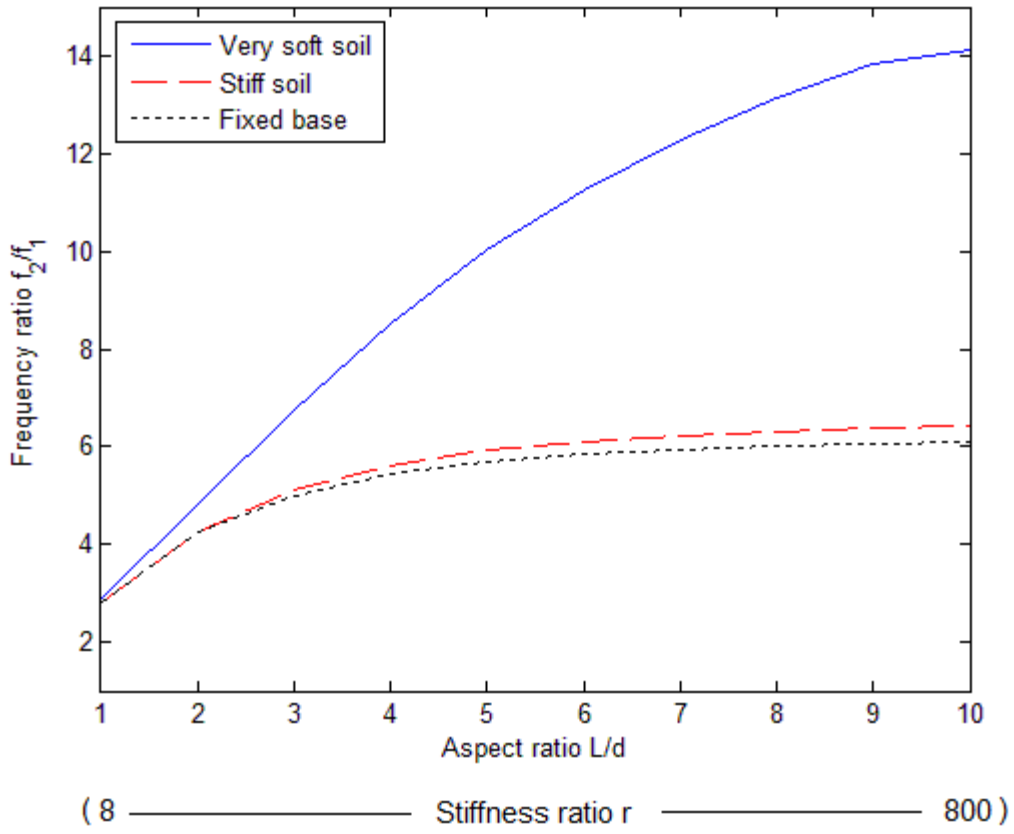

Figure 3.4: Effect of aspect ratio L/d on frequency ratio of buildings with $\rho_{building}$ = 400kg/m^3 and E^*/G^* = 1 (solid beam).

Stewart and Fenves (1998) suggest that soil-structure interaction predominately affects the fundamental natural frequency, and this observation agrees with the numerical study. In the example of a frame building, Figure 3.5a shows that the natural frequencies of a Timoshenko beam with small aspect ratio (L/d = 2) are reduced by 20%, and 10-15%, respectively, for the 1st modes and higher modes; while the natural frequencies of a Timoshenko beam with large aspect ratio (L/d = 10) are reduced by 60%, and 10-15%, respectively, for the 1st modes and higher modes. The individual effects of soil rotational spring stiffness K_R and soil translational spring stiffness K_T are also investigated. As shown in Figure 3.5b, K_R has significant effect on the 1st mode frequency, but

minimal effect on the higher modes. On the other hand, K_T in general has less than 15% effect on the frequencies. Nevertheless, real buildings behave like a Timoshenko beam with properties in between a pure shear beam and a pure bending beam, so soil-structure interaction should not be neglected in determining the dynamic behavior of buildings during earthquakes.

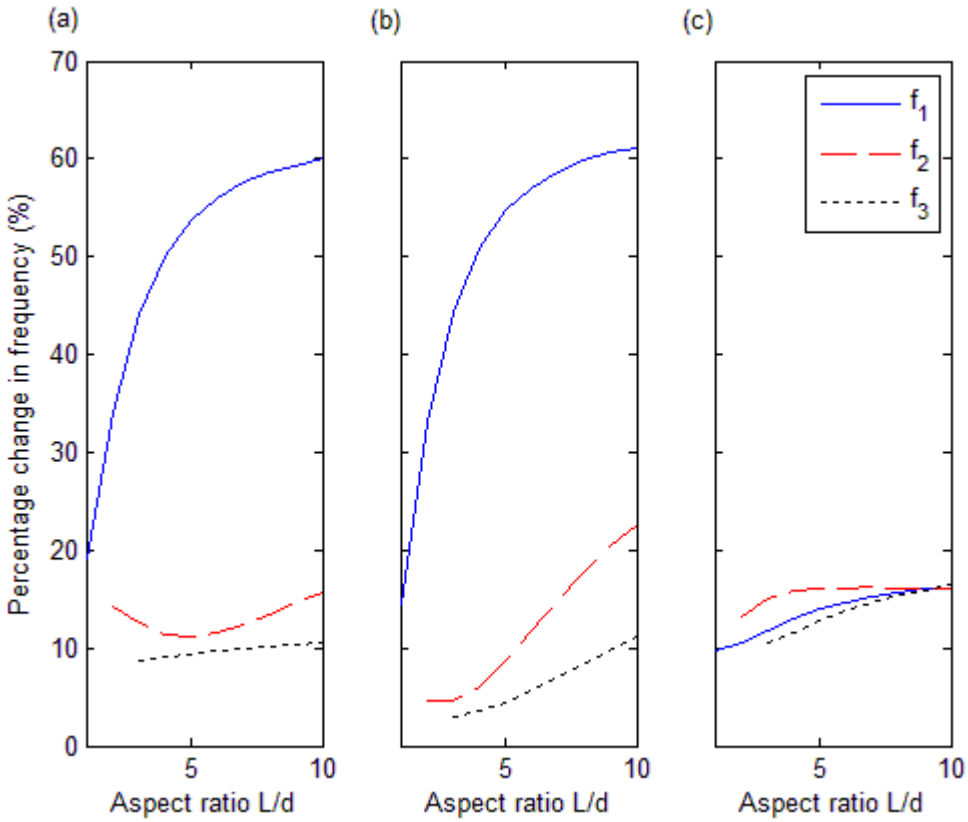

Figure 3.5: Effect of aspect ratio L/d on the percentage change in frequency of the first three modes. (a) Very soft soil (V_s = 60m/s) with soil translational K_T and rotational K_R springs. (b) Very soft soil with soil rotational K_R spring only. (c) Very soft soil with soil translational K_T spring only.

3.2 BUILDING SYSTEM IDENTIFICATION

To simulate the spatial/temporal dynamic behavior of an existing building, follow these steps: (1) Estimate S-wave velocity V_s, the soil density ρ_{soil} and Poisson's ratio υ of the soil. (2) Estimate the dimensions (width d, and height L) of the building; these values can usually be approximated using Google Earth. Underground sub-structures usually contain thick and stiff shear walls, so they have a minimal effect on the building's deflection. We can therefore roughly approximate L as the height above ground. (3) Estimate the density for the building $\rho_{building}$; this value can be approximated from the structural type of the building. Building densities, $\rho_{building}$, are assumed to be the order of 200kg/m^3 for frame buildings, and 400kg/m^3 for shear wall buildings. (4) Determine the first two natural frequencies (f_1 and f_2) of the building in a particular direction from spectral analysis of motions (either ambient noise or driven by minor earthquakes) recorded by an installed seismometer. (5) Calculate soil spring properties: (5a) Equivalent foundation radius: $r_o = \sqrt{\frac{cross\text{-}sectional\ area\ of\ building}{\pi}}$. (5b) Soil shear modulus: $G_{soil} = V_s^2 \rho_{soil}$. (5c) Soil translational spring stiffness: $K_T = \frac{32(1-\upsilon)}{7-8\upsilon} G_{soil} r_o$. (5d) Soil rotational spring stiffness: $K_R = \frac{8G_{soil} r_o^3}{3(1-\upsilon)}$. (6) Calculate building properties: (6a) Effective shear modulus of the building: $G^* = \rho_{building} \left(4Lf_1\right)^2$. (6b) Stiffness ratio r, as well as effective Young's modulus of the building E^* (through Equation 3.2), can be approximated from the defined parameters and the measured natural frequency ratio f_2/f_1 using the characteristic equation (Equation A.26 in Appendix A). (7) The constructed Timoshenko beam model will provide natural frequency ratios f_i/f_1 as well as the corresponding mode shapes, where f_i is the ith mode frequency and f_1 is the fundamental mode frequency. Higher mode frequencies can be estimated from the measured fundamental natural

frequency. From the numerical method for solving the differential equations, the maximum estimated natural frequency is bounded by the following condition: $f_{max}^2 < \frac{kGA}{(2\pi)^2 \rho_{building} I}$ (see Appendix A).

3.3 EXISTING STRUCTURE ANALYSIS: MILLIKAN LIBRARY

Caltech Millikan Library (Figure 2.4) is a nine-story reinforced-concrete building with one level of basement embedded in stiff soil whose shear wave velocity is about 300m/s. The building has both moment resisting frames as well as a very stiff core-wall in both the NS and EW directions. It also has continuous NS shear walls that extend from the foundation to the roof on the east and west sides of the building. It is an unusually stiff building considering its height. Millikan Library has been instrumented since its first construction in 1966, and it is possible to compare the apparent modal frequencies that have been recorded for many earthquakes and shaking experiments. Furthermore, a 36-channel accelerometer network recorded by a Kinemetrics Mt. Whitney system was installed in 1998; this system is a triggered system that measures horizontal building motions on every level of the building including the basement and the roof. An almost continuous recording of building motions is available since 2000 when the Southern California Seismic Network installed the station MIK on the 9th floor. In 2008, a 3-axis rotational sensor was added to MIK and a second identical station, MIKB, was installed in the basement.

A Kinemetrics harmonic shaker was installed on the roof of the library in early 1970s and it has been used for many class projects and research studies over the past decades (Figure 2.4); the maximum frequency of the shaker is 9Hz. From forced vibration experiments, the first two measured NS modal frequencies are 1.75Hz and 7.21Hz (Bradford, 2006), corresponding to natural

frequency ratios of 1 and 4.1. The third NS mode has not yet been identified and its frequency is almost certainly higher than the 9Hz limit of the roof shaker. The first two measured EW modal frequencies are 1.22Hz and 4.76Hz (Bradford, 2006), corresponding to natural frequency ratios of 1 and 3.9. An apparent resonance at 7.83Hz was suggested by Bradford to be the 3rd EW mode. However, that mode shape is not orthogonal to the other two mode shapes. Therefore, only the first two identified EW modes are considered in this chapter.

Table 3.2 shows the parameters used to construct the Timoshenko beam model for Millikan Library. Values for soil properties and building properties are extracted from Favela (2004) and Todorovska (2009). The calculated stiffness ratio r is 27 and 17 for NS and EW directions, respectively. The frequency ratios f_2/f_1 of Millikan Library are similar for both directions, which means that the shear stiffness relates in the same way to the flexural stiffness for both directions. Using the Timoshenko beam model, the estimated third vibration mode occurs at 15.3Hz (f_3/f_1 = 8.75) and 10.05Hz (f_3/f_1 = 8.24) for NS and EW directions, respectively. These values are definitely higher than the 9Hz safety limit of the roof shaker, so they have not been identified.

Figures 3.6-3.7 shows the estimated mode shapes. The mode shapes produced from the Timoshenko beam are good estimations of the measured ones. The frequency ratios f_2/f_1 of 3.9 and 4.1 occur in between that of a pure shear beam and a pure bending beam. In such case, mode shapes of the Timoshenko beam provide a much better result compared to those of a pure shear beam. The two estimated 3rd mode shapes from the Timoshenko beam are also provided in the figures.

Table 3.2: Timoshenko beam model parameters for Millikan Library.

	NS direction	EW direction
Input:		
S-wave velocity V_s	316m/s	
Soil density ρ_{soil}	1850kg/m^3	
Poisson's ratio υ	0.306	
Building depth d	21m	23m
Building height L	44m	
Building density $\rho_{building}$	400kg/m^3	
Fundamental frequency f_1	1.75	1.22
Frequency ratio f_2/f_1	4.1	3.9
Calculate:		
Equivalent foundation radius r_o	12.4m	
Soil shear modulus G_{soil}	1.67x10^{8}Pa	
Soil translational stiffness K_T	1.01x10^{10}N/m	
Soil rotational stiffness K_R	1.22x10^{12}Nm/rad	
Effective shear modulus G^*	3.79x10^{7}Pa	1.84x10^{7}Pa
Output:		
Stiffness ratio r	27	17
Effective Young's modulus E^*	4.11x10^{7}Pa	3.81x10^{7}Pa

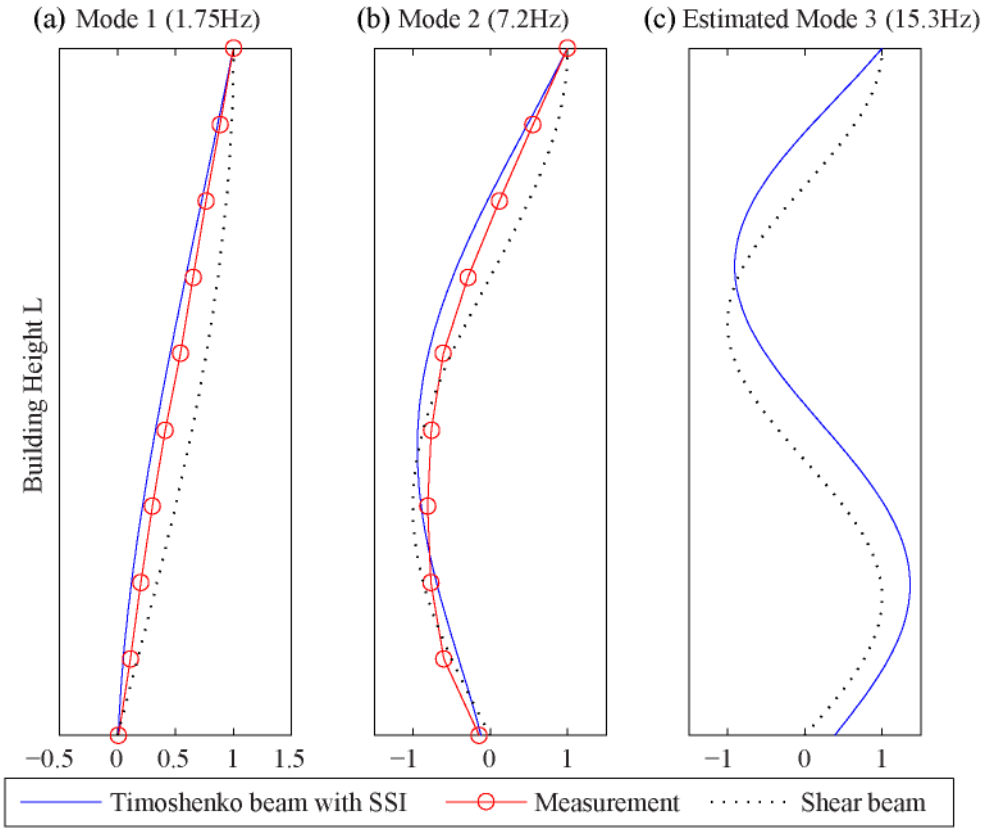

Figure 3.6: Mode shapes comparison of Millikan Library in NS direction.

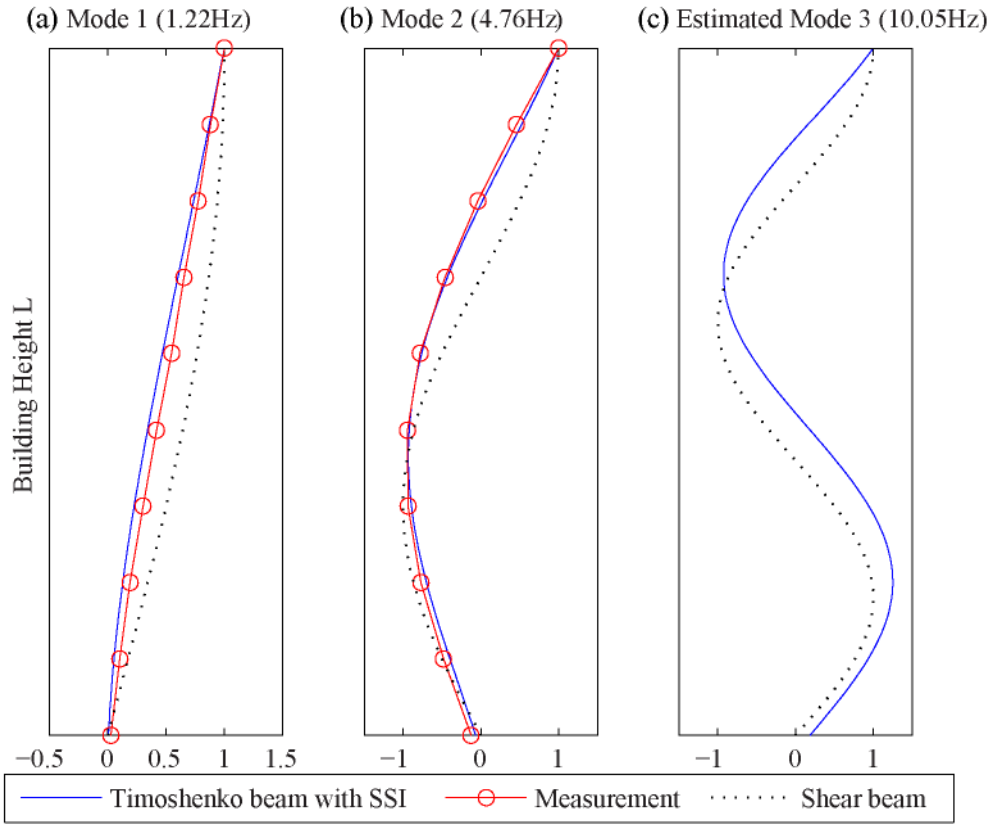

Figure 3.7: Mode shapes comparison of Millikan Library in EW direction.

3.4 CONCLUSION

Simple models of buildings as a shear beam have been surprisingly successful. They can be used to explain many features of modes of vibration of buildings and they can help to understand traveling waves in a building (e.g. Kohler et al., 2007; Rahmani and Todorovska, 2013). However, there are cases where buildings exhibit global bending about their base (tall and slender buildings that are stiff). Furthermore, there are cases in which we would like a better understanding of the effect of foundation rocking. All of these effects are incorporated in the solution for a cantilevered Timoshenko beam on a translational spring as well as a rotational spring. The good news is that the

solution is expressible in a closed form (see Equations A18-A19 in Appendix A). Unfortunately, the expressions are far more complex than for a simple shear beam.

A formal methodology is presented that produces the mode shapes of a building assuming that (1) we have records from at least one seismometer in the building from which we can determine the first two modal frequencies in a given direction, (2) that we can estimate the exterior dimensions of the building, and (3) that the building can be approximately modeled as a Timoshenko beam on a translational and rotational base. Of course the last assumption is both critical and dubious. That is, few buildings are really prismatic; it is common to design tall buildings with larger structural elements in the lower stories (they also have larger effective densities). Miranda and Taghavi (2005) have investigated the effect of linear and parabolic variations of lateral stiffness along the building height using finite element models. They suggest that the effect of non-uniform stiffness on mode shapes and frequency ratios is very small and can be neglected for bending type structures. The individual effect on shear type structures is larger, but the overall influence is relatively small and can be neglected. Nevertheless, this simple methodology does predict the type of mode shapes of a building that has significant bending (e.g. Millikan Library).

Knowing the earthquake response from one sensor on a particular floor of a building can allow us to estimate responses for the other floors using the calculated mode shapes through modal decomposition (Kohler et al., 2013). In addition, the Timoshenko beam model can be used to estimate building responses for predicted ground motions. The time behavior of each mode can be determined by solving the problem of a linear single degree of freedom oscillator with the appropriate frequency and damping (damping can be approximately obtained from spectral analysis of the data). With appropriate participation factor for each modal response, a vector sum of the modes can be performed to find approximate deformations and floor accelerations for the entire

building for the ground motion. The results can allow us to approximate the performance of non-structural elements (e.g. elevator system, mechanical piping systems, and etc.) due to large floor accelerations, while the structure of the building remains elastic.

In practice, it may be best to estimate the approximate effect of foundation rocking by estimating the rocking stiffness from the elasticity parameters of the soil and the footprint of the building. For example, Bycroft (1956) presented the solution for a rigid circular disk that is forced to rock on an elastic half space. This approach has not been pursued. However, if we had an independent estimate of the rocking stiffness, we could still use the derived solutions to estimate the approximate building motions from estimates of the first two modal frequencies. In this study, buildings without significant plan irregularities are emphasized, so torsional effects have been ignored. Possible future studies can include the effect of 3-dimensional seismic excitation and an extension of the existing Timoshenko beam model to capture the torsional responses as well as the non-linear response of a tall building. Such analysis may require comparisons with 3-dimensional finite element simulations. Nevertheless, the procedure described here should provide a good estimate of building motion and it is relatively simple to apply. However, it is important for any potential user to recognize that this type of analysis cannot produce detailed results.

Chapter 4

PREDICTION OF WAVE PROPAGATION IN BUILDINGS

As mentioned in the previous chapter, in the structural array components of some crowd-sourced seismic networks, there may be instances in which a single seismogram is the only record that is available from a building. In this chapter, a new computational tool is presented to estimate and visualize the linear elastic motions of existing, instrumented buildings that have recorded earthquake shaking. The method is verified with observations from dense structural array data and numerical simulations. Using the time series from a single station in a building, the linear elastic displacement response predicted for all floors based solely on modal decomposition may not adequately capture the initial impulsive response. This can lead to an underestimation of floor displacement, especially if maximum floor response occurs during the coherent, impulsive ground motion before the resonant mode response dominates (Iwan, 1997). To address this issue, building motion due to earthquake excitation is decomposed into the broadband traveling wave component and the low-frequency resonant mode component. Computed mode shapes of the building are used to relate the resonant mode response from an observation on one floor to calculated predictions for response on the other floors.

The application of fixed-base shear beam mode shapes to tall buildings is often a good assumption (e.g. Jennings, 2003), particularly if the observed frequency ratios match those of the shear beam (i.e., f_1, $3f_1$, $5f_1$ where f_1 is the fundamental translational frequency in a particular direction). If the natural frequency ratios of the target building are different from those of a shear beam, then mode shapes from a Timoshenko beam can be adopted when significant flexural response is observed. Mode shapes can be closely approximated by the knowledge of the natural frequencies of the first two translational modes in a particular direction of the building, and the

building dimensions. In Chapter 3, a Timoshenko beam model with lateral and rotational springs at the base is adopted to approximate the dynamic linear-elastic behavior of the buildings. In many cases, the natural frequencies of the first two vibrational modes of a building can be determined from data recorded by a single seismometer. The building response of the other floors can then be assembled. The method presented here is suitable if building response remains linear elastic.

4.1 BUILDING RESPONSE DURING EARTHQUAKES

Given a particular ground motion, the linear elastic building response due to earthquake excitation can be computed in two complementary bases: the traveling wave representation and the resonant mode representation. Given vast computational resources and no observational limitations, either approach would independently capture the complete linear dynamic response. One approach is to sum reflecting pulses traveling within the building. Equation 4.1a shows the wave propagation solution of a continuous fixed-base shear beam model (e.g. Sasani et al., 2006),

$$u(t,z)=\sum_{k=1}^{\infty}(-1)^k\,\zeta(2kH+z)\,u_g\left(t-\frac{zT_1}{4H}-\frac{kT_1}{2}\right)-\sum_{k=1}^{\infty}(-1)^k\,\zeta(2kH-z)\,u_g\left(t+\frac{zT_1}{4H}-\frac{kT_1}{2}\right) \tag{4.1a}$$

where $u(t,z)$ is the displacement response; t is time; z is height from the ground; H is the total building height; T_1 is the fundamental vibrational period of the building; $\zeta(z)$ is the damping function; $u_g(t)$ is the horizontal ground motion; and k is the index of summation. This closed-form solution is true for a shear beam where the traveling wave velocity is independent of the wavelength, i.e., wave velocity $c = (4H)/T_1$. In order to include wave dispersion, convolution with functions that include the phase information would be necessary, but the solution would become complicated. Nevertheless, the wave solution for a shear beam is a good approximation for

displacement response in buildings when the dispersion effect is small, i.e., when the initial impulse begins its first transit leg up the building.

Alternatively, displacement response in buildings can be obtained by summing an infinite number of resonant modes, each with specific phase (e.g., Roberts and Lutes, 2003) (Equation 4.1b)

$$u(t,z) = \sum_{m=1}^{\infty} u_m(t,z) = \sum_{m=1}^{\infty} \phi_m(z) q_m(t) \tag{4.1b}$$

where $u_m(t,z)$ is the building response of the m^{th} mode; $\phi_m(z)$ is the m^{th} mode shape; $q_m(t)$ is the modal displacement at the m^{th} modal coordinate; and m is the index of summation. Dispersion effects are implicitly incorporated into this solution. Given information from a single seismometer, we cannot always identify higher-mode natural frequencies or their corresponding damping ratios. Therefore, we are unable to add up all the modes for the resonant mode solution to approach the full wave solution. To get around this limitation, a fast and robust method will be presented that captures the initial broadband impulse traveling along the building height by the wave solution and transitions to subsequent low-frequency building displacement response using the resonant mode solution.

4.2 SEISMIC RECORDS FROM A 54-STORY BUILDING

Earthquake records of a 54-story office building in downtown Los Angeles (Figure 4.1) are used to describe the response prediction method. The 54-story building, constructed in 1991, is a rectangular building with base dimensions of 64.7m x 41.5m and founded on a concrete mat foundation. The lateral resisting system is mainly made up by the moment-resisting perimeter steel frame with three-meter column spacing. There are Virendeel trusses and 14.6-meter transfer girders

at the 36th and 46th floors to accommodate the dislocations of vertical structural elements. The building is instrumented by the California Strong Motion Instrumentation Program (CSMIP) with accelerometers on the penthouse, 46th floor, 36th floor, 20th floor, ground floor and the P4 underground level. Structural details and seismic records of this building can be found in the Center for Engineering Strong Motion Data (http://www.strongmotioncenter.org). This tall building is chosen because the displacement records of this building show significant effects from the 1st and 2nd translational modes, as well as smaller contributions from the 3rd mode. It also exhibits strong traveling wave behavior during the initial response to earthquakes. It is shown later that although the proposed method neglects the influence of torsion, which can be significant for tall buildings, the first-order prediction agrees well with the measured data.

Figure 4.2 shows the recorded displacements in the NS direction of the 54-story building on the 20th, 36th, 46th and penthouse floors during the July 29th, 2008 M5.4 Chino Hills, CA earthquake (epicentral distance = 47km). The displacement spectra demonstrate that the building's displacement responses are dominated by the 2nd NS mode. The influence due to the 1st mode is significant and there are lesser contributions from the 3rd mode. The 1st, 2nd and 3rd NS modal frequencies of the building are observed to occur at 0.18Hz, 0.52Hz and 0.84Hz. The natural frequency ratios are approximately 1, 3 and 5 which are close to those of a fixed-base shear beam, so we assume the mode shapes of this building are close to those of a fixed-base shear beam. In addition, an initial upward traveling impulse is observed at t = 0sec (Figure 4.2). The first crest of the impulse is reflected at the roof at t = 1.5sec.

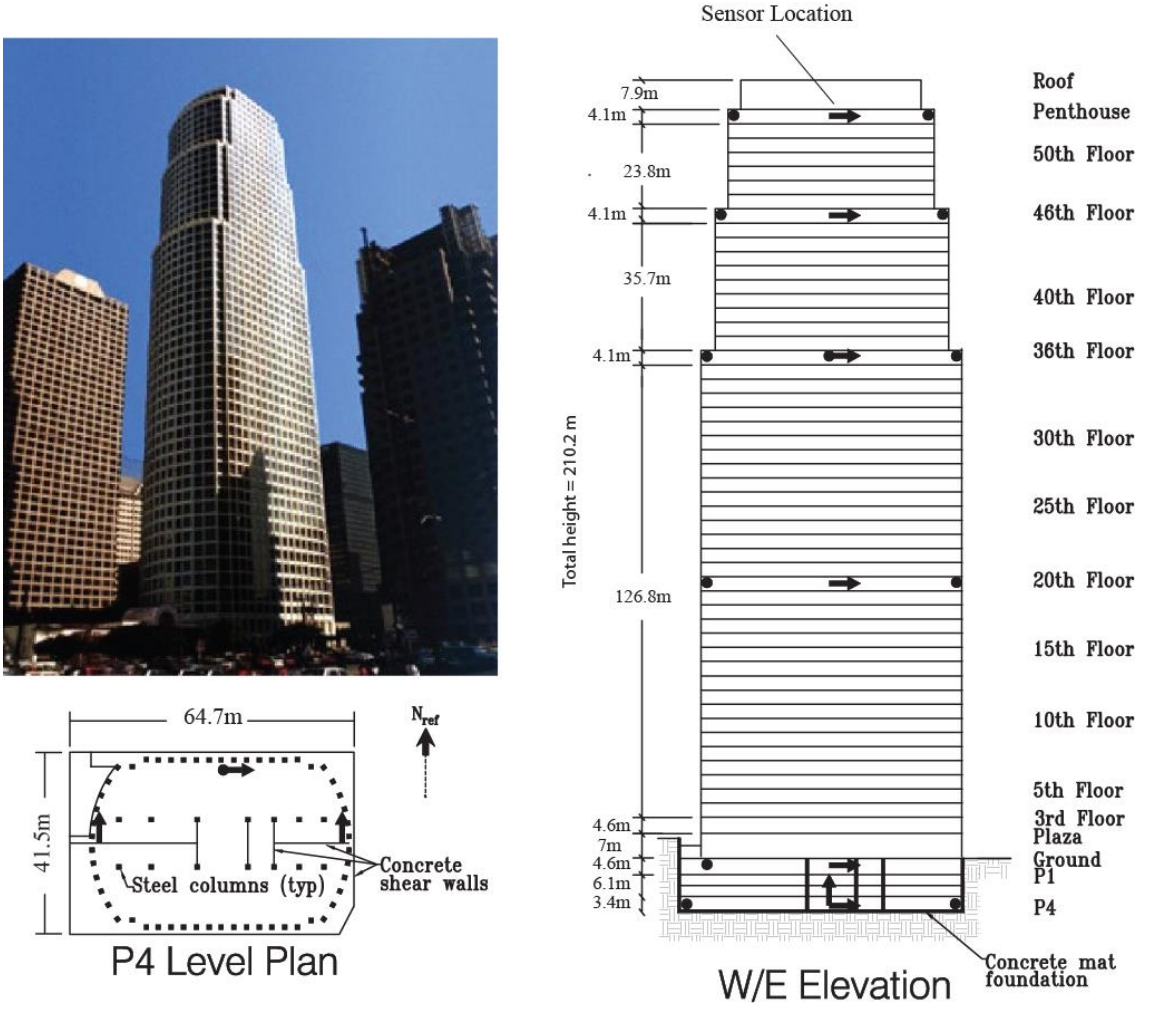

Figure 4.1: Photo and diagrams of the 54-story building in downtown Los Angeles, CA showing building dimensions, floor heights, and seismic network configuration (from the Center for Engineering Strong Motion Data).

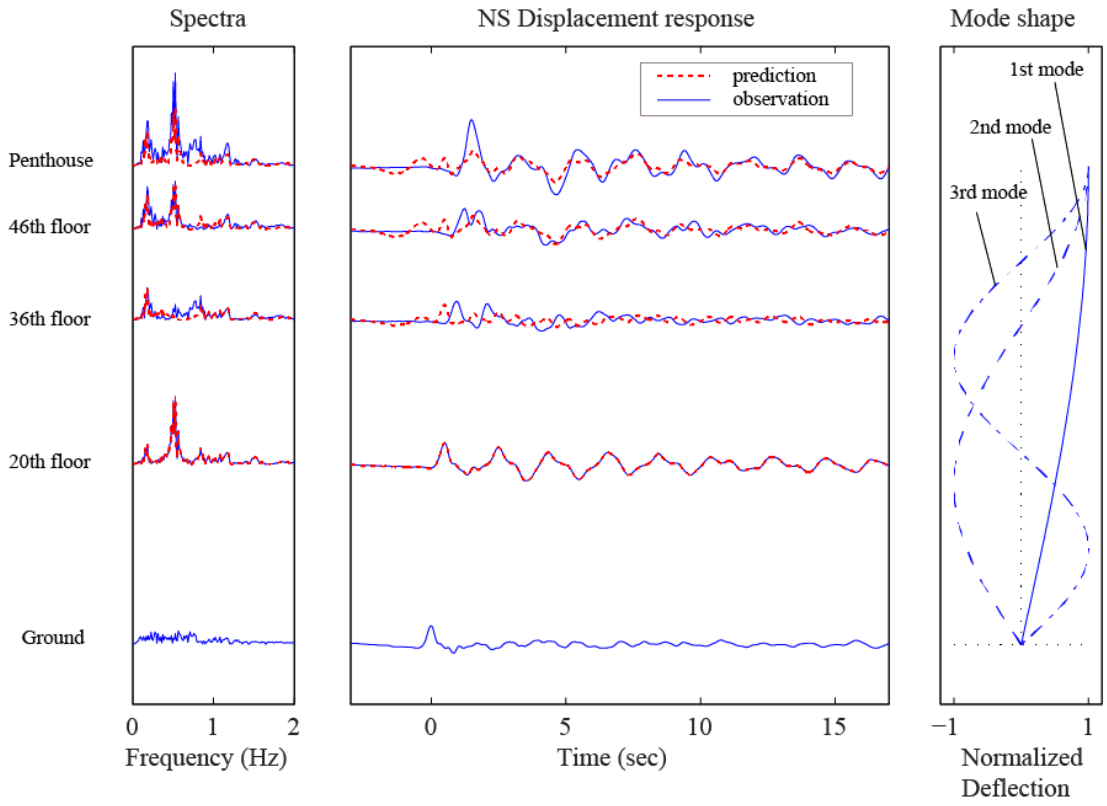

Figure 4.2: Simulated (based only on resonant mode solution) and observed displacement responses of the 54-story building in the NS direction during the 2008 M5.4 Chino Hills, CA earthquake. The vertical locations of the records are shown by the floor levels in the building. Displacement time series are normalized to the same scale by data from the penthouse which has maximum absolute displacement= 1.45cm and minimum absolute displacement= -2.34cm.

Assuming that we only have input from a single seismometer on the 20th floor of the building, the displacements of the other floors are estimated to show the total building response. First, the building response estimate solely based on resonant modes is investigated. The 2008 Chino Hills earthquake displacement records are band-pass filtered with second-order, zero-phase Butterworth filters for frequencies 0.1-0.4Hz for the 1st resonant mode; 0.4-0.7Hz for the 2nd resonant mode; and

0.7-1.0Hz for the 3rd resonant mode. The resonant mode response $u_r(t,z)$ at height z from the ground, constrained by data produced by a single seismometer at height z_s, can be approximated as

$$u_r(t,z)|_{\text{station}=z_s} = \sum_{m=1}^{\text{no. of modes}} \left[f_m(t,z_s) \cdot \frac{\varphi_m(z)}{\varphi_m(z_s)} \right] + u_{rb}(t,z_s) \tag{4.2}$$

where t is time; $f_m(t,z_s)$ is the filtered response for the m^{th} mode for the single record at height z_s; $\varphi_m(z)$ is the mode shape deflection value as a function of height z for the m^{th} mode; and $u_{rb}(t,z_s)$ is the residual motion after the filtered response component has been subtracted from the data. This residual motion $u_{rb}(t,z_s)$ is assumed to be the rigid-body motion due to the ground excitation:

$$u_{rb}(t,z_s) = u(t,z_s) - \sum_{m=1}^{\text{no. of modes}} \left[f_m(t,z_s) \right] \tag{4.3}$$

In other words, the filtered time series for different modes are related to the other floors using the corresponding mode shapes of the building, and resonant mode solution motions are included in the floor response prediction. The time series comparisons between the estimation from the 20th floor and the data are displayed in Figure 4.2. The prediction solely based on modal decomposition does not adequately capture the initial upward traveling impulse from the ground, and it underestimates the peak floor response at the penthouse by a factor of more than 2 at $t \cong 1.5$sec. This estimation matches the seismic records for subsequent times after the initial impulse has reached the top of the building, however. Note that Iwan (1997) indicated that maximum floor response might occur during the coherent impulsive ground motions before the resonant mode response dominates.

4.3 BUILDING RESPONSE PREDICTION USING A SINGLE SEISMOMETER

Since modal decomposition using the first few modes does not capture the initial traveling impulse during earthquakes, the traveling wave solution is used to capture the initial upward traveling impulse along the building height. To transition from traveling wave solution to resonant mode solution, we use a linear transition function which begins at the time when the initial impulse first travels to the roof of the building (i.e., $t = T_1/4$ from the start of base excitation), and ends at the time when the initial impulse makes its first reflection back to the building's base (i.e., $t = T_1/2$ from the start of base excitation), where T_1 is the fundamental period of the building. The total estimated displacement response $\hat{u}(t,z)$ is defined as a function of weighted traveling wave and weighted modal solution:

$$\hat{u}(t,z) = u_w(t,z) \cdot w_w(t,z) + u_r(t,z) \cdot w_r(t,z) \tag{4.4}$$

where $u_w(t,z)$ and $w_w(t,z)$ are the wave solution and weighting function for the wave solution; $u_r(t,z)$ and $w_r(t,z)$ are the resonant mode solution (see Equation 4.2) and weighting function for the resonant mode solution. At subsequent times when wave attenuation and dispersion effects become significant, building motions cannot be easily modeled by the wave solution.

To predict floor displacement using information from a single seismometer, the initial impulse is assumed to take time = $T_1/4$ to travel up building height H (equal to the wave travel time in a shear beam), i.e., wave velocity $c = (4H)/T_1$. The subsequent modal response solution capturing the low-frequency vibrating modes is identified either by FFT analysis or by system identification methods (e.g. Overschee, 1994; Ljung, 1999; Clinton et al., 2006) applied to the seismic records (Equation 4.2). Using the pre-calculated mode shapes that assumed a beam representation, the

modal displacement responses on the other floors can be computed. If the frequency ratios of a building are different from those of a fixed-base shear beam, mode shapes of a Timoshenko beam can be used (see Chapter 3).

The initial impulse is observed in the displacement record from the 20th floor of the 54-story building for the 2008 Chino Hills, CA earthquake (Figure 4.3). This initial impulse shape is replicated on other floors according to the traveling shear-wave speed estimated for this building, i.e., wave velocity $c = (4H)/T_1 = (4 \times 210) / 5.83 = 144$m/s. This impulse is simulated for a cycle that includes one upward and one downward leg vertically along the building. Using the approximated shear-wave velocity, the first crest of the impulse is estimated to arrive at the roof at time $t_1 = 1.5$sec where it will be reflected and will reach the base of the building at time $t_2 = 2.9$sec. In this example, let $TS_b(t)$ be the time series response before t_1 on the 20th floor; the value of $TS_b(t)$ is zero for $t > t_1$. Similarly, let $TS_a(t)$ be the time series response after t_1 on the 20th floor; thus the entire time series on the 20th floor is $TS_{20F}(t) = TS_b(t) + TS_a(t)$. This representation allows us to simply shift the time series $TS_b(t)$ and $TS_a(t)$ according to the estimated wave velocity to simulate the wave propagation effect up the building. The simulated wave solution for the initial impulse on the target floor $u_w(t,z)$ can then be expressed as

$$u_w(t,z) = TS_b(t - d/v) + TS_a(t + d/v) \tag{4.5}$$

where $d = z - z_s$, and z_s is the height of the seismometer floor from the ground; v is the wave velocity. In our example, d is positive when the target floor is above the 20th floor (the single seismometer floor), which implies $TS_b(t)$ and $TS_a(t)$ will merge; d is negative when the target floor is below the 20th floor, which implies $TS_b(t)$ and $TS_a(t)$ will diverge.

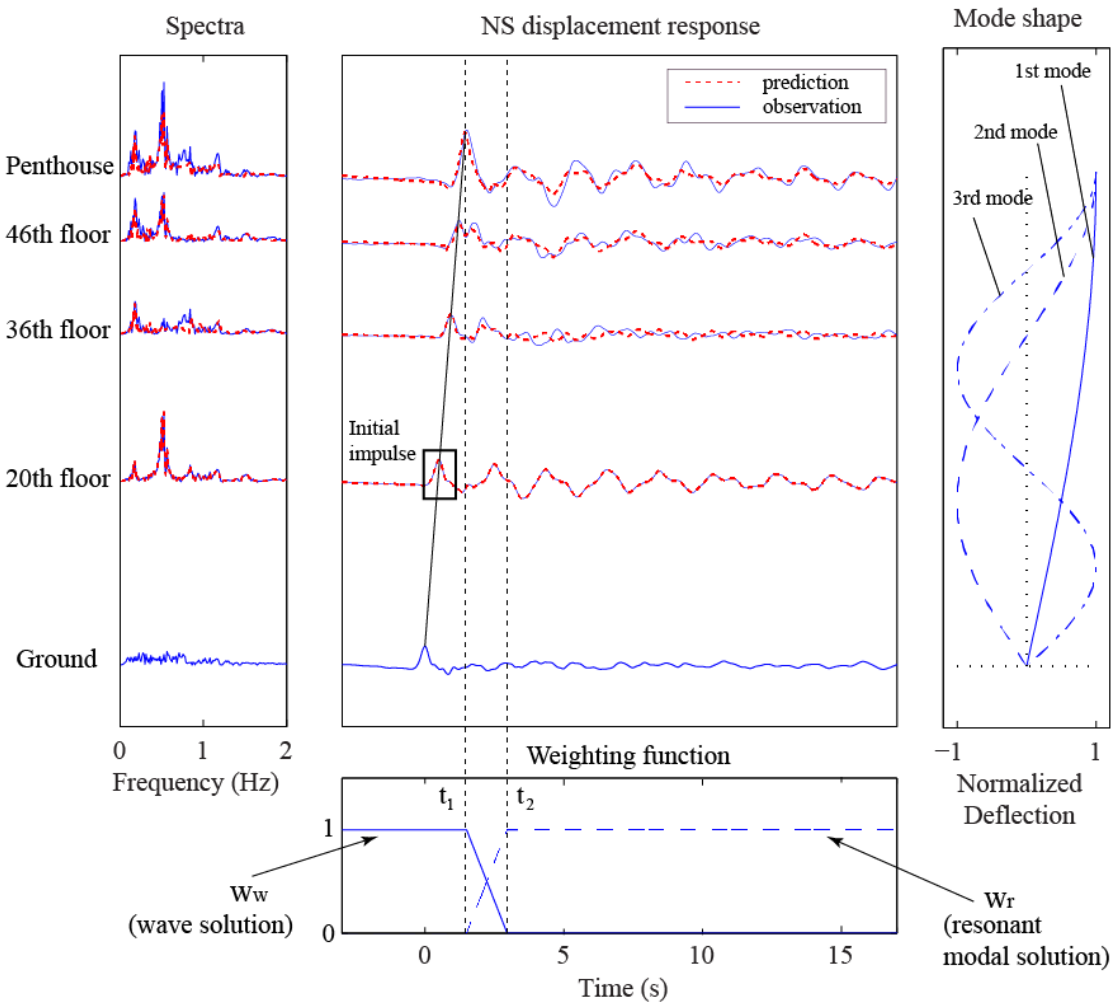

Figure 4.3: Simulated (based on the combined, weighted, traveling wave plus resonant mode method described in text) and observed displacement responses of the 54-story building in the NS direction during the 2008 M5.4 Chino Hills, CA earthquake. The vertical locations of the records are shown by the floor levels in the building. Displacement time series are normalized to the same scale by data from the penthouse which has maximum absolute displacement = 1.45cm and minimum absolute displacement = -2.34cm.

For the 54-story example, the simulated impulse travels up the building. Then we apply weighting functions according to the time t_1 and t_2 for the transition to the resonant mode responses

(see Equation 4.3 and Figure 4.3). For subsequent times, the observed displacement record from the single seismometer is band-pass filtered with a second-order, zero-phase Butterworth filter on the first three resonant frequencies to get the modal response time series. Responses for the other floors are related to the 20th floor using the mode shapes of a fixed-base shear beam (Equation 4.2).

Figures 4.4 and 4.5 show the results of the method applied to the 54-story building comparing the four different single seismometer inputs (20th, 36th, 46th and penthouse floors). Unlike the mode-only solution, this method also models the initial traveling wave. Figures 4.4a and 4.5a show the predicted floor response time series and spectra using the record at the penthouse as input. The penthouse data successfully capture the first three modes, so the subsequent modal responses are well-estimated on the other floors. The same applies to the data recorded on the 46th floor (Figures 4.4b and 4.5b). The 36th floor is near a nodal point of the 2nd mode, so the data do not capture any contribution from the 2nd mode (Figures 4.4c and 4.5c). With only combinations of the 1st and 3rd modes, the predicted responses on the other floors are somewhat degraded. Although the 20th floor is near a nodal point in the 3rd mode, the prediction agrees with the observation using only the information from the 1st and 2nd modes (Figures 4.4d and 4.5d).

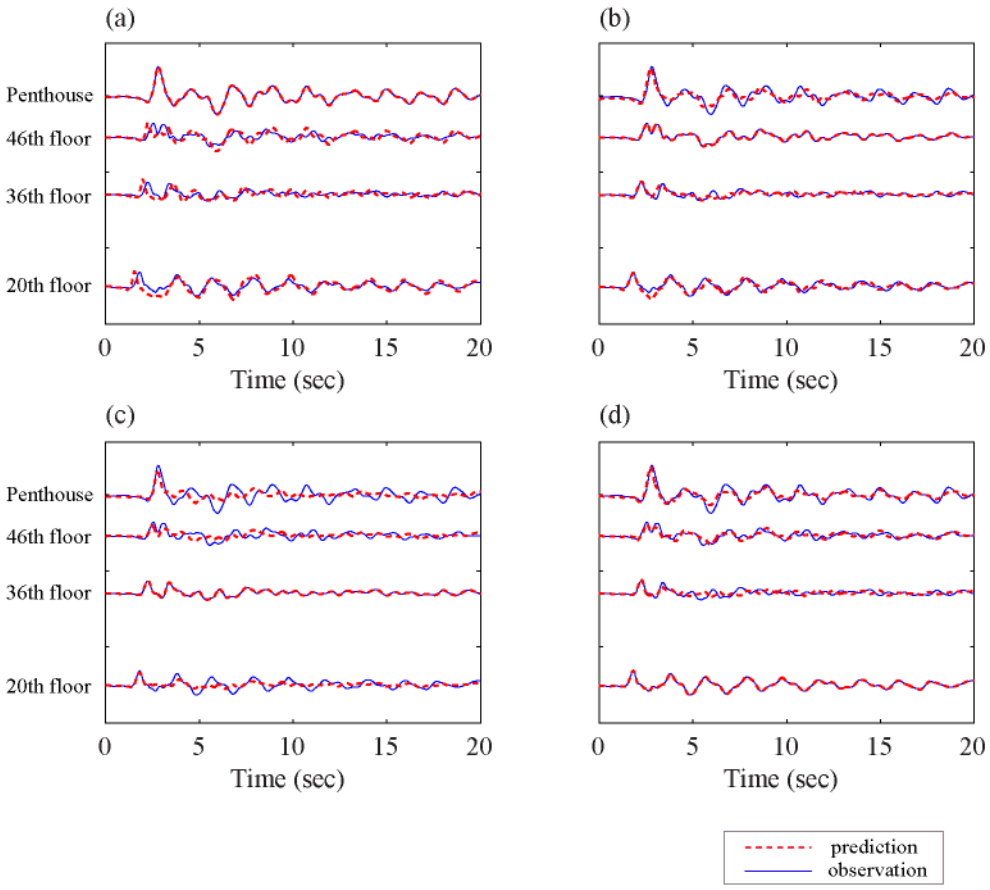

Figure 4.4: Displacement responses of the 54-story building in the NS direction for the 2008 M5.4 Chino Hills, CA earthquake. (a) Prediction using the record from the penthouse. (b) Prediction using the record from the 46th floor. (c) Prediction using the record from the 36th floor. (d) Prediction using the record from the 20th floor.

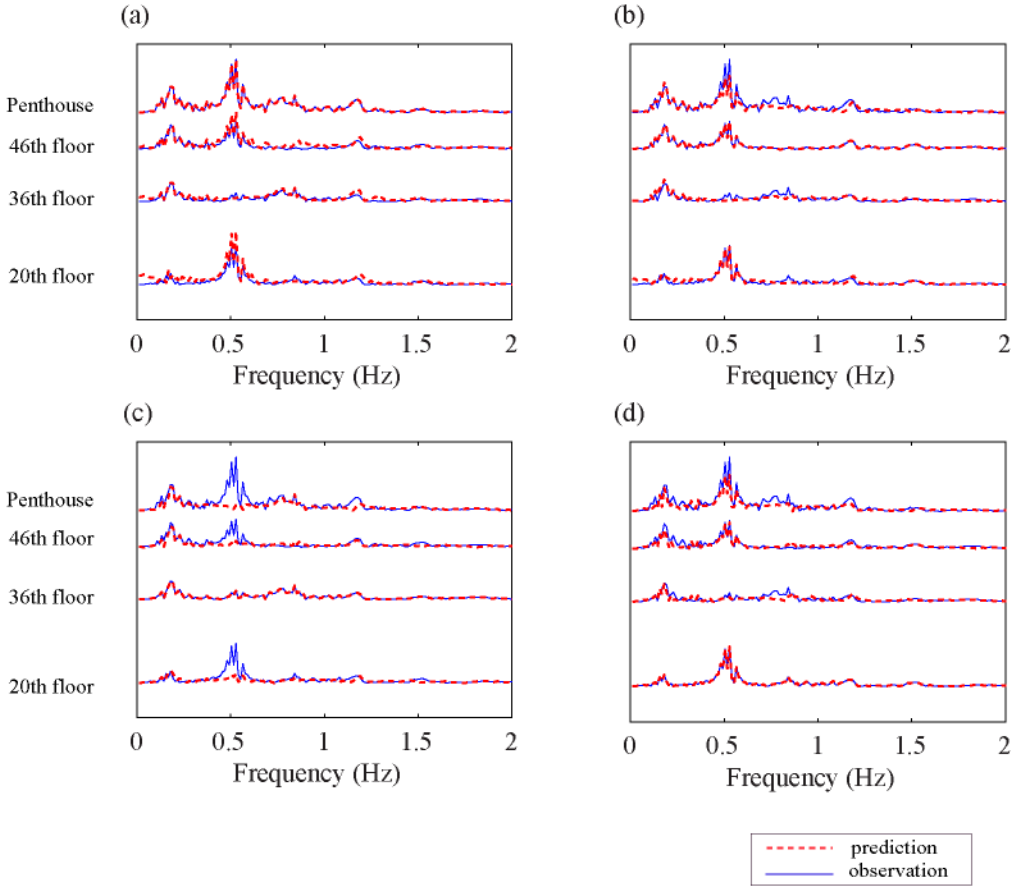

Figure 4.5: Fourier spectra of displacement responses of the 54-story building in the NS direction for the 2008 M5.4 Chino Hills, CA earthquake. (a) Prediction using the record from the penthouse. (b) Prediction using the record from the 46th floor. (c) Prediction using the record from the 36th floor. (d) Prediction using the record from the 20th floor.

Figure 4.6 shows the predicted displacement responses using the same method applied to data recorded from the June 28th, 1992 M6.5 Big Bear, CA earthquake (epicentral distance = 133km) for the same building. Similar conclusions can be drawn. Figure 4.7 shows that the building's displacement response to the April 4th, 2010 M7.2 El Mayor-Cucapah earthquake (epicentral distance = 341km) was significantly larger in absolute amplitude than the two previously considered earthquakes, and the observed ground motion is much longer-period. In this case, the initial ground excitation is not impulsive and the floor responses in the building are mostly in-phase.

The motions for these three earthquakes recorded at the base of this building are compared (Figure 4.8) and their spectral contents, reflected in the duration of the initial impulse of the input ground motion, are observed to vary from broadband for the 2008 Chino Hills earthquake (Figure 4.8a) to intermediate-period for the 1992 Big Bear earthquake (Figure 4.8b) to low-frequency for the 2010 El Mayor–Cucapah earthquake (Figure 4.8c). The initial impulse duration for the 2008 Chino Hills earthquake, the 1992 Big Bear earthquake, and the 2010 El Mayor–Cucapah earthquake are 0.7sec, 1.3sec and 5.7sec, respectively. The fundamental period, T_1, of this building is close to 5.8sec in the NS direction. This observation suggests that when the duration of the initial ground impulse approaches T_1, the initial traveling wave will not occur; instead resonant response from dominant vibrating modes is formed in the building during the ground excitation.

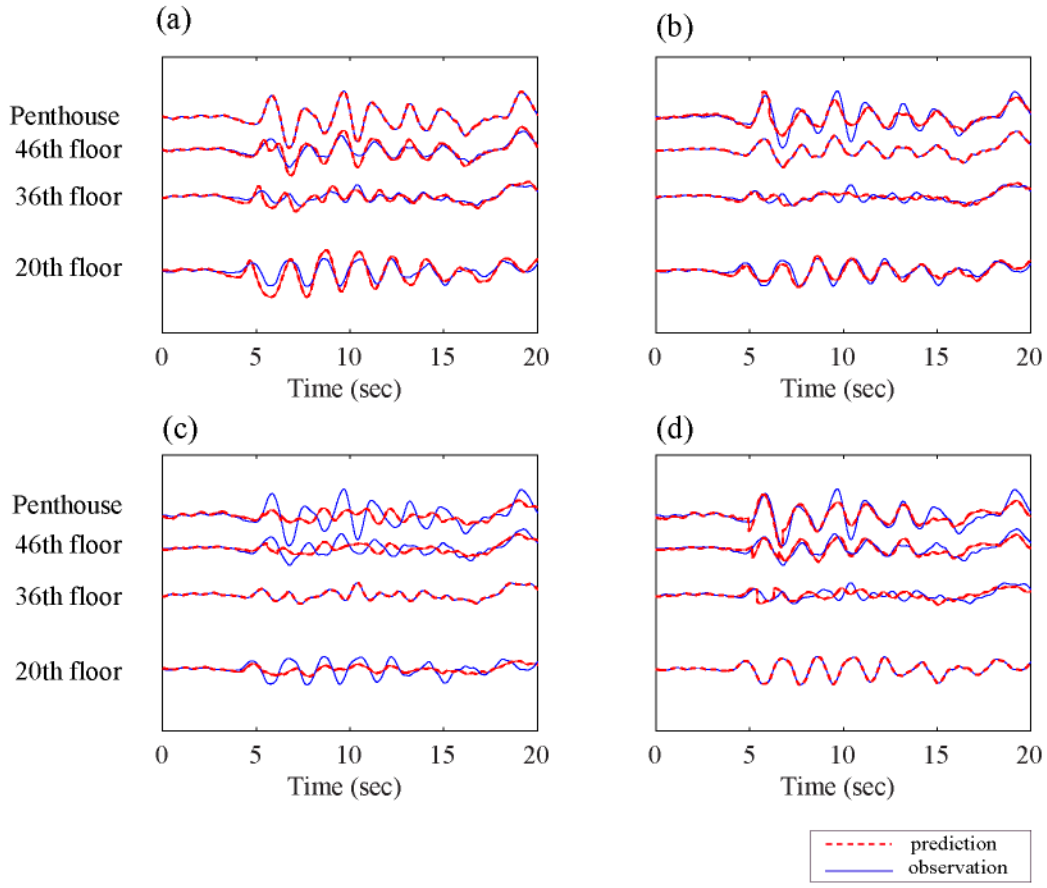

Figure 4.6: Displacement responses of the 54-story building in the NS direction for the 1992 M6.5 Big Bear, CA earthquake. (a) Prediction using the record from the penthouse. (b) Prediction using the record from the 46th floor. (c) Prediction using the record from the 36th floor. (d) Prediction using the record from the 20th floor.

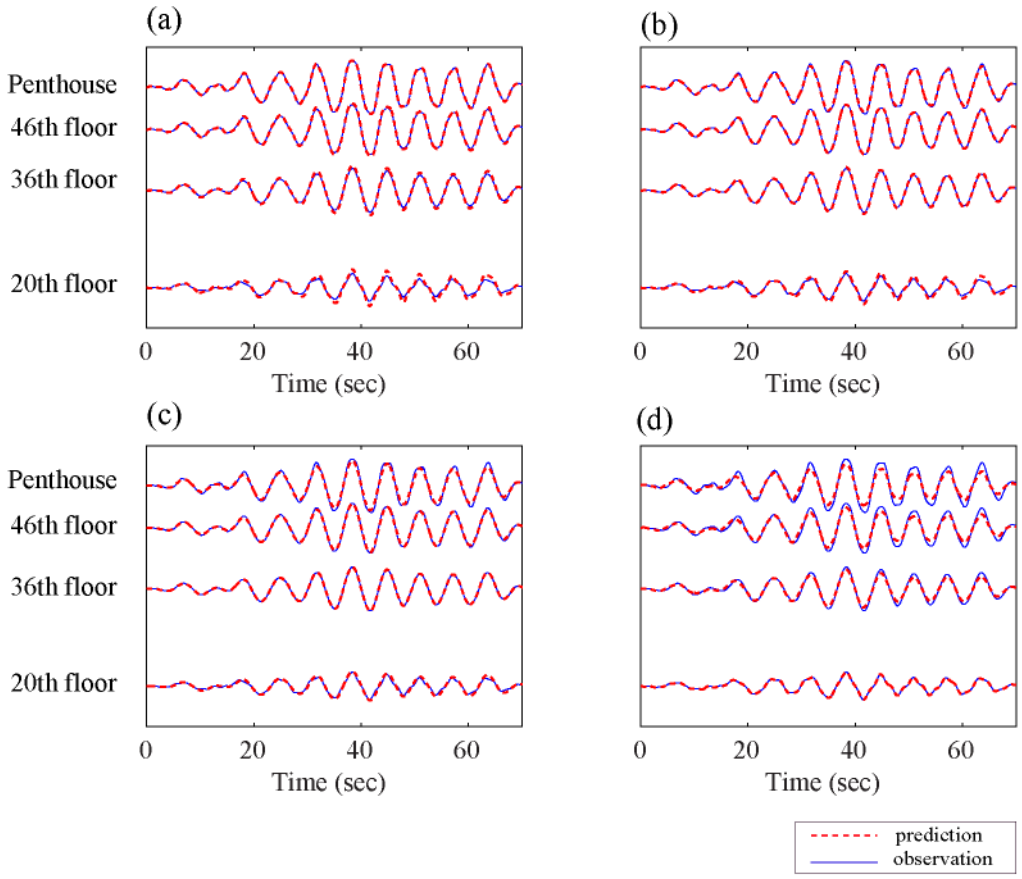

Figure 4.7: Displacement responses of the 54-story building in the NS direction for the 2010 M7.2 El Mayor–Cucapah earthquake based solely on the resonant mode solution. (a) Prediction using the record from the penthouse. (b) Prediction using the record from the 46th floor. (c) Prediction using the record from the 36th floor. (d) Prediction using the record from the 20th floor.

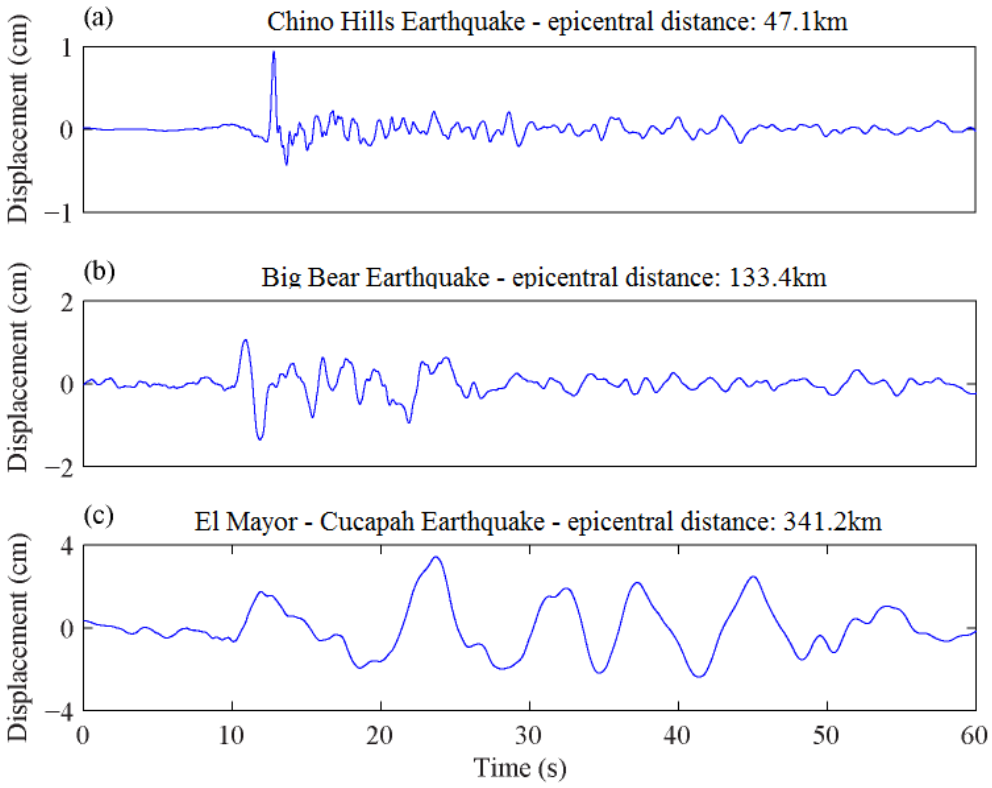

Figure 4.8: Observed displacement at the ground level of the 54-story building in the NS direction for the (a) 2008 Chino Hills, CA earthquake, (b) 1992 Big Bear, CA earthquake, and (c) 2010 El Mayor–Cucapah earthquake.

4.4 VERIFICATION WITH A 3D FINITE-ELEMENT MODEL

To further illustrate and validate the traveling wave behavior of building response, a detailed finite-element model of a building is used to compute the transfer functions for impulsive excitation at the base of the building, i.e., impulse response functions. Impulse response functions have been used extensively in the field of geophysics to capture the property of coherent waves between two seismic stations on the Earth (e.g. Campillo and Paul, 2003; Denolle et al., 2013). Within a building,

impulse response functions describe how waves travel up and down the building, as well as how waves are reflected from large-scale stiffness discontinuities in the building (e.g. Kohler et al., 2007; Ebrahimian and Todorovska, 2013). Moreover, interferometric methods such as ambient noise cross correlations also capture the impulsive response functions within a building, and closely match the shear-wave velocities observed in the earthquake-based impulse response functions (Prieto et al., 2010). In theory, these impulse response functions account only for the wave propagation effect due to elastic properties between any pair of seismometers.

The Doris and Louis Factor building on the UCLA campus is a 17-story steel moment-resisting-frame structure with two basement levels (Figure 4.9). It is an example of a building type that deforms primarily in shear. The first two NS modal frequencies are 0.59Hz and 1.83Hz, while the first two EW modal frequencies are 0.55Hz and 1.70Hz (Kohler et. al., 2007). Kohler et al. (2007) constructed a three-dimensional finite-element model using ETABS (distributed by Computers and Structures Inc.) to study the wave-propagation behavior of the Factor building in the linear elastic regime (Figure 4.10). Details in the model are based on structural engineering drawings of the building. The structural core of Factor building is a double-moment bay and this bay provides the lateral stiffness required to meet the demands of the structure. The other non-moment frames are primarily used to carry gravity load. Moment frames of the building are modeled using beam and column elements with moment-resisting connections; the remaining connections are modeled as pinned connections. Floors and interior walls of the building are replaced with distributed mass elements and the mass is vertically lumped at each floor.

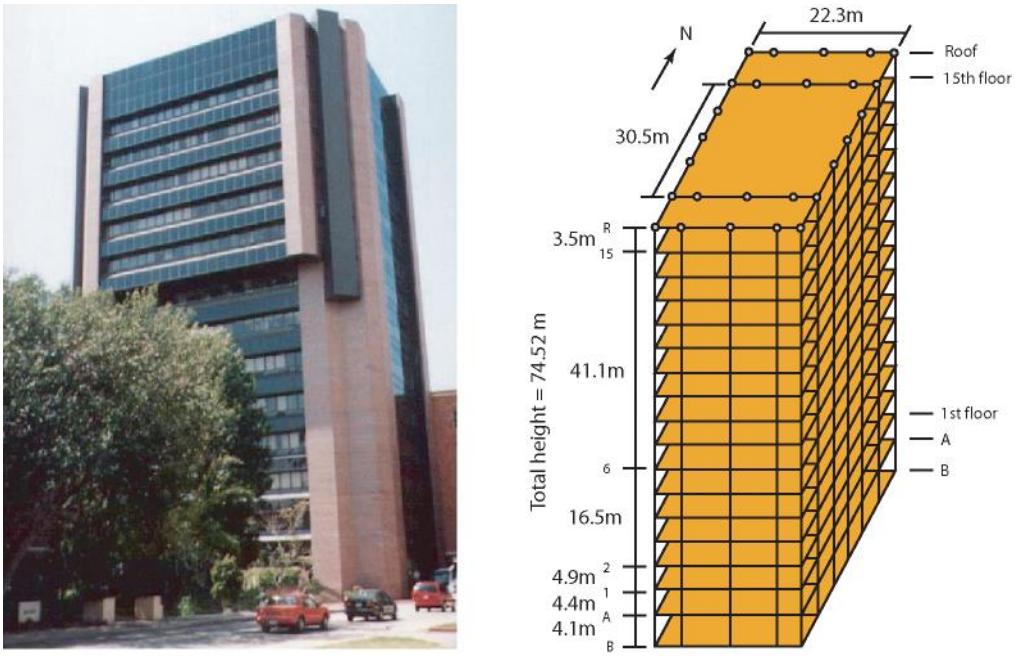

Figure 4.9: UCLA Factor building showing building dimensions and floor heights (from Kohler et al., 2007).

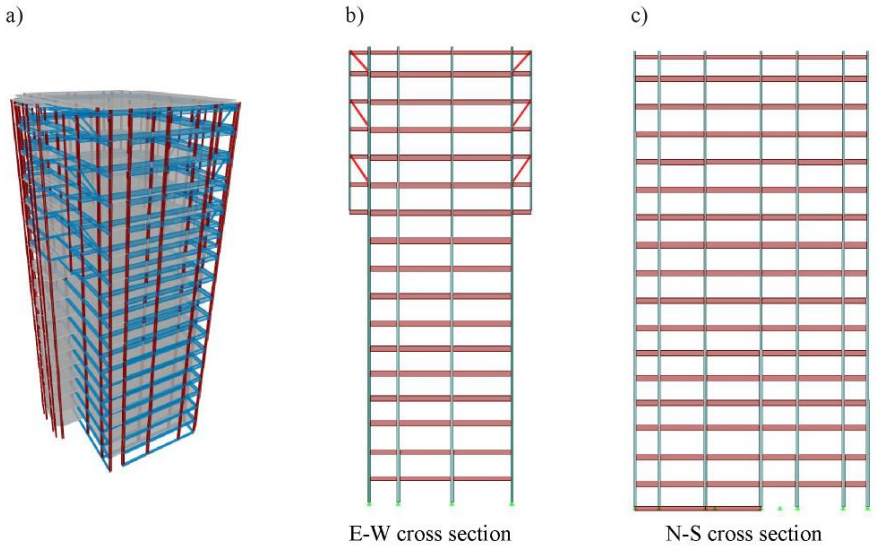

Figure 4.10: ETABS finite-element model of Factor building (from Kohler et al., 2007). (a) Primary major structural elements. (b, c) East-west and North-south cross sections of major structural elements.

A displacement impulse with duration of $T_1/15$ (where T_1 is the fundamental natural period of the building in the NS direction) is inputted at the base of the finite-element model to compute the impulse response functions in the NS direction. First, a relatively small value of $T_1/15$ is used to examine the effects of an impulse duration much less than T_1. Figure 4.11a shows that the impulse is reflected off the underside of the roof as well as at the base of the building. Initially, the impulse takes time = $T_1/4$ to travel up the building from the base, which exactly equals the time required by a theoretical shear beam. The impulse maintains its amplitude and phase as it travels vertically from the base to the roof. When it arrives at the roof, constructive interference between the initial upward and the reflecting waves occur. Afterwards, wave attenuation and dispersion become significant. Because different frequency components of that impulse begin to travel at different speeds with reduced amplitudes, the impulse cannot maintain its initial shape.

In theory, we can convolve the impulse response functions with any earthquake ground motions to obtain the linear-elastic response of each floor. Figure 4.11b shows the simulated displacement response for the Factor model in the NS direction for the 2008 Chino Hills earthquake. Similar to the impulse response functions, an impulse first travels up the building with consistent amplitude and phase. After it is reflected from the roof of the building, the impulse cannot maintain its initial shape. While the earthquake triggers continuous motion at the base of the building, standing waves (associated with the vibrating modes of the building) due to upward and downward traveling waves are formed. Modal response in displacement is typically dominated by the first 2-3 resonant vibrating modes of the building (e.g. Chopra and Goel, 2004). In particular, if the modal response is dominated by the fundamental mode, this phenomenon is observed in the in-phase motions of all floors. For example, the initial wave crests on all floors occur nearly instantaneously at $t \cong 2.5$sec (Figure 4.11b).

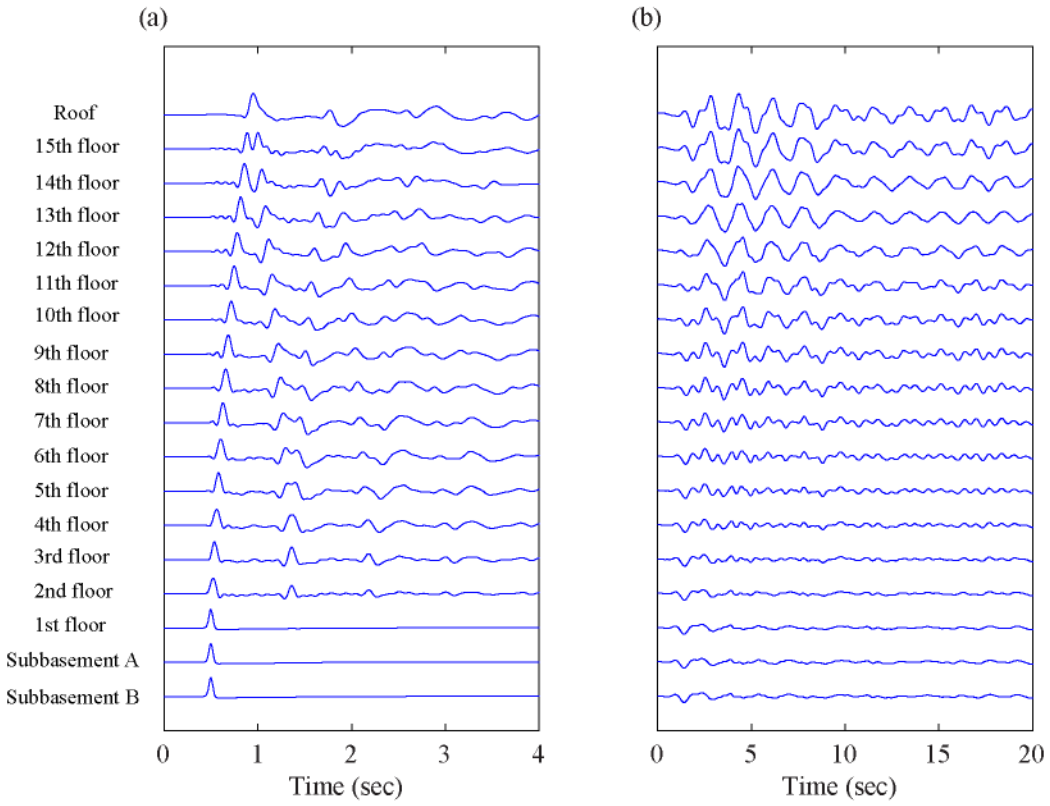

Figure 4.11: Simulation results using the Factor building finite-element model. (a) Impulse response functions. (b) Simulated displacement responses in the NS direction for the 2008 Chino Hills, CA earthquake. The vertical locations of the records are shown by the floor levels. Displacement for the time series are normalized to the same scale by the response at the roof which has a maximum absolute displacement = 7.4mm and minimum absolute displacement = -6.9mm.

4.5 EFFECT OF IMPULSE DURATION ON TRAVELING WAVE

The Factor model is used to investigate the effect of initial impulse duration in the ground motion on the building response (Figure 4.12). For impulse duration time much smaller than T_1, the initial upward traveling impulse is observed and it takes time = $T_1/4$ to travel from the base to the roof of the building with subsequent response dominated by the resonant modes (Figure 4.12a).

Similar simulation results are observed for increasingly long impulse duration times (time = $T_1/2$ as shown in Figure 4.12b), until the impulse duration approaches T_1 (Figure 4.12c). When the impulse duration is larger than T_1, resonant modes (in-phase motions) are mixed into the initial upward traveling impulse. The initial impulse now takes less time to travel from the base to the roof of the building. For example, the travel time from base to roof is $T_1/5.5$ for an impulse with duration of $1.5T_1$. When the initial impulse duration time is long enough (time = $2.5T_1$) and longer than the fundamental period, the building oscillates in phase with the ground motion like a rigid body, and the initial upward traveling wave is no longer observed (Figure 4.12d).

Construction of accurate, detailed three-dimensional finite-element models of instrumented buildings depends on the access to structural engineering drawings of the buildings which are often not available. If a building is instrumented on every floor, we can obtain the transfer functions by deconvolving the displacement responses on all floors with the nearby free-field ground motion. In practice this can also be approximated by deconvolving the upper floor displacements with the base motion of the building. This procedure is an approximation because the base of the building is assumed to be fixed during the building's transient motions. If the building is only instrumented with a single seismometer, transfer functions obtained by this method, as well as the relative displacement between each floor's response and the base motion are somewhat less accurate. The numerical results validate the idea of using a single recorded impulse as a template for the traveling wave and applying this template to other floors through an estimated wave speed.

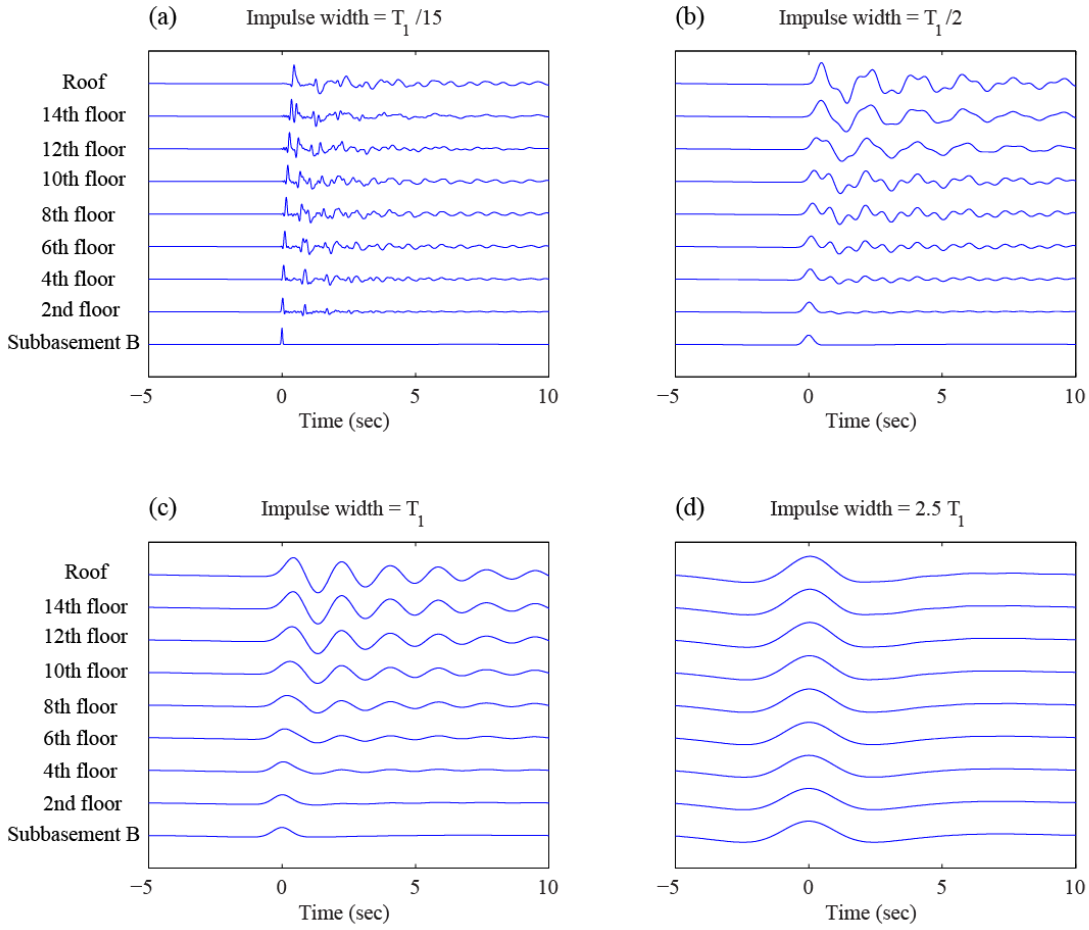

Figure 4.12: Comparison of the effects of varying the impulse duration on the Factor building finite-element model simulation results. (a) Impulse duration = $T_1/15$. (b) Impulse duration = $T_1/2$. (c) Impulse duration = T_1. (d) Impulse duration = $2.5T_1$, where T_1 is the fundamental period of the building.

4.6 CONCLUSION

The main advantages of this method of estimating the linear-elastic displacement response of a building are that it is fast and robust, and that data from only a single seismometer are needed to

provide constraints. Differential equations associated with dynamic response theory are not required to compute the displacement response. The initial upward traveling impulse can be approximated by the wave solution and the impulse velocity is related to the fundamental period of the building. The subsequent displacement response can be approximated by the resonant mode solution which can be extracted from the observations with appropriate band-pass filters. Our results illustrate that the roof is the best choice for instrumentation because this location is not a nodal point in any resonant modes; thus it will capture all the dominant modal responses during a seismic event. Our case study with the 54-story building shows that a sensor located on lower floors will not affect the displacement response predictability unless the single station is located on a floor level near a nodal point of the dominant resonant modes.

The duration of the ground motion impulse has a pronounced effect on the relative significance of the traveling wave. The impulse is expected to take the time = $T_1/4$ to travel from the base to the roof of the building. If the impulse duration is less than $T_1/4$, initial traveling of the impulse will be observed in the floor responses, and maximum floor response may occur during this period before the resonant mode response dominates. If the impulse duration is long enough, the building will oscillate in phase with the ground motion like a rigid body, and the initial upward traveling wave will not be observed. This phenomenon happens when impulse duration approximately equals T_1 for the 54-story building during the 2010 El Mayor-Cucapah earthquake and $2.5T_1$ for the finite-element model of the Factor building.

The method presented here is well-suited to simulate building motions on multiple floors using data from new and expanding crowd-sourced seismic networks, in which volunteers install inexpensive seismometers in their homes and offices in high-rise buildings. The Community Seismic Network (Clayton et al., 2011) and Quake-Catcher Network (Cochran et al., 2009; 2011)

are examples. In a crowd-sourced network, station locations are typically chosen for reasons that are unrelated to, and may not be able to take advantage of, the optimal design and configuration of a seismic network. Furthermore, there may be instances in which a single seismometer is the only data stream available from a building. Our method indicates that even one data stream input can be suitable for estimating the entire-building response. In addition, our modeling results can be imported into 4D spatial-time visualizations of building responses due to an earthquake or other shaking event. These products can raise the social interest in, and awareness of, the earthquake hazard. Visualization products such as movies of floor displacement responses allow the non-scientific community to learn how buildings responded to an earthquake. Kohler et al. (2013; 2014) show that 3D geometry-based models of buildings can be constructed using *SketchUp*, a 3D modeling program initially developed by Google for *GoogleEarth*, and can be easily transferred into 3D mesh models for quantitative processing using, e.g., *Matlab*. Figure 4.13 shows the 3D mesh model for the 54-story building that is used for visualization of earthquake response.

The technique presented here also meets needs in the field of hazard management. For example, roof deformation may be an indirect measure of the intensity of the shaking as well as a potential measure of damage (Crowley et al., 2004; Medina and Krawinkler, 2005). It can provide rapid interpretation of the extent of potential damage by comparing the estimated response to the allowable elastic limit. The intensity of shaking can be estimated for a particular structure when data is available from that structure. Last but not least, this study can be used to develop earthquake early warning applications for buildings, e.g., automated elevator control based on the estimated levels of shaking on different floors (see Chapter 5).

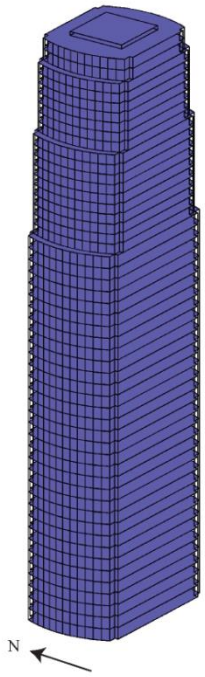

Figure 4.13: 3D mesh model for visualization of the 54-story building response.

C h a p t e r 5

ENGINEERING APPLICATIONS FOR EARTHQUAKE EARLY WARNING

Earthquake Early Warning (EEW) is undergoing a rapid development worldwide with enhanced interest coming after the recent major destructive earthquakes, e.g., the 2008 Wenchuan earthquake in China, the 2010 Haiti earthquake, and the 2011 Tohoku earthquake in Japan. Most regions in Japan are covered by a public earthquake warning broadcast network operated by the Japan Meteorological Agency (JMA) (Allen et al., 2009a; Doi, 2002). Development and testing regarding EEW systems are being performed in China, Mexico, Taiwan, various countries in Europe, and in California where an EEW system, called the California Integrated Seismic Network (CISN) *ShakeAlert*, is currently being developed (http://www.cisn.org/eew/CISN_page.html). *ShakeAlert* combines outputs of three distinct early warning algorithms that are based on different theories: namely τ_c-P_d on-site algorithm (Böse et al., 2009a; Böse et al., 2009b), Earthquake Alarm Systems (ElarmS) (Allen et al., 2009b), and Virtual Seismologist (V-S) (Cua and Heaton, 2007). Figure 5.1 demonstrates a sample user interface of the CISN ShakeAlert System. Detailed information can be found in Böse et al. (2013). In addition, a Smartphone version of such system is currently under development (Faulkner et al., 2013).

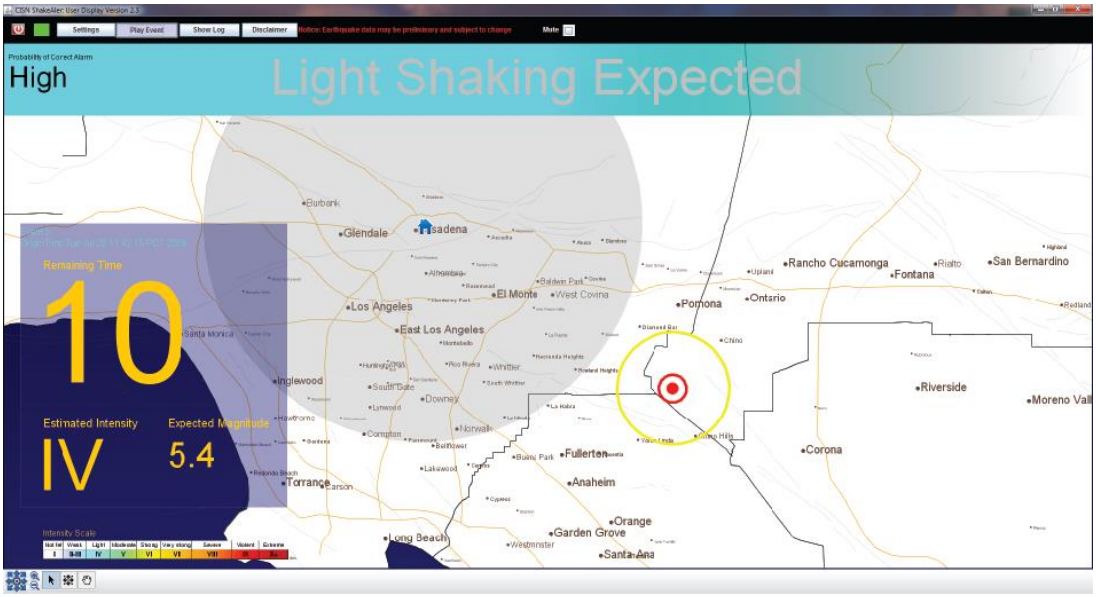

Figure 5.1: Sample of the CISN ShakeAlert user interface.

EEW systems typically provide estimation of earthquake magnitude, epicenter location, and warning time to their users, as well as the estimation of intensity measure (*IM*) at the user's location (Hilbring et al., 2010). However, often a user of such system will be residing in a building. The shaking experienced by a user in a tall building will be significantly different from that on the ground and this shaking can change significantly from one building to another and also from one floor to another. In 2011, during the M9 Tohoku earthquake in Japan, ground motions were amplified by a factor of 3.5 at the roofs of some tall buildings in Tokyo metropolitan area (Kasai et al., 2012). In this chapter, the characteristics of shaking that can be expected in mid- to high-rise buildings using finite element models and time series analysis will be discussed. In the later sections, a probabilistic framework is proposed to develop engineering applications for buildings based on the expected shaking intensity in the building. The computation involved in the proposed decision-making is simple enough that could be handled by a smartphone, which could possibly extend the coverage for earthquake early warning through cellular networks. Users of the EEW system are expected to receive a message including

expected shaking level in case of an earthquake, and such information has shown to be capable of mitigating panic and confusion (Kubo et al., 2011).

5.1 PREDICTION OF SEISMIC INTENSITY IN BUILDINGS

Current state-of-the-art in seismology provides realistic estimate of the time history based on knowledge of the location of an earthquake and a site within a 3-D model of seismic velocities. Strain Green's tensor is used to relate the seismic wave properties between the source location and the user's location. In this section, the fact that Green's functions can be pre-calculated for different source locations and different users' locations using 3-dimensional seismic velocity model in California will be explored. The corresponding building responses at the users' locations are then estimated using finite element and shear beam models. In practice, this information can be pre-computed and stored in a database. Once users provide their street address and which floor they are on, the seismic intensity of this floor can be quickly provided from the database during an earthquake event. The sensitivity of the predicted shaking intensity due to the relative geometry of the earthquake/building pair is explored here. Different locations, including downtown Los Angeles (a site with many tall buildings), West Pasadena (a hard rock site), and the inter-change between I-90 and I-710 (a Los Angeles basin site) are adopted.

5.1.1 GROUND MOTION MODEL

In this study, an earthquake is approximately modeled as a point double-couple source. This approximation is inappropriate for ruptures that exceed 20km in length. Long rupture is a far more challenging problem that is left for future work. Seismic events in the magnitude M5 to M6 range are targeted. There will be tens of these events in the coming decade, and at least some of

these events will cause anxiety to occupants of tall buildings. The long-period motions from a point source of any orientation can be obtained from the appropriate linear combination of the strain Green's function (or alternatively, the moment tensor Green's functions).

Strain Green's tensors used for the sites of interest are adopted from the Southern California Earthquake Center's (SCEC) CyberShake project (Graves et al., 2011). The 3-D seismic velocity model used in the calculation is the SCEC Community Velocity Model for Southern California (CVM-S) version 4. To demonstrate how an early warning system for tall buildings might work, three building locations and two different M6 earthquakes on the San Andreas Fault are assumed. The assumed earthquake locations are San Bernardino and Parkfield. The assumed building locations are downtown Los Angeles (a site with many tall buildings), West Pasadena (a hard rock site), and the inter-change between I-90 and I-710 (a Los Angeles basin site) (Figure 5.2). Distances between the earthquake sources and the building sites are presented in Table 5.1.

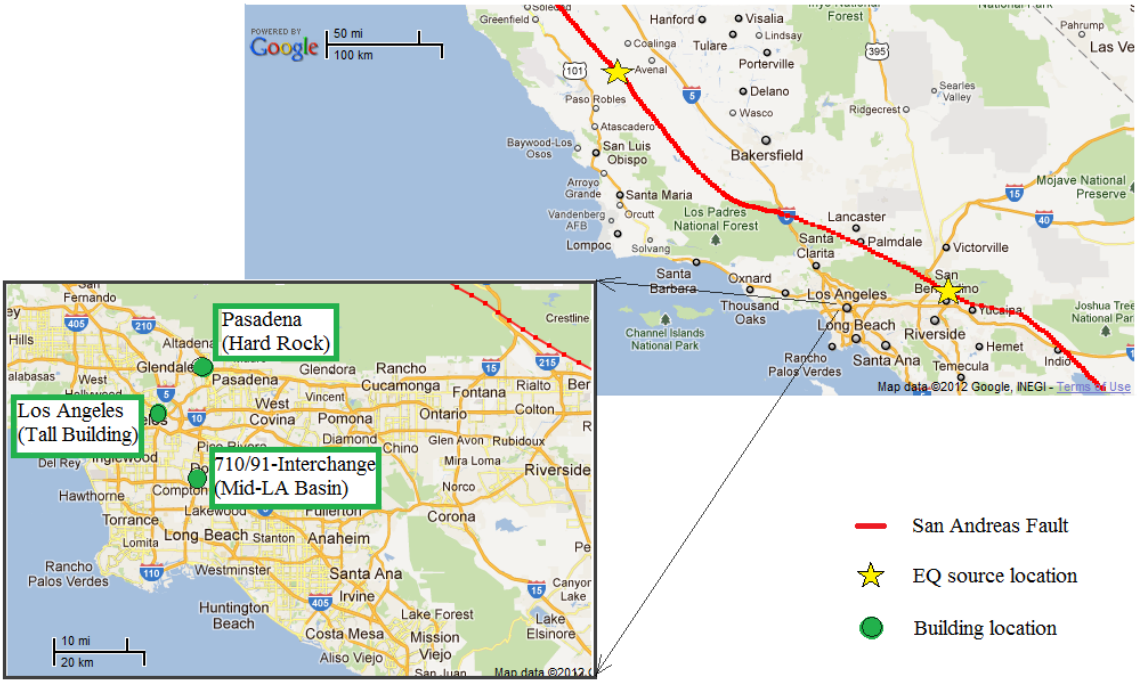

Figure 5.2: Locations of earthquake sources and buildings.

Table 5.1: Distances between earthquake sources and buildings.

		Earthquake source location	
		San Bernardino	Parkfield
Building location	Los Angeles	88km	285km
	Pasadena	78km	284km
	I-710/91	82km	300km

5.1.2 STRUCTURAL MODEL

Two finite element models of steel moment-frame buildings (Figure 5.3), one with 6 stories and another with 20 stories, are used to assess the building responses under earthquakes. Both buildings have story height of 3.81m for every story except the first story that is assumed to be 5.49m. Column spacing is 7.32m for the 6-story building and 6.1m for the 20-story building. The models are designed according to the 1994 Uniform Building Code (Hall, 1997). A36 steel is used in the design of both beams and columns. Design dead loads are 3.83kPa for the roof, 4.55kPa for the floors, and 1.68kPa for the cladding. The floor design live load is 2.39kPa. Gravity load plus wind and gravity loads, as well as seismic loads, are considered in the design. Fundamental natural frequency for the 6-story building is 0.64Hz, while that for the 20-story building is 0.29Hz. Other natural frequencies of the buildings are presented in Table 5.2. More details of the buildings can be found in the report by Hall (1997).

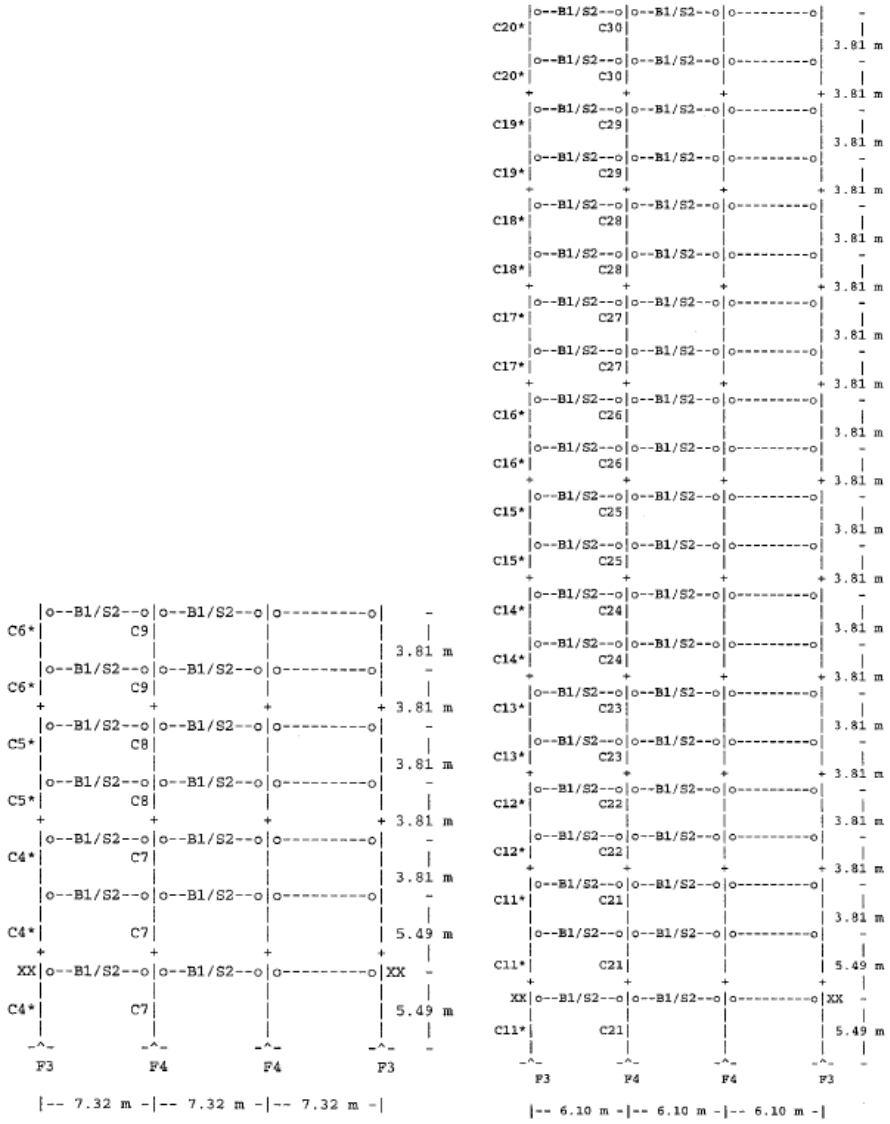

(a) 6-story building (b) 20-story building

Figure 5.3: Finite element models of the 6-story and 20-story buildings. (from Hall, 1997)

Table 5.2: Natural frequencies of the buildings.

	6-story building	20-story building
1st natural frequency (f_1)	0.64Hz	0.29Hz
2nd natural frequency (f_2)	1.81Hz	0.93Hz
3rd natural frequency (f_3)	3.01Hz	1.64Hz
f_2/f_1	2.83	3.21
f_3/f_1	4.71	5.66

5.1.3 HUMAN COMFORT

Human perception of shaking is a complex subject that involves different physiological and psychological factors. Researchers suggest that people are in general insensitive to velocity if visual effects are not considered. It is because no force is required by the body to counter-balance any motions in constant velocity. Instead, people feel force acting on them when they experience acceleration. A continuous adjustment of the body is necessary for a human to adapt to a varying force with changing acceleration during earthquakes. The subject of human comfort thresholds in tall buildings has been widely studied in the past (e.g. Bashor et al., 2005; Boggs, 1997; Griffis, 1993). The relation between human comfort level and peak acceleration is suggested in Table 5.3 (adopted from Griffis, 1993).

Table 5.3: Human comfort level to acceleration.

Peak Acceleration	Comfort level	Early warning message
< 0.5% g	Not perceptible	No shaking
0.5% - 1.5% g	Threshold of perceptible	Minor shaking
1.5% - 5% g	Annoying	Moderate shaking
> 5% g	Very Annoying	Strong shaking

5.1.4 DISCUSSION

As mentioned before, CISN ShakeAlert can estimate the earthquake source location and magnitude when an earthquake strikes. However, the seismic waves transmitted to the user's location are different for different focal mechanisms at a given location of the seismic source and a given seismic magnitude. For each building site, a total set of 27 wave forms are generated for each earthquake location with the following combinations of parameters: dip of 0^o, 45^o, and 90^o;

rake of 0°, 45°, and 90°; and strike of 0°, 45°, and 90°. Earthquake source depth is assumed to be 7km. Although local site effects are taken into account in this study by the 3-D seismic velocity model, there is no soil layer in the model and soil-structure interaction is neglected. Soil resonance at the period of our buildings is probably not a dominant effect, but it would clearly need to be considered in areas with very soft soils.

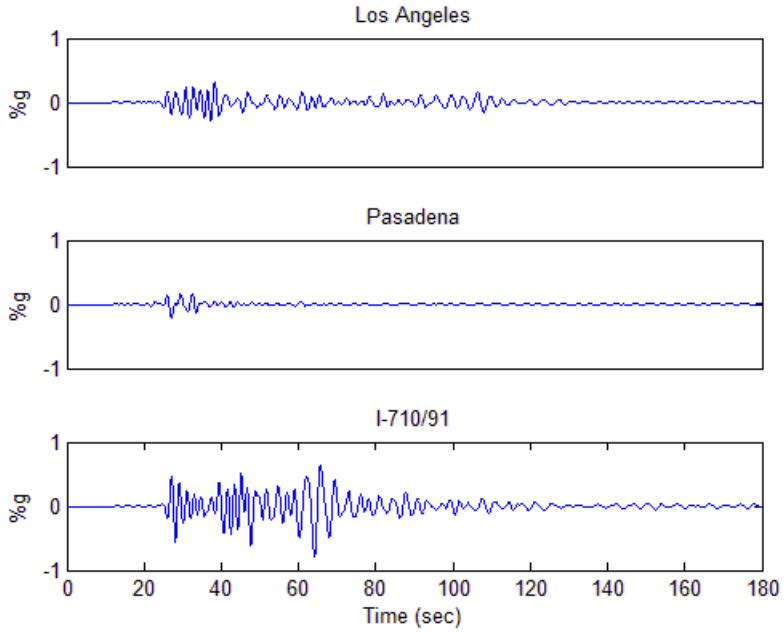

Figure 5.4: Ground motions for different building sites due to a M6 earthquake at San Bernardino with dip = 90°, rake = 180°, and strike = 120°.

Figure 5.4 shows the ground motions for different building sites due to a M6 earthquake at San Bernardino with dip= 90°, rake= 180°, and strike = 120°. Although the three building sites are located at similar distance away from the earthquake source, the effect of the Los Angeles basin, which is seen at the I-710/91, causes the remarkably different ground motion than is seen at the two other sites.

Although the finite element simulations for the buildings include nonlinear effects, the

particular earthquakes were sufficiently small that all of the simulated motions were within the linear elastic range; that is, traditional modal analysis could have been used to simulate the building motions. Furthermore, the modal properties of these buildings can be obtained from a simple shear beam analysis. For example, the natural frequency ratios (the frequency of the i^{th} mode divided by the frequency of the 1st mode) of the 6-story building are 1, 2.83, and 4.71; while that of the 20-story building are 1, 3.21, and 5.66 (Table 5.2). These ratios are very close to the 1, 3, and 5, ratios that a simple fixed-base shear beam exhibits. Building response using continuous shear beam structure has been well studied in the past (e.g. Iwan, 1997; and Sasani et. al, 2006). In the current study, a fixed base shear beam with damping (Roberts and Lutes, 2003) is adopted to simulate the building responses. Damping ratios of 8.5% and 2.5% are selected for the 6-story building and 20-story building, respectively. Comparisons of top-floor and mid-floor acceleration responses for the buildings on the I-710/91 site due to a M6 earthquake at San Bernardino with dip= 90°, rake= 180°, and strike = 120° are presented in Figure 5.5. It shows that for the purpose of estimating the seismic intensity, the result of a regular steel-frame building designed according to UBC code can be well approximated by a shear beam model in the linear elastic regime.

While the acceleration response can be derived by the appropriate modal summation, the response of a uniform shear beam is especially simple if it is written as a summation of vertically propagating shear waves that reflect at the top and the bottom of the building. The acceleration response solution for a fixed-base shear beam with damping (Roberts and Lutes, 2003) is described as follows:

$$\ddot{u}(x,t) = \sum_{k=0}^{\infty}(-1)^k\, e^{-k\pi\xi}\, \ddot{u}_g\left(t - \frac{x}{4Hf} - \frac{k}{2f}\right) - \sum_{k=1}^{\infty}(-1)^k\, e^{-k\pi\xi}\, \ddot{u}_g\left(t - \frac{x}{4Hf} + \frac{k}{2f}\right) \quad (5.1)$$

where $\ddot{u}(x,t)$ is the acceleration response; x is the vertical distance from the ground; H is the

height of the building; ξ is the damping ratio; $\ddot{u}_g(t)$ is the ground acceleration motion; f is the fundamental natural frequency of the building.

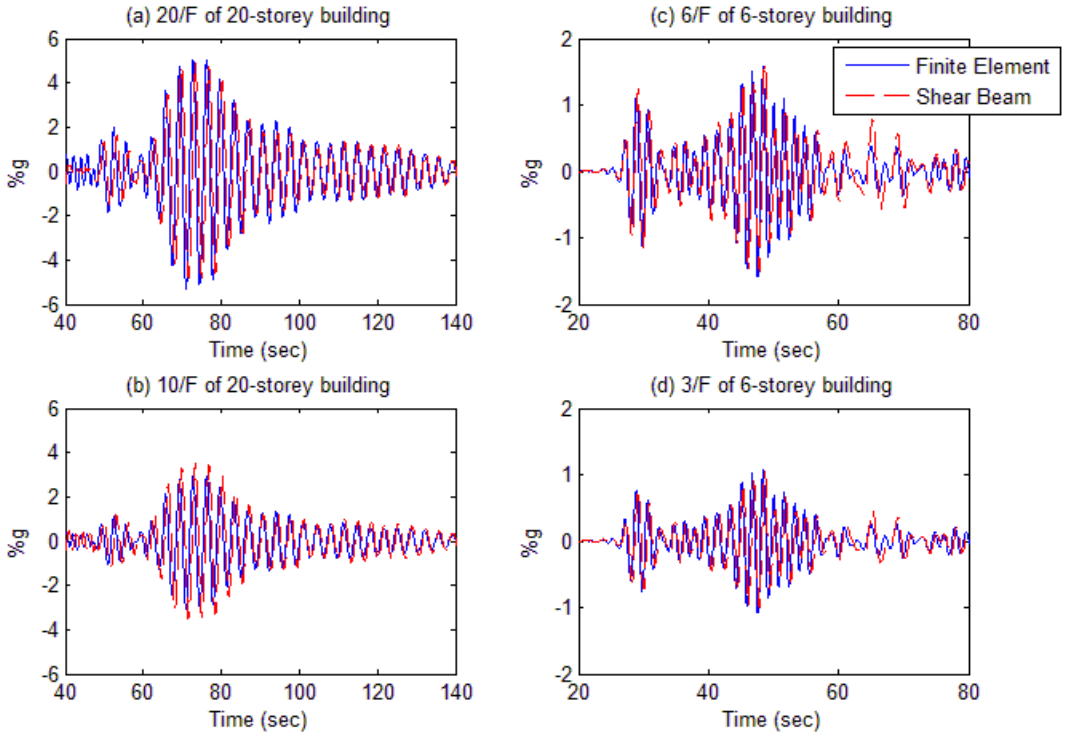

Figure 5.5: Comparison of responses from finite element models and shear beam models for the buildings in I-710/91 assuming a M6 in San Bernardino with dip = 90°, rake = 180°, and strike = 120°. (a) Response at 20/F of 20-story building; (b) Response at 10/F of 20-story building; (c) Response at 6/F of 6-story building; (d) Response at 3/F of 6-story building.

27 simulations are generated for each floor of a building for each earthquake source location. As a demonstration of the proposed methodology, an equally weighted mean is taken for the responses on each floor to get the average floor acceleration response on a building. In the future, more weight can be put on those directions of a point source with high probability of rupture. For the sake of estimating human discomfort and anxiety, the direction of acceleration does not matter, so the envelope of the average floor acceleration responses are used to determine the

seismic shaking levels (Figures 5.6-5.7). Peak acceleration of the record on each floor is compared to the level of human comfort given in Table 5.3, then an appropriate early warning message is sent to the user.

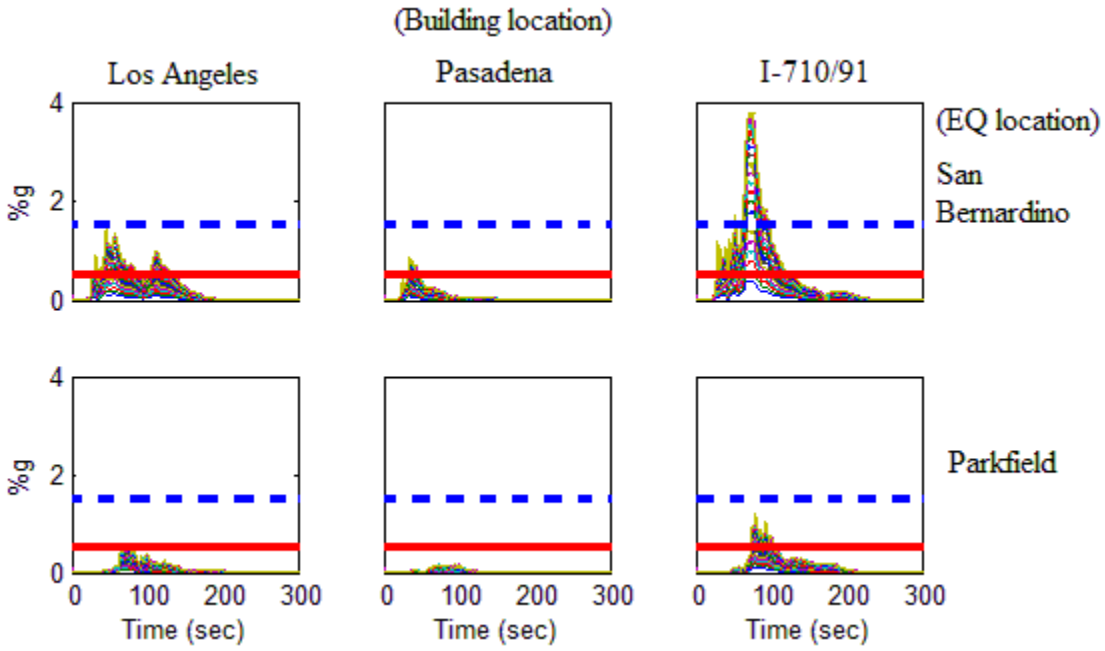

Figure 5.6: Seismic shaking level for 20-story building. 20 curves on each plot correspond to different floor acceleration responses. (Blue dotted line: threshold for moderate shaking; Red solid line: threshold for minor shaking).

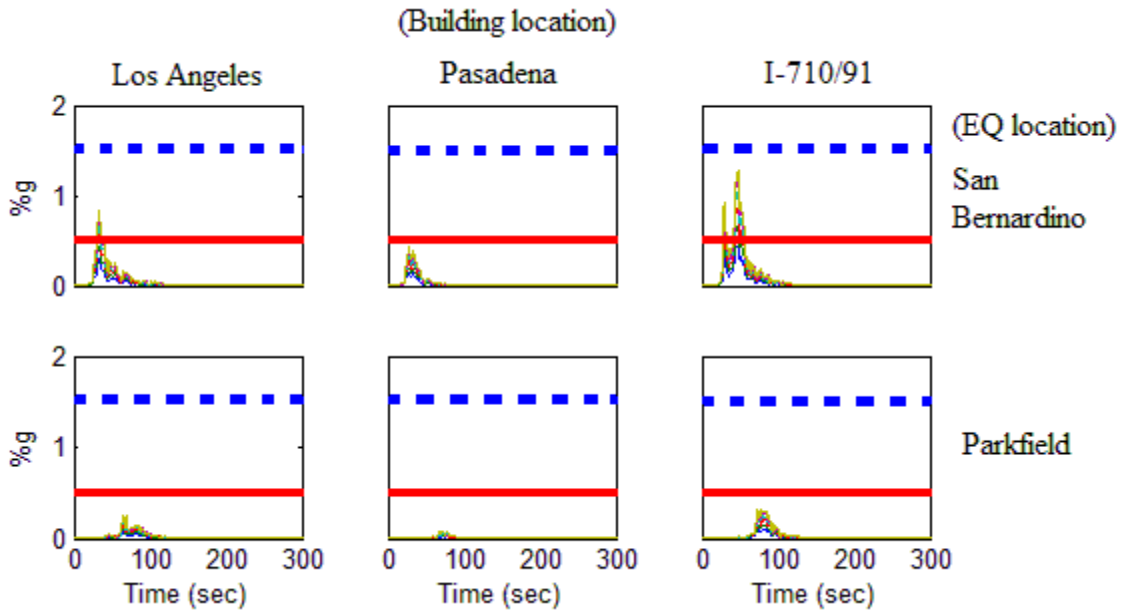

Figure 5.7: Seismic shaking level for 6-story building. 6 curves on each plot correspond to different floor acceleration responses.

Time series analysis can provide information on shaking duration, which empirical methods (e.g., Ground Motion Prediction Equation) cannot. The time length for which the acceleration record is higher than the threshold for shaking perception (0.5% g) is taken as the expected shaking duration. For example, a person on the 10th floor of a 20-story building at I-710/91 will receive the following sample early warning message when an earthquake in San Bernardino strikes: "Moderate shaking coming in x seconds. Please remain calm and stay away from the windows. The building will continue to sway for approximately 100 seconds." (Note: the x seconds are provided by the CISN ShakeAlert decision module, and this time value will be updated and counted down in the User Display).

5.2 DECISION-MAKING FRAMEWORK

Cheng, M. H., S. Wu, T. H. Heaton, and J. L. Beck, 2014. Earthquake early warning application to buildings, Engineering Structures 60, 155-164.

The information provided by earthquake early warning may be used by decision makers to perform appropriate emergency response. The decision may involve a complicated tradeoff between the potential costs of missed alarms and false alarms due to uncertainties in EEW estimation. As the warning time is usually very short, ranging from a few seconds to a minute or so, an automated decision-making approach is needed. Such automation is commonly based on a cost-benefit framework. Several researchers have addressed the need of a complete end-to-end framework (from seismic hazard warning information to loss models for decision making) in earthquake early warning applications based on Pacific Earthquake Engineering Research Center's (PEER) Performance-based Earthquake Engineering (PBEE) methodology (Grasso et al., 2007; Iervolino et al., 2007; Wu et al., 2013). This idea is known as the Performance-based Earthquake Early Warning (PBEEW) (Grasso, 2005). Figure 5.8 shows the general structure of decision making with PBEEW. Choice of ground motion model, structural model, fragility model, and loss model for decision-making can be customized depending on the specific context of an application or users' demands. In this section, the focus will be on building-specific EEW applications. A combination of structural and fragility models are used to extend the ground shaking prediction from EEW to an early warning of building shaking intensity.

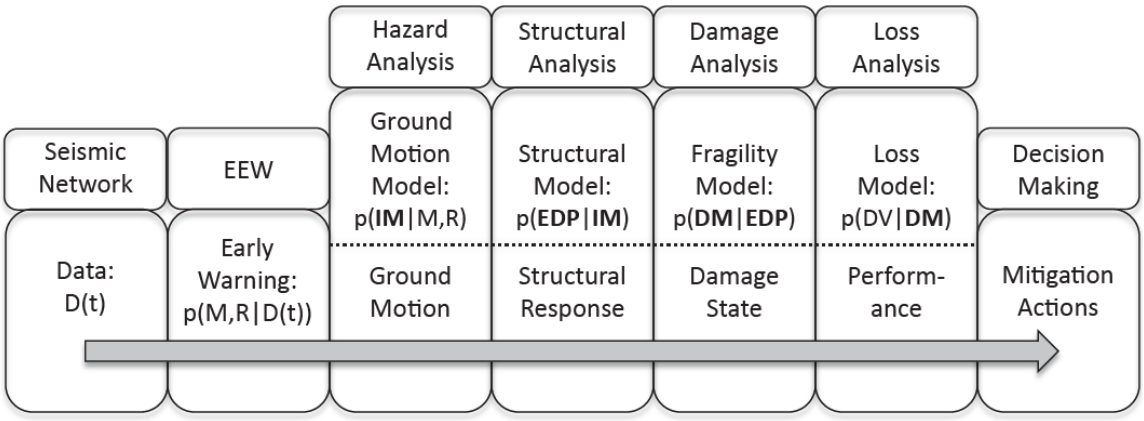

Figure 5.8: Information flow of PBEEW. M is earthquake magnitude, R is epicentral distance from the user's location; IM is intensity measure (e.g. *PGA*, *PGV*, S_a); EDP is engineering demand parameter (e.g. floor acceleration, inter-story drift); DM is measure of damage; DV is decision variable.

Existing ground motion models include Ground Motion Prediction Equations (GMPE) and physics-based three-dimensional ground motion simulation models. For example, the CyberShake (Graves et al., 2011) project developed physics-based model that allows simulation of ground motion time-series at a specific site in Southern California. The advantage of a physics-based approach over GMPE is that the ground motion response explicitly captures earthquake rupture and wave propagation effects. Results from Graves et al. (2011) indicate that when a physics-based model is utilized in seismic hazard analysis, the hazard level is higher for some sites compared to that given by a conventional GMPE, due to the incorporation of rupture directivity and basin response effects. However, a significant amount of computational effort is involved in the physics-based approach. On the other hand, five sets of GMPEs have been developed as a part of the PEER's Next Generation Attenuation model (NGA) project (Abrahamson and Silva, 2008; Boore and Atkinson, 2008; Campbell and Bozorgnia, 2008; Chiou and Youngs, 2008; Idriss, 2008). These GMPEs are attenuation equations in which the site location is parameterized by a relative location with respect to the source (which depends on the fault geometry), the site

conditions (e.g. V_{s30}, the local average of the shear velocity in the upper 30m) and, in some cases, the local depth of the sedimentary basin (Abrahamson and Silva, 2008; Campbell and Bozorgnia, 2008; Chiou and Youngs, 2008). These parameterizations in the GMPEs are determined by empirical regressions of assumed functional forms given the available data. As opposed to the physics-based method, GMPE just provides a ground motion intensity measure (e.g. peak ground acceleration, spectral acceleration, etc.), and the computational effort involved is considerably reduced. Nevertheless, in the framework to be presented here, results from sophisticated physics-based models could be pre-computed and stored in a database for certain sites to improve prediction accuracy and computational efficiency for real time application (as discussed in Section 5.1).

Estimation of floor vibration response of buildings due to earthquakes has been extensively studied in the past. Three-dimensional finite element structural models can be adopted if detailed documentation of the building plans is available (Lee and Ahn, 2011). Similarly, if the dynamic properties of a building, e.g., mode shape, modal damping, and modal frequencies, are known, a mathematical approach using modal decomposition can be used (Chopra, 2007). In the absence of much information about a structure, its building response can be approximated by a simple continuum structural model (e.g. the shear beam model (Iwan, 1997); or a continuum model consisting of a flexural cantilever beam and a shear cantilever beam (Miranda and Taghavi, 2005); or the Timoshenko beam model (see Chapter 3)). These beam models can be defined by the knowledge of as few as the first two natural frequencies of a building, and the corresponding higher mode responses are automatically incorporated in the models. In general, finite element and modal decomposition models will give more accurate results, but they involve detailed information of the building and significantly more computational effort. To provide a quick solution in the application of EEW, results of floor intensity can be pre-computed for various

predicted earthquakes and stored in a database (as discussed in Section 5.1). In the subsequent sections, an illustrative example using the simple continuous beam approach is provided. Furthermore, the proposed framework presented here could provide preliminary damage assessments of buildings if the corresponding fragility models have been developed.

PBEEW uses a probabilistic approach to provide early warning based on ground motion estimation and building shaking intensity prediction. To make a decision about emergency response based on early warning information, this information has to pass through an automated decision-making module with a pre-defined decision criterion. Depending on the application, different kinds of decision criteria can be used. Possible applications based on the acceleration response in buildings include the following: 1) Early warning of floor shaking sensed by occupants; 2) Elevator control; 3) Emergency shutdown of sensitive machinery; and 4) Early warning of potential non-structural element damage.

Different decision criteria affect the robustness and efficiency of the decision-making process. Complexity of decision criteria range from the simplest mean value oriented decision (taking action when the mean of a target variable exceeds a threshold value) to a full cost-benefit analysis of the emergency response. More complicated decision criteria lead to more flexible decision behavior, but require more effort to setup and compute (Wu et al., 2013). Referring to Figure 5.8, only the hazard analysis and structural analysis stages are considered in this study, since damage analysis and loss analysis are irrelevant for the proposed applications. For the example in a later section, the decision criterion is a function of an expected utility value of the engineering demand parameter (*EDP*), $E[U(EDP)]$, which is calculated based on the PBEEW methodology by:

$$E[U(EDP)] = \iint U(EDP)\, p(EDP|IM) p(IM)\, dEDP\, dIM \tag{5.2}$$

where *IM* denotes the intensity measure, $p(IM)$ is the PDF (probability density function) for the intensity measure prediction from EEW and the response prediction PDF $p(EDP|IM)$ typically involves the structural model.

In this chapter, applications to human comfort and elevator control are selected to demonstrate how the proposed PBEEW framework can be applied.

5.2.1 HUMAN COMFORT

As discussed in Section 5.4, humans are sensitive to acceleration. Typically, the comfort level is determined by the mean value of the predicted peak floor acceleration (*PFA*) as given by its PDF, $p(PFA)$. In many engineering applications, *PFA* is described by a log-normal distribution; hence, this decision criterion is equivalent to determining the comfort level for the 50^{th} percentile of *PFA* from the cumulative density function (CDF) of ln *PFA* (the value of *PFA* below which there is a 0.50 probability). This is named the *mean-value method*. Another possible decision criterion is to determine the comfort level as the most probable comfort level calculated from $p(PFA)$, which is equivalent to determine the interval that contains the largest area under the $p(PFA)$ curve. The total area under the $p(PFA)$ curve is 1, and the range of $PFA \in (0, \infty)$ is divided into four intervals according to Table 5.3. This is named the *most-probable method*.

5.2.2 ELEVATOR CONTROL

Modern mid- to high-rise buildings typically feature elevators and occupants use them extensively, so any life safety issues associated with them cannot be ignored. Potential seismic risks for elevators include cab door damage, equipment anchorage damage, counterweights falling out of

their guide rails, etc. Regarding regulation standards, the State of California (Cal/OSHA) requires the installation of an earthquake sensing device on every single elevator. This device will trigger a shut down if more than 0.5g of acceleration is detected. In contrast, Japanese elevator regulation requires elevators to stop operation at a much lower threshold, 0.08g to 0.15g of acceleration depending on building properties and elevator location (Kubo et al., 2011).

In the case of EEW, a PDF of *PFA* can be constructed, and a typical decision-making approach is to stop the elevator when the mean of *PFA* exceeds a certain threshold value PFA_0, depending on the regulations. Another commonly adopted probabilistic approach is to stop the elevator when the probability of ($PFA > PFA_0$) exceeds a threshold value P_0.

5.2.3 EXAMPLE

In the following sections, an existing GMPE and a simple structural model combining the behavior of flexural and shear cantilever beams will be used to illustrate the use of the proposed probabilistic decision making framework, although users can pick any ground motion model and structural model appropriate to their decision objectives.

5.2.4 GROUND MOTION MODEL

The GMPE developed by Boore and Atkinson (2008) is used as the ground motion model for this example, which is appropriate for earthquakes in California. In particular, the equation for the predicted ground motion is:

$$lnY = F_M(M) + F_D\left(R_{JB}, M\right) + F_S\left(V_{s30}, R_{JB}, M\right) + \varepsilon\sigma_T \tag{5.3}$$

where Y, F_M, F_D, and F_S represent the intensity measure (peak ground acceleration *PGA* is used in this example), magnitude scaling function, distance function, and site amplification function; M is the moment magnitude; R_{JB} is the Joyner-Boore distance; and V_{S30} is the inverse of the average shear-wave slowness from the surface to a depth of 30m; $\varepsilon\sigma_T$ is a zero-mean Gaussian error term with standard deviation σ_T. This GMPE model is selected because of two reasons: first, this model is simple enough that it can easily take the output from ShakeAlert as input, i.e., R_{JB} and M, and Vs_{30} is a known value for any user's location; and second, this GMPE model allows *PGA* to be integrated out analytically when predicting *PFA* based on the structural model below (see also Section 5.3.2).

5.2.5 STRUCTURAL MODEL

To demonstrate the use of the proposed decision-making framework, a generic building model that can readily predict peak floor accelerations is required. A continuum model that combines a flexural cantilever beam and a shear cantilever beam (Miranda and Taghavi, 2005) is adopted in this example. It is understood that this structural model inherits some limitations and assumptions, such as linear elastic behavior and classical damping. Also, tall buildings are more sensitive to long-period accelerations, while short buildings are more sensitive to high-frequency accelerations. Therefore, the estimation of *PFA* based on *PGA* by the model (Miranda and Taghavi, 2005) may not be the best choice, because *PGA* is controlled by high-frequency components of the ground motion (Malhotra, 2006). However, this ground motion model is selected in this study because a probability distribution for *PFA* given *PGA* is available (Taghavi, 2006) and the log-normally distributed *PFA* forms a conjugate analytically integrable pair with *PGA* in the GMPE model as mentioned before. Once again, the models chosen here are used to

illustrate the decision-making framework; users can pick any appropriate ground motion model and structural model.

The chosen model can be fully defined by four parameters: fundamental period of the building T_1, modal damping ratio ξ, lateral stiffness ratio α_0, and lateral stiffness reduction ratio δ. The dimensionless parameter α_0 describes the participation of shear and flexural deformations in the model, which affects the lateral deflected shape of the building. The other dimensionless parameter δ describes the variation of lateral stiffness along the building height. Taghavi (2006) concluded that lateral stiffness reduction has negligible effect on the prediction of floor responses, so $\delta = 1$ is used (i.e. uniform stiffness along the height). A typical value of modal damping ratio $\xi = 5\%$ is selected. As suggested by Miranda and Reyes (2002), $\alpha_0 = 12.5$ is used for moment resisting frame buildings; $\alpha_0 = 3.125$ is used for dual system (e.g. resisting frame and shear wall) buildings; and $\alpha_0 = 1$ is used for shear wall buildings. The fundamental period T_1 needs to be estimated for each building; for example, by using the crowd-sourced seismic networks (e.g. Quake Catchers Network (Cochran et al., 2011) and the Community Seismic Network (Clayton et al., 2011)). The fundamental period T_1 can be estimated by spectral peak-picking or by more sophisticated system identification techniques such as deterministic-stochastic subspace system identification using the recorded data from ambient vibration or small magnitude earthquakes (Alvin et al., 2003). Taghavi (2006) did a parameter study on this structural model to summarize the effect of peak floor acceleration given peak ground acceleration. In his simulation, Taghavi adopted a set of 80 ground motions with earthquake magnitudes ranging from M5.8 to M6.9; epicentral distances ranging from 13km to 60km; and peak ground accelerations ranging from 0.03g to 0.44g. Figure 5.9 shows the mean value of $\ln(PFA/PGA)$ along the building height. Since logarithm scale is involved, a positive value of $\ln(PFA/PGA)$ means the *PFA* value is magnified

comparing to *PGA*, while a negative value means *PFA* is reduced. Figure 5.10 shows the standard deviation of ln(*PFA*/*PGA*).

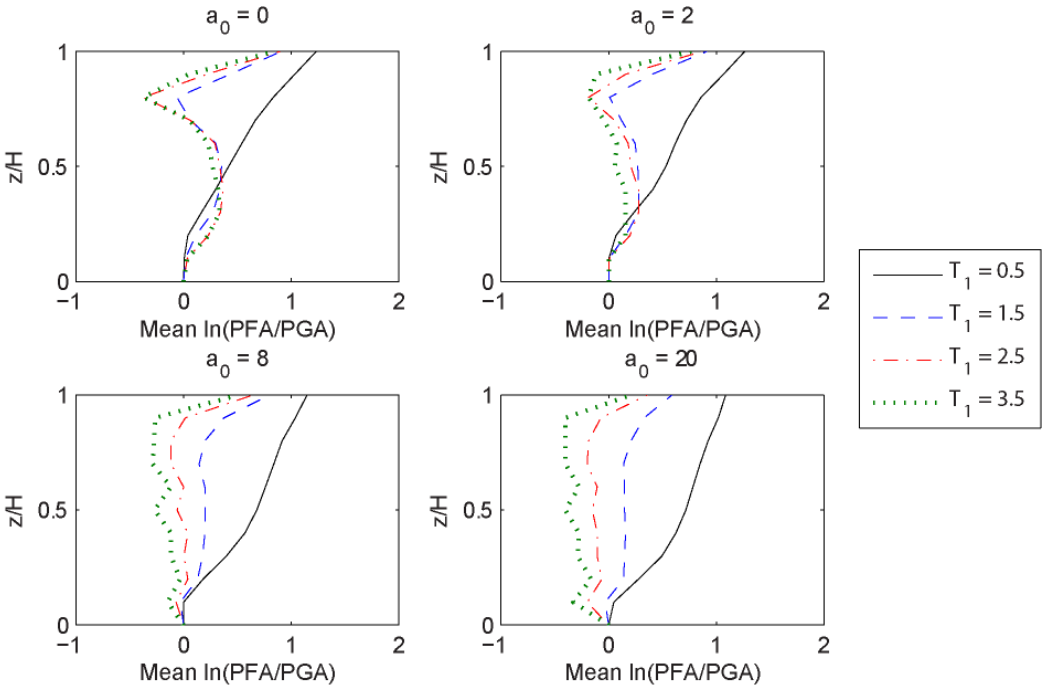

Figure 5.9: Mean of floor acceleration demand (from Taghavi, 2006). *z* is the height of the level considered; *H* is the total height of a building; and α_0 is the lateral stiffness ratio.

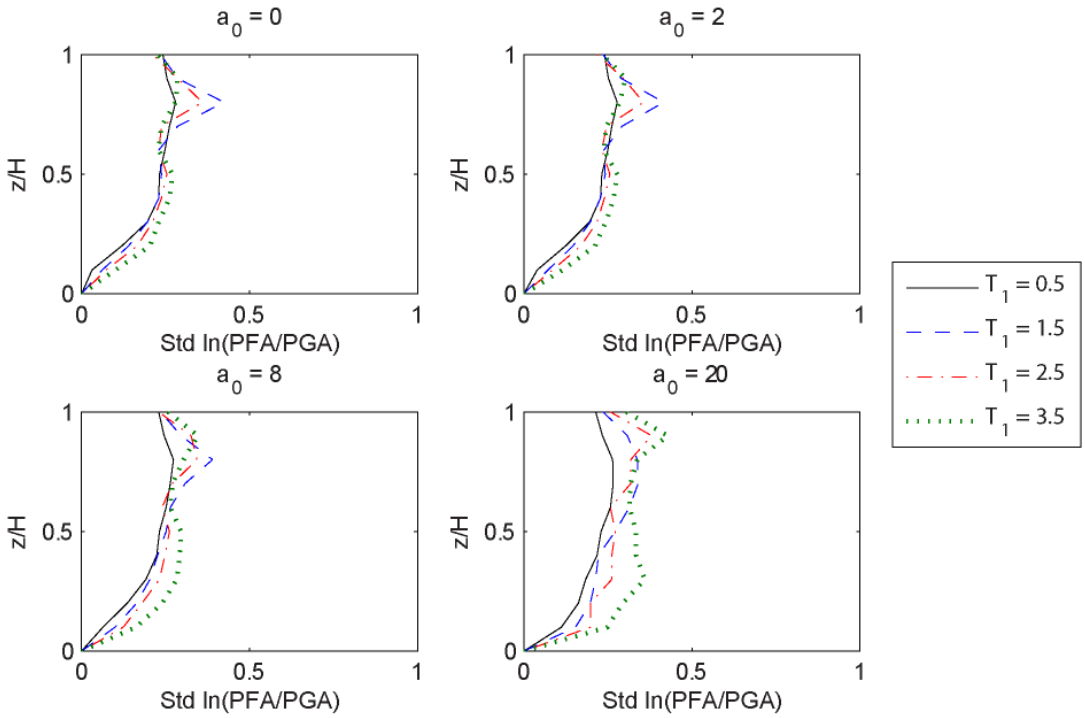

Figure 5.10: Standard deviation of floor acceleration demand (from Taghavi, 2006). z is the height of the level considered; H is the total height of a building; and α_0 is lateral stiffness ratio.

5.2.6 EARTHQUAKE DATA

Seismic records are extracted from the California Strong Motion Instrumentation Program (CSMIP) database (http://www.strongmotioncenter.org/) (see Appendix B). Data from the buildings that meet the following criteria are used in this study:

1. Reinforced concrete or steel buildings;

2. Mid-rise structures (4-7 stories) or high-rise structures (≥ 8 stories);

3. Buildings were designed after the introduction of earthquake-resistant design codes in California;

4. Buildings that have at least three available earthquake records, and $PFA \geq 0.2$g for at least one of these earthquakes.

There are 29 buildings that satisfy the selection criteria (see Appendix B). A total of 172 sets of records from various earthquakes are available from the database. The buildings encompass a range of different story heights, lateral force resisting systems, site geologies, and ages (design years). Figures 5.11-5.12 show the spatial distribution of the selected building/earthquake pairs in Los Angeles and San Francisco.

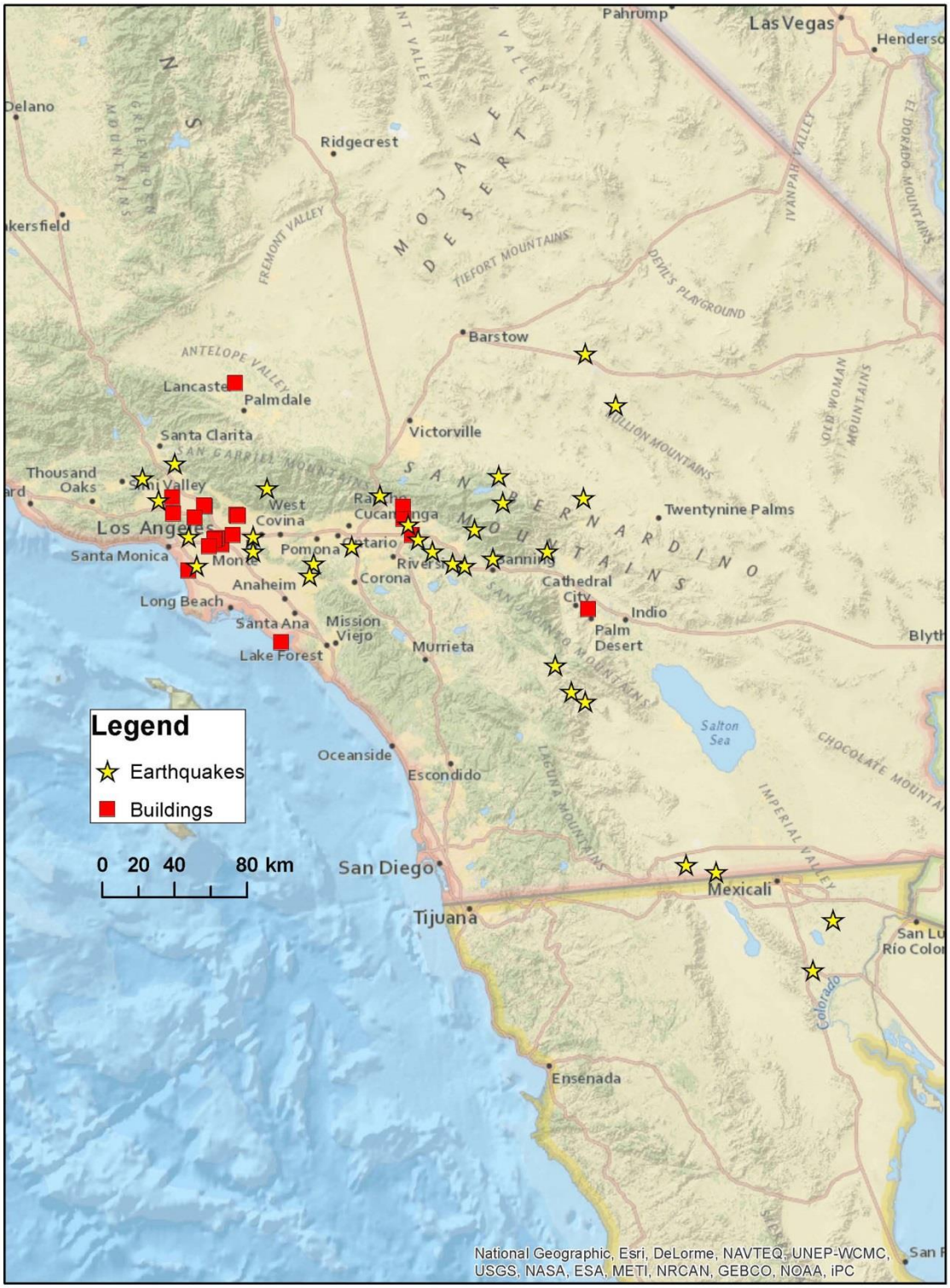

Figure 5.11: Spatial distribution of building/earthquake pairs in Los Angeles.

Figure 5.12: Spatial distribution of building/earthquake pairs in San Francisco.

5.2.7 DISCUSSION

The performance of the proposed decision-making methodology is examined for human comfort and elevator control applications. The correct warning that should be issued is calculated from the response based on the measured seismic data. The issued warning is calculated by using the predicted response based on the selected structural and ground motion models. The two warnings are compared to address the prediction capability of the selected structural and ground motion models and the decision-making capability. A perfect EEW prediction is assumed in this study, i.e., earthquake magnitude and epicenter location are taken to be the true magnitude and epicenter location of an earthquake. The analysis is focused on evaluating the performance of the chosen ground motion, structural and decision models.

The decision criteria for both human comfort and elevator control involve calculating a PDF of *PFA*:

$$p\left(PFA|M,R_{JB}\right)=\int p(PFA|IM)\,p\left(IM|M,R_{JB}\right)\,dIM \tag{5.4}$$

where M and R_{JB} are the magnitude and Joyner-Boore distance given by EEW.

Based on the chosen GMPE model and structural model, *IM* is chosen to be ln(*PGA*). For a given EEW data, Boore and Atkinson (2008) give a Gaussian distribution for ln(*PGA*) as follows:

$$p\left(\ln(PGA)|M,R_{JB}\right)=N(\ln(PGA)|\mu_1,\sigma_1) \tag{5.5}$$

where $N(x|\mu,\sigma)$ denotes the Gaussian distribution of x with mean μ and standard deviation σ. Here, the mean μ_1 and the standard deviation σ_1 can depend on M and R_{JB}.

Based on the structural model results given by Taghavi (2006), the conditional probability distribution of ln(*PFA*) given ln(*PGA*) is described as follows:

$$p(\ln(PFA)|\ln(PGA),\theta) = N(\ln(PFA)|\ln(PGA)+\mu_2,\sigma_2)$$

$$= \frac{1}{\sigma_2\sqrt{2\pi}}\exp\left(-\frac{(\ln(PFA)-\ln(PGA)-\mu_2)^2}{2\sigma_2^2}\right) \quad (5.6)$$

where the mean μ_2 and the standard deviation σ_2 of ln(*PFA*), given ln(*PGA*), depend on the structural model parameters θ which include the fundamental period of the building T_1 and lateral stiffness ratio α_0. In this example, fundamental periods are extracted from spectral peak-picking using small magnitude earthquake records and lateral stiffness ratios are selected based on the structural types of the buildings (see Appendix B).

Hence, $p(\ln(PFA)|\,\theta, M, R_{JB})$ can be computed from Equation 5.4 using Equations 5.5 and 5.6:

$$p\left(\ln(PFA)\,|\theta,M,R_{JB}\right) = \int p(\ln(PFA)\,|\ln(PGA))\,p\left(\ln(PGA)|M,R_{JB}\right)\,d(\ln(PGA))$$

$$= \int N(\ln(PFA)|\ln(PGA)+\mu_2,\sigma_2)\,N(\ln(PGA)\,|\mu_1,\sigma_1)\,d(\ln(PGA))$$

$$= N\left(\ln(PFA)\,|\mu_1+\mu_2,\sqrt{\sigma_1^2+\sigma_2^2}\right) \quad (5.7)$$

The above result is based on a well-known mathematical result for Gaussian integrals:

$$\int N(x|y+\mu_a,\sigma_a)\,N(y|\mu_b,\sigma_b)\,dy = N\left(x\middle|\mu_a+\mu_b,\sqrt{\sigma_a^2+\sigma_b^2}\right) \quad (5.8)$$

Hence, the resulting PDF of ln(*PFA*) given EEW data is Gaussian with its mean and standard deviation depending on those of the structural model and GMPE model.

For the human comfort application, the warning messages follow the categorization in Table 5.3. The correct warning on each floor of a building is taken to be the warning message based on the peak floor acceleration measured during an earthquake. The issued warning is based on the two decision criteria mentioned in Section 5.6. Comparison between the two criteria is discussed in the subsequent section.

For the elevator control application here, both US and Japan standards are considered. The elevator stopping criterion is chosen to be based on the threshold value P_0 on the probability of predicted *PFA* exceeding a standard threshold PFA_0:

$$Stop\ elevator\ \ iff\ \ P\left(\ln(PFA) > \ln(PFA_0)\,|\theta, M, R_{JB}\right) > P_0 \tag{5.9}$$

where

$$P\left(\ln(PFA) > \ln(PFA_0)\,|\theta, M, R_{JB}\right)$$

$$= \int_{\ln(PFA_0)}^{\infty} N\left(\ln(PFA)\,|\mu_1 + \mu_2, \sqrt{\sigma_1^2 + \sigma_2^2}\right) d(\ln(PFA))$$

$$= 1 - \Phi\left(\frac{\ln(PFA_0) - (\mu_1 + \mu_2)}{\sqrt{\sigma_1^2 + \sigma_2^2}}\right) \tag{5.10}$$

where $\Phi(x)$ is the CDF for N(0,1) variable.

5.2.7.1 HUMAN COMFORT

For the human comfort application, the warning messages categorized in Table 5.3 are: “no shaking”, “minor shaking”, “moderate shaking”, and “strong shaking”. There are a total of 16

different combinations based on 4 types of issued warnings and 4 types of correct warnings. Up to 647 cases are considered in the analysis (various records from different floors in the same building are considered as different cases). The fraction of cases where the issued warning is an under-estimate, correct or over-estimate based on the counting of the 16 combinations are presented in Table 5.4 shows the results for the two decision criteria. The two methods are described in Section 5.6.

Table 5.4. Results of human comfort application.

Decision Criterion	Under-estimate	Correct	Over-estimate
Mean-value method	0.329	0.507	0.164
Most-probable method	0.326	0.509	0.165

From Table 5.4, the two decision criteria provide similar performance. However, it is important to note that decision based on the most probable comfort level calculated from $p(PFA)$ is biased towards the largest interval when the intervals are not uniformly spaced (which is the case in this example). It is suggested that the traditional mean-value-based decision is more appropriate and easy to implement for practical use. Another observation is that the fraction of cases giving an under-estimate is higher than an over-estimate. It may be due to the fact that some local site effects, e.g., Los Angeles basin effect, are not captured in the simple GMPE model (Boore and Atkinson, 2008) for ground motion prediction. Also, *PGA* may not be a good metric to estimate seismic responses of tall buildings as discussed in Section 5.7.2.

5.2.7.2 ELEVATOR CONTROL

The threshold acceleration value for stopping an elevator is 0.5g for US buildings, and it is 0.08g to 0.15g for Japanese buildings. Table 5.5 shows the number of records exceeding the

threshold value in each case. Since the US standard is less stringent, only 8 out of 172 records exceed the given threshold. For the two boundary cases regarding the Japanese standard, at least one-third of the records exceed the threshold value. A common decision analyzing tool, the receiver operating characteristic (ROC) curve, is employed to analyze the decision-making methodology in this example. The ROC describes the true positive rate versus the false positive rate. In this example, the true positive rate is the fraction of cases making a correct decision to stop the elevator among all cases where the elevator should have been stopped (inversely related to missed alarm), while false positive rate is the fraction of cases making an incorrect decision to stop the elevator among all cases where it should not (related to false alarm). Figure 5.13 shows the ROC curve for 3 threshold values based on the US and Japan standard. The point at the top left corner of the ROC space indicates the best possible prediction method, because it represents a 100% true positive rate and 0% false positive rate. Any curve which is close to the top left corner represents a good decision policy. In contrast, the diagonal dash line indicates what we call a random guess decision policy. Any curve which is close to the diagonal line represents a bad decision policy.

Table 5.5. Threshold value comparison using the measured records (real case).

Threshold	No. of records exceeding threshold	No. of records below threshold
PFA_0 = 0.08g	82	90
PFA_0 = 0.15g	57	115
PFA_0 = 0.5g	8	164

In Figure 5.13, each ROC curve is parameterized by P_0 from 0 (top right) to 1 (bottom left). The ROC curve by US standard (PFA_0 = 0.5g) is the closest to the top left corner. However, there are too few records exceeding the given threshold in the real case (see Table 5.5), so the result given by this case is not statistically significant. The two ROC curves by Japan standard (PFA_0 =

0.08g and 0.15g) are also considerably close to the top left corner. This result indicates that the performance of the proposed decision criterion is satisfactory. A point to note is that users can pick any point P_0 on the ROC curve as their own decision criterion, and it all depends on their utility function. Depending on the situation, a user may favor a point with high true positive rate and corresponding high false positive rate, or a point with low false positive rate and corresponding low true positive rate.

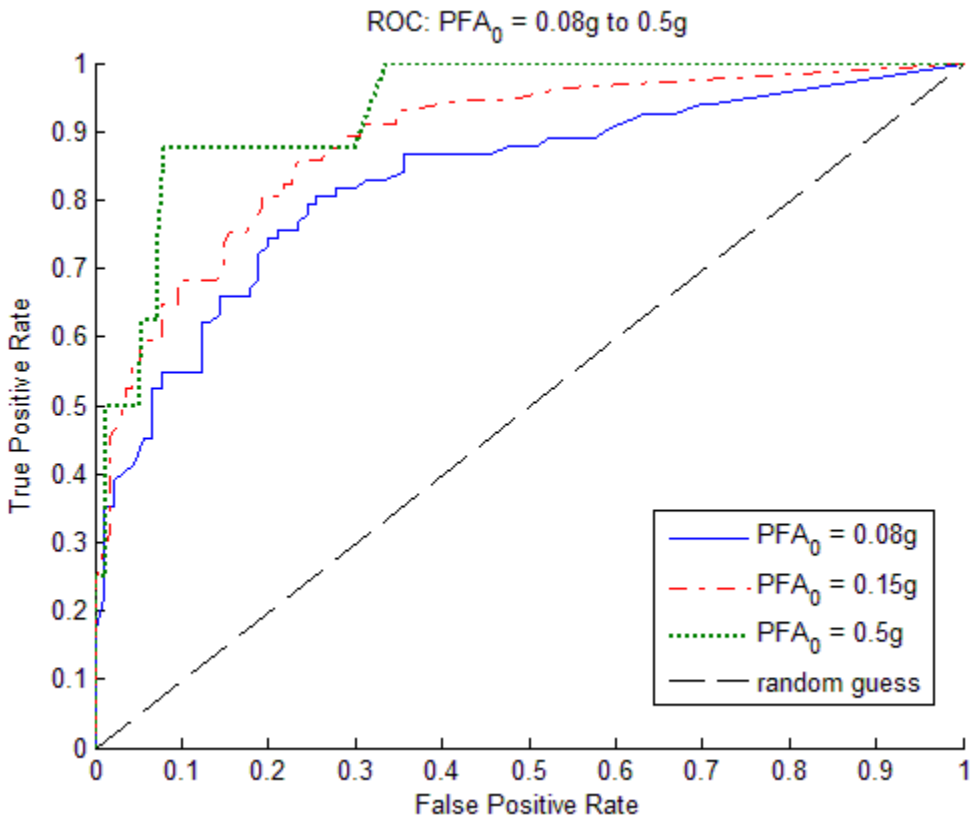

Figure 5.13: ROC plot for elevator control. Blue solid curve shows the results for PFA_0 = 0.08g. Red dash curve shows the results for PFA_0 = 0.15g. Green dotted curve shows the results for PFA_0 = 0.5g. Each curve is parameterized by P_0 from 0 to 1. Black diagonal dash line indicates the random guess decision policy.

Limitations due to the choice of simple models are also investigated. With the illustration using the Japan standard, Figure 5.14 shows the improvement in the ROC curve for PFA_0 = 0.08g after removing the records for buildings with non-uniform vertical stiffness. After such removal, the ROC curve shifts to the top left corner. This is mainly due to the fact that the structural model (Miranda and Taghavi, 2005) used in this study cannot effectively perform *PFA* estimation in non-uniform buildings. Similar results are obtained for the PFA_0 = 0.15g case.

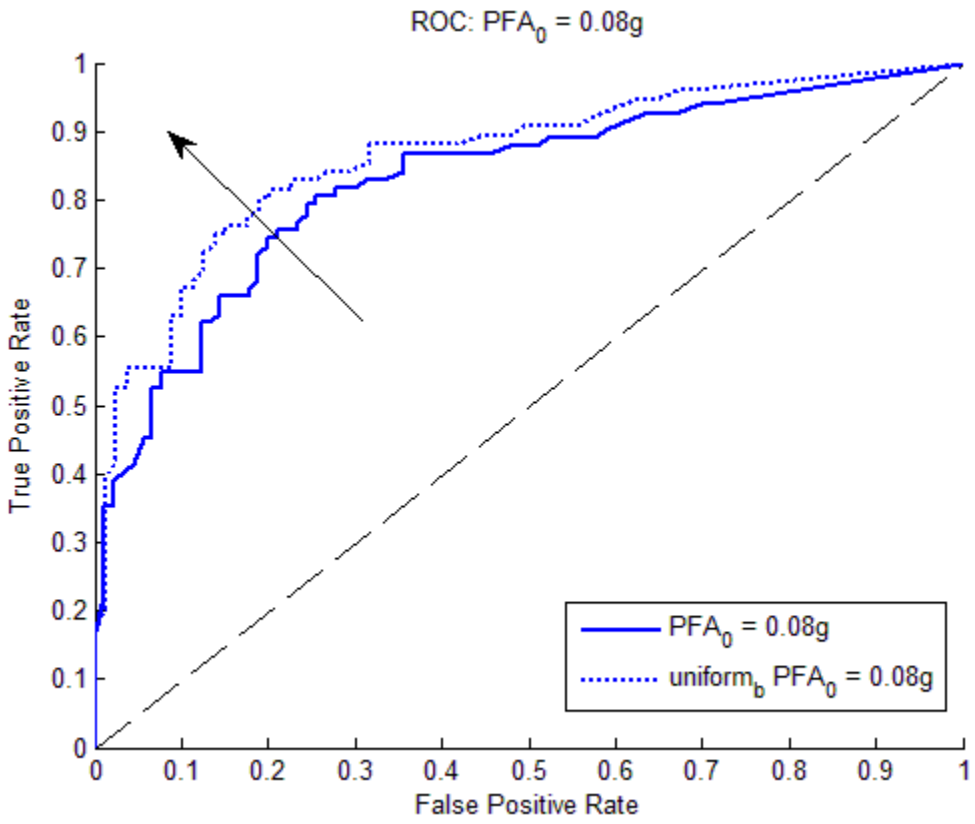

Figure 5.14: ROC plot for elevator control for PFA_0 = 0.08g. Solid lines are the results using all the 172 records. Dotted lines are the results using the records only from buildings with uniform vertical stiffness.

5.3 VALUE OF INFORMATION MODEL

In the previous sections, a probabilistic framework for automated elevator control based on the expected shaking intensity in buildings is presented. The possible action could be stopping the elevator at the nearest floor and opening the elevator door for people to evacuate. Here, the required action time and the lead time in earthquake early warning will be considered in the framework. When the lead time is less than the action time, the system would take action only if the incomplete action is still beneficial. Otherwise, the system is expected to trigger a back-up action, e.g., an immediate stop of the elevator. This section presents the collaborative work with Stephen Wu, in which I contributed on the numerical computations using Monte Carlo simulations (MCS) and machine learning (Relevance Vector Machine, RVM). In this study, RVM is selected to construct a surrogate model for efficient computation mainly because of its ability to obtain sparse solutions in regression using a Bayesian learning framework (Tipping, 2001).

Wu et al. (2013) outlined an earthquake probability-based automated decision making (ePAD) framework, which aims to choose an optimal action based on cost-benefit analysis. A value of information model is proposed to account for the lead time in earthquake early warning. Decision is made according to the tradeoff between the extra reduction (benefit), L_B, and the cost, L_C, of economic loss after taking the action, given the seismic data $D(t)$ at time t. Consider a simple case where a_1 = take action and a_0 = no action. If no action is taken, we define $E[DF|D(t), a_0] = VoI$.

$$VoI = \int \int_{\Delta t}^{\infty} max\{DF(IM, T_{lead} - \Delta t, a_1), 0\} p\big(IM \big| D(t)\big) p\big(T_{lead} \big| D(t)\big)\, dIM\, dT_{lead} \quad (5.11a)$$

$$DF(IM, T_{lead}, a_i) = \beta_i(T_{lead}) E[L_B|IM, A_i] - \gamma_i(T_{lead}) E[L_C|IM, A_i] \quad (5.11b)$$

where DF is the decision function which combines all the user-specific models (e.g. decision model, structural model and ground motion model); IM is the intensity measure (= ln PGA, in this example); T_{lead} is the lead time; Δt is the expected time interval for the next EEW update; a_i donates initiating the i^{th} action and a_0 donates temporarily not taking any action; A_i donates completion of the i^{th} action and A_0 donates permanently not taking any action; β and γ are discounting factors as a function of T_{lead}. If no action is taken, there is no benefit or cost associated with this decision. The expected value of L_B and L_C given IM and a_0, $E[L_B|IM,a_0]$ and $E[L_C|IM,a_0]$, are both zero. Hence, $E[DF|D(t),a_0] = 0$. On the other hand, $E[L_B|IM,a_1]$ and $E[L_C|IM,a_1]$ are calculated based on a loss model and a structural model. We assume $E[L_B|IM,a_1] = r_B l_B P(DM|IM,a_1)$ and $E[L_C|IM,a_1] = r_C l_C$, where l_B is the number of injured individuals; l_C is the associated cost, including time delay and service interruption; $P(DM|IM,a_1)$ is the fragility function of damage state DM; r_B and r_C are the factors used to convert benefit and loss terms to economic values.

Let T_a be time required to complete an action. As an example, we assume that β_1 is a step function with value of 0 when $T_{lead} < T_a$ and 1 otherwise. No benefit is gained if the required action cannot be completed; γ_1 is a linear function with values between r_0 and 1 when $T_{lead} < T_a$, where r_0 represents the ratio of fixed cost (independent of T_{lead}) over total cost. Figure 5.15 shows the value of β_1 and γ_1 as a function of T_{lead}. The functions β_0 and γ_0 are not considered here because $DF(IM,T_{lead},a_0) = 0$. More details can be found in Wu (2014).

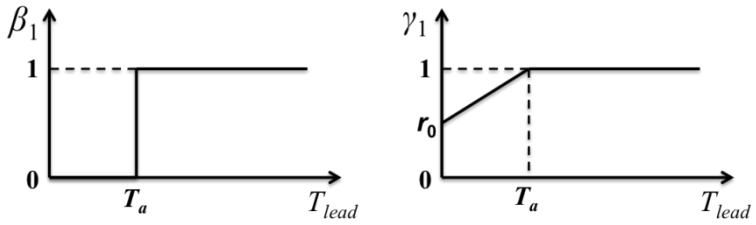

Figure 5.15. β_1 and γ_1 as a function of T_{lead}.

Now, we consider the following decision criteria:

Take action if and only if $E[DF|D(t), a_1] = E[L_B|D(t), a_1] - E[L_C|D(t), a_1] > VoI$ (5.12)

Consider the same structural model as discussed in Section 5.2.5 and divide Equation 5.12 by $r_B l_B$, we get:

Take action if and only if $\Phi\left(\frac{\mu_{ST}+\mu_{IM}-lnpfa_0}{\sqrt{\sigma_{ST}^2+\sigma_{IM}^2}}\right) > r_T P_0 + r_{VoI} I_{VoI}$ (5.13)

where $r_{VoI}(\mu_T, \sigma_T) = \Phi\left(\frac{\ln(\mu_T)-\ln(T_a+\Delta t)}{\sigma_T}\right) / \Phi\left(\frac{\ln(\mu_T)-\ln(T_a)}{\sigma_T}\right)$ (5.14a)

$$I_{VoI}(\mu_{IM}, \sigma_{IM}) = \int max\{0, P(DM|IM, A_1) - P_0\} \Phi\left(\frac{IM-\mu_{IM}}{\sigma_{IM}}\right) dIM \quad (5.14b)$$

$$P_0 = \frac{r_C l_C}{r_B l_B} \quad (5.15c)$$

where r_T is a function of lead time (μ_T, σ_T) and action time (T_a). Derivations can be referred to Wu (2014). Here, we consider a surrogate model with parameters $lnpfa_0$ = ln(0.5g), α_0 = 3.125, T_1 = 2.5sec, and P_0 = 0.3. This set of parameters represents a 20- to 30-story tall building with dual structural system (μ_{ST} = 0.82, σ_{ST} = 0.22) and a relatively conservative elevator control decision

behavior under the current US standard. The training data for the surrogate model is obtained from Monte Carlo Simulation (MCS) of the actual integral I_{VoI}. Figure 5.16 shows that I_{VoI} values computed using the surrogate model from RVM (colored mesh) matches well with the values obtained from MCS (points with blue cross symbol). The maximum absolute error at any data point is less than 5%.

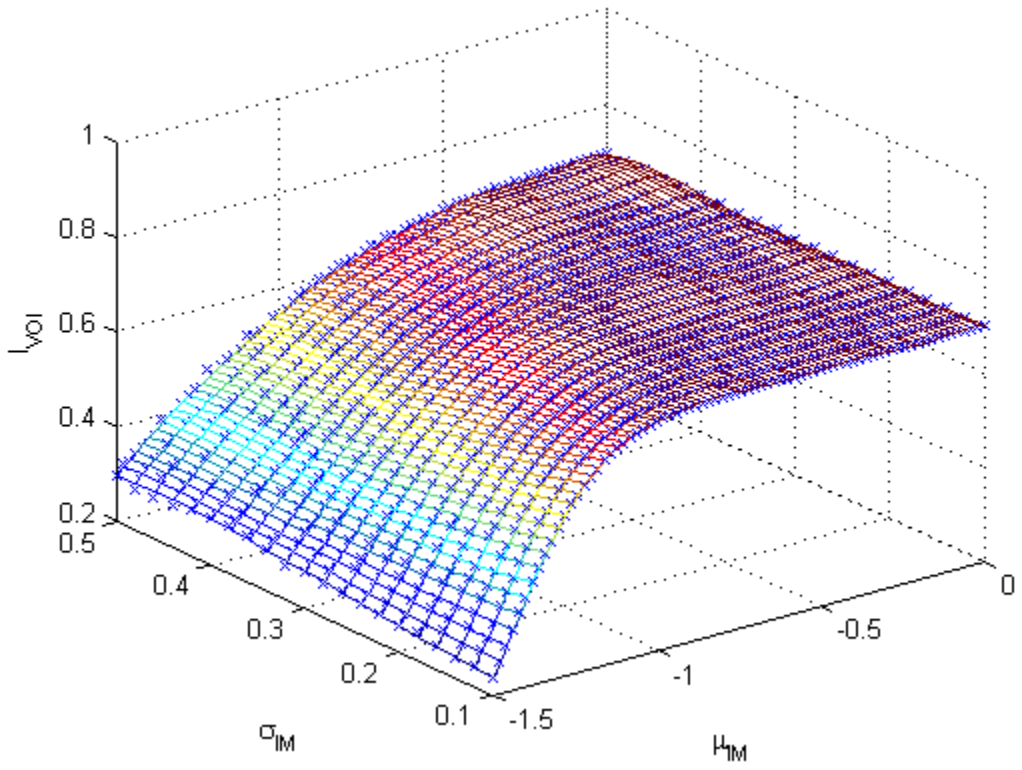

Figure 5.16. Surrogate model of I_{VOI} using RVM. (colored mesh: RVM; points with cross symbol: MCS).

Here, we consider the lead time model with parameters T_a = 2sec, r_0 = 0.5, Δt = 1s, σ_T = 0.2sec and μ_T ranges from 1sec to 4sec. Figure 5.17 shows that decision contours obtained from the surrogate model match well with the actual decisions obtained from MCS. An action will be

triggered if the computed value falls above the corresponding decision contour. Decision contours become more "uncertainty-taking" as μ_T increases, which is due to the expected benefit of potentially less uncertain information in later time. As a side note, no decision contour is shown for μ_T < 2sec. In such case, action is not taken due to the lack of benefit from an incomplete action. As mentioned before, a back-up action, e.g., immediate stop of the elevator, would be triggered. For example, if we consider the case of μ_{IM} = -1.5 and σ_{IM} = 0.05, the required action will only be taken if μ_T > 2sec, and the back-up action will be taken if $\mu_T \leq$ 2sec.

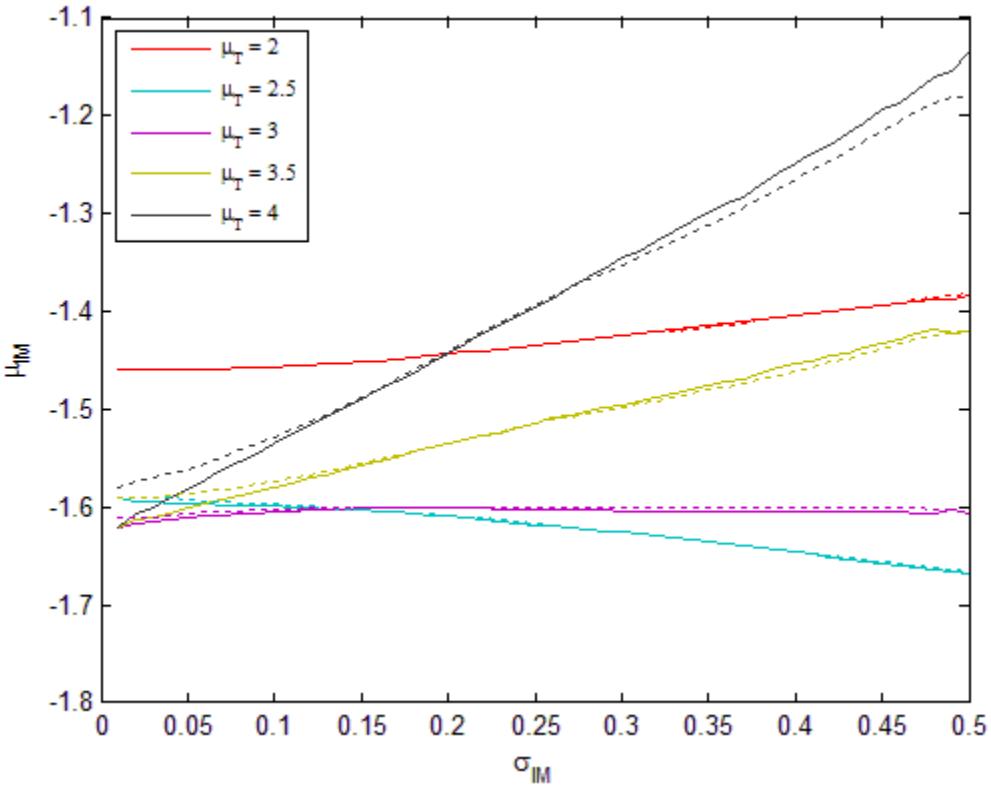

Figure 5.17. Decision contours for value of information model (solid lines: from MCS; dotted lines: from RVM).

Chapter 6

FUTURE WORK

CSN network and earthquake early warning:

Much work can be done to investigate the seismic energy concentration in 4-10Hz from the recorded data in the CSN network. The use of Geocells (Olson, 2014) can enhance the confidence in event detection using the low-quality data from low-cost sensors. Possible future studies include the effect of a band-pass filter for real-time earthquake early warning using Geocells.

The probabilistic decision-making framework can be adopted to develop other earthquake early warning applications, e.g. traffic control in transportation networks and automated stiffness change of smart buildings.

Timoshenko beam with soil springs:

Much work can be done to study the reliability of mode shape prediction from natural frequency ratio for various types of buildings. The effects of non-uniform vertical stiffness and mass along the building height are other essential topics for investigation. The Timoshenko beam model can possibly be extended to include torsional effect for 3D response simulation.

Wave propagation in buildings:

Future work can be done to understand the occurrence of initial traveling seismic impulses in buildings for various ground motions and building types.

Chapter 7

SUMMARY

Community Seismic Network, one of the newly developed seismic networks which utilize the use of low-cost seismic sensors, provides another source to monitor earthquakes. The network can be extended to perform structural health monitoring of buildings as well as to facilitate the development of engineering applications for earthquake early warning systems. Chapter 2 presents an overview of such a network as well as its application to earthquake detection. Statistical tests show that the spectral energy in the recorded data during earthquakes concentrates in 4-10Hz, and a suitable band-pass filter can improve the existing earthquake detection algorithm.

Chapter 3 presents a closed form solution for the prismatic Timoshenko beam model with soil-structure interaction. In general, buildings behave like a Timoshenko beam with properties in between a pure shear beam and a pure bending beam, and soil-structure interaction should not be neglected in determining dynamic behaviors of buildings during earthquakes. A formal methodology is presented that predicts mode shapes of a building assuming that (1) we have records from at least one seismometer in the building from which we can determine the first two modal frequencies in a given direction, (2) we can estimate the exterior dimensions of the building, and (3) the building can be approximately modeled as a Timoshenko beam on a translational and rotational base. The proposed method is successfully applied to estimate the mode shapes of Millikan Library at Caltech.

Chapter 4 presents a simple method to estimate the linear elastic response of a building using data from a single seismometer. Total displacement response of buildings due to earthquake-excited vibrations is decomposed into the traveling wave component and the resonant mode component.

Resonant mode response in displacement can be obtained with appropriate band-pass filter. Seismic records from a 54-story building in downtown Los Angeles and a finite-element model for UCLA Factor building have been used to illustrate the proposed method. If only one seismometer is allowed in a building, this study suggests that the instrument shall be installed on a floor away from the nodal points of the dominant vibrating modes. The proposed method can beneficially utilize the data from the crowd-sourced seismic networks, where station locations are typically chosen for reasons that are unrelated to, and that may not be able to take advantage of, the optimal design of a seismic network. It allows users to visualize the vibrating motions of buildings due to small-to-moderate earthquakes. It could also provide a rapid interpretation of shaking intensity that is useful for emergency response and earthquake early warning applications.

Chapter 5 presents a building warning method that focuses on human comfort prediction and automated elevator control. It is based on the Performance-based Earthquake Early Warning (PBEEW) framework. Examples using an existing Ground Motion Prediction Equation (GMPE) and a simple structural model combining the behavior of flexural and shear cantilever beams are included to illustrate the use of the proposed PBEEW framework for buildings. The prediction results are acceptable, but they also suggest that the simplified ground motion and structural models do not capture some local site effects, e.g., Los Angeles basin effect, and some building behaviors, e.g., response of non-uniform buildings. This chapter discusses that a user could select a P_0 value that represents the user's decision behavior, without performing the complete cost-benefit analysis. Decision contours can be used to study the effects of lead time and uncertainties in earthquake early warning information, and a surrogate model using Relevance Vector Machine (RVM) can be adopted to efficiently compute decision contours in the value of information model.

BIBLIOGRAPHY

Abrahamson, N. and W. Silva, 2008. Summary of the Abrahamson & Silva NGA ground motion relations, *Earthquake Spectra* **24** (1), 67-97.

Allen, R. M., P. Gasparini, O. Kamigaichi, and M. Böse, 2009a. The status of earthquake early warning around the world: an introductory overview, *Seismological Research Letters* **80** (5), 682-693.

Allen, R. M., H. M. Brown, M. Hellweg, O. Khainovski, P. Lombard, and D. Neuhauser, 2009b. Real-time earthquake detection and hazard assessment by ElarmS across California, *Geophysical Research Letters* **36**, L00B08.

Alvin, K. F., A. N. Robertson, G. W. Reich, and K. C. Park, 2003. Structural system identification: from reality to models, *Computers and Structures* **81**, 1149-1176.

Bashor R., T. Kijewski-Correa, A. Kareem, 2005. On the wind-induced response of tall buildings: The effect of uncertainties in dynamic properties and human comfort thresholds, *Proceedings of Tenth Americas Conference on Wind Engineering*, Baton Rouge, USA.

Balendra, T., W. T. Chan, and S. L. Lee, 1982. Modal damping for torsionally coupled buildings on elastic foundation, *Earthquake Engineering and Structural Dynamics* **10**, 735-756.

Bradford, S. C., 2006. Time-frequency analysis of systems with changing dynamic properties, *PhD dissertation*, California Institute of Technology, Pasadena, California, USA.

Boggs D., 1997. Acceleration indexes for human comfort in tall buildings – Peak or RMS? In: Isyumov N, Goto T, Tschanz T, editors. *Motion Perception Tolerance and Mitigation. Counsel on Tall Buildings and Urban Habitat*, CTBUH Monograph Chpt. 13.

Boore, D. M. and G. M. Atkinson, 2008. Ground-motion prediction equations for the average horizontal component of PGA, PGV, and 5%-damped PSA at spectral periods between 0.01s and 10.0s, *Earthquake Spectra* **24** (1), 99-138.

Boutin, C., S. Hans, E. Ibraim, and P. Roussillon, 2005. In situ experiments and seismic analysis of existing buildings. Part II: Seismic integrity threshold, *Earthquake Engineering and Structural Dynamics* **34** (12), 1531-1546.

Böse, M., E. Hauksson, K. Solanki, H. Kanamori, and T. H. Heaton, 2009a. Real-time testing of the on-site warning algorithm in Southern California and its performance during the July 29 2008 Mw5.4 Chino Hills earthquake, *Geophysical Research Letters* **36**, L00B03.

Böse, M., E. Hauksson, K. Solanki, H. Kanamori, Y. M. Wu, and T. H. Heaton, 2009b. A new trigger criterion for improved real-time performance of onsite earthquake early warning in Southern California, *Bulletin of the Seismological Society of America* **99** (2A), 897-905.

Böse, M., R. Allen, H. Brown, G. Cua, E. Hauksson, T. H. Heaton, et al., 2013. CISN ShakeAlert - An Earthquake Early Warning Demonstration System For California, *Early Warning For Geological Disasters - Scientific Concepts And Current Practice*, Springer, Eds. F. Wenzel and J. Zschau, in press.

Bycroft, R. N., 1956. Forced vibrations of a rigid circular plate on a semi-infinite elastic space and on an elastic stratum, *Philosophical Transactions of the Royal Society of London. Series A, Mathematical and Physical Sciences* **248** (948), 327-368.

Campbell, K. W. and Y. Bozorgnia, 2008. NGA ground motion model for the geometric mean horizontal component of PGA, PGV, PGD and 5% damped linear elastic response spectra for periods ranging from 0.01 to 10s, *Earthquake Spectra* **24** (1), 139-171.

Campillo, M. and A. Paul, 2003. Long-range correlations in the diffuse seismic coda, *Science* **299**, 547-549.

Cheng, M. H. and T. H. Heaton, 2013. Simulating building motions using the ratios of its natural frequencies and a Timoshenko beam model, *Earthquake Spectra*, in press, DOI: http://dx.doi.org/10.1193/011613EQS003M.

Cheng, M. H., S. Wu, T. H. Heaton, and J. L. Beck, 2014. Earthquake early warning application to buildings, Engineering Structures **60**, 155-164.

Chiou, BS-J. and R. R. Youngs, 2008. An NGA model for the average horizontal component of peak ground motion and response spectra, *Earthquake Spectra* **24** (1), 173-215.

Chopra, A. K., 2007. Dynamics of structures: Theory and applications to earthquake engineering, 3rd edition. *Pearson Prentice Hall*, Upper Saddle River, NJ.

Clayton, R., T. Heaton, M. Chandy, A. Krause, M. Kohler, J. Bunn, M. Olson, M. Faulkner, M. H. Cheng, L. Strand, R. Chandy, D. Obenshain, A. Liu, and M. Aivazis, 2011. Community Seismic Network, *Annals of Geophysics* **54** (6), 738-747.

Clinton, F. J., S. C. Bradford, T. H. Heaton, and J. Favela, 2006. The observed wander of the natural frequencies in a structure, *Bulletin of the seismological society of America* **96** (1), 237-257.

Cochran, E. S., J. F. Lawrence, C. Christensen, and R. S. Jakka, 2009. The Quake-Catcher Network: citizen science expanding seismic horizons, Seismological Research Letters **80** (1), 26-30.

Cochran, E. S., J. F. Lawrence, A. Kaiser, B. Fry, A. Chung, and C. Christensen, 2011. Comparison between low-cost and traditional MEMS accelerometers: a case study from the M7.1 Darfield, New Zealand, aftershock deployment, *Annals of Geophysics* **54** (6), 728-737.

Crowley, H., R. Pinho, and J. J. Bommer, 2004. A probabilistic displacement-based vulnerability assessment procedure for earthquake loss estimation, *Bulletin of Earthquake Engineering* **2**, 173-219.

Cua, G. B., 2005. Creating the Virtual Seismologist: developments in ground motion characterization and seismic early warning, *PhD dissertation*, California Institute of Technology, Pasadena, California, USA.

Cua, G. and T. H. Heaton, 2007. The Virtual Seismologist (VS) method: a Bayesian approach to earthquake early warning, In: Gasparini P, Manfredi G, Zschau J, editors, *Earthquake Early Warning Systems,* Springer Berlin Heidelberg, 97-132.

Denolle, M. A., Dunham, E. M., Prieto, G. A., and Beroza, G. C., 2013. Ground motion prediction of realistic earthquake sources using the ambient seismic field, *J. Geophys. Res. Solid Earth* **118**, 1-17.

Division of Occupational Safety and Health (Cal/OSHA). Title 8 regulations. Sub-Chapter 6, Elevator Safety Orders. Group 3, New Elevator Installations. Article 37, Seismic Requirements For Elevators, Escalators and Moving Walks. Section 3137. (http://www.dir.ca.gov/Title8/3137.html, accessed on 17 Dec, 2012).

Doi K., 2002. Earthquake early warning system in Japan, In: Zschau J, editor, *Early Warning Systems for Natural Disaster Reduction*, Springer-Verlag Berlin, Berlin, Germany.

Ebrahimian, M. and M. Todorovska, 2013. Wave propagation in a Timoshenko beam building model, *J. Eng. Mech.*, in press, DOI: 10.1061/(ASCE)EM. 1943-7889.0000720.

Faulkner, M., R. Clayton, T. Heaton, K. M. Chandy, M. Kohler, J. Bunn, R. Guy, A. Liu, M. Olson, M. H.. Cheng, and A. Krause, 2013. Community sense and response systems: your phone as quake detector, *CACM*, in press.

Favela, J., 2004. Energy radiation from a multi-story building, *PhD dissertation*, California Institute of Technology, Pasadena, California.

Foutch, D. A. and P. C. Jennings, 1978. A study of the apparent change in the foundation response of a nine-story reinforced concrete building, *Bulletin of the Seismological Society of America* **68** (1), 219-229.

Grasso, V. F., 2005. Seismic Early Warning Systems: Procedure for Automated Decision Making, *PhD thesis*, Università degli Studi di Napoli Federico II, Naples, Italy.

Grasso, V. F., J. L. Beck, and G. Manfredi, 2007. Automated decision procedure for earthquake early warning, *Engineering Structures* **29** (12), 3455-3463.

Graves, R., T. H. Jordan, S. Callaghan, E. Deelman, E. Field, G. Juve, et al., 2011. CyberShake: A physics-based seismic hazard model for Southern California, *Pure & Applied Geophysics* **168** (3-4), 367-381.

Griffis, L. G., 1993. Serviceability limit states under wind load, *AISC Engineering Journal* **30** (1), 1–16.

Hall, J. F., 1997. Seismic response of steel frame buildings to near-source ground motions, *California Institute of Technology*, EERL-97-05.

He, X. and J. Tromp, 1996. Normal-mode constraints on the structure of the Earth, *Journal of Geophysical Research* **101** (B9), 20053-20082.

Heidebrecht, A. C. and B. S. Smith, 1973. Approximate analysis of tall wall-frame structures, *Journal of the Structural Division, Proceedings of the ASCE* **99** (2), 199-221.

Hilbring, D., T. Titzschkau, A. Buchmann, G. Bonn, F. Wenzel, and E. Hohnecker, 2010. Earthquake early warning for transport lines, *Natural Hazards*, 1-31.

Hsu, J. C., H. L. Lee, and W. J. Chang, 2007. Flexural vibration frequency of atomic force microscope cantilevers using the Timoshenko beam model, *Nanotechnology* **18**, 28.

Idriss, I. M., 2008. An NGA empirical model for estimating the horizontal spectral values generated by shallow crustal earthquakes, *Earthquake Spectra* **24** (1), 217-242.

Iervolino, I., M. Giorgio, and G. Manfredi, 2007. Expected loss-based alarm threshold set for earthquake early warning systems, *Earthquake Engineering and Structural Dynamics*, **36** (9), 1151-1168.

International Handbook of Earthquake & Engineering Seismology, Part 2, 2003. Chapter 67, Editors: Lee, H. K., H. Kanamori, P. Jennings, and C. Kisslinger, *Academic Press*, Burlington, MA, USA.

Iwan, W., 1997. Drift spectrum: measure of demand for earthquake ground motion, *Journal of Structural Engineerin*g **123** (4), 397-404.

Jennings, R. L. and N. M. Newmark, 1960. Elastic response of multi-story shear beam type structures subjected to strong ground motion, *Proceedings of the Second World Conference on Earthquake Engineering*, Vol. 2, Science Council of Japan, Tokyo, Japan.

Jennings, P. C., 2003. An introduction to the earthquake response of structures, in *International Handbook of Earthquake and Engineering Seismology,* W. H. K. Lee, H. Kanamori, P. C. Jennings, and C. Kisslinger (Editors), Academic Press, Burlington, MA, USA, Volume 81, Part B, 1097-1125.

Kasai, L., W. C. Pu, and A. Wada, 2012. Responses of tall buildings in Tokyo during the 2011 Great East Japan Earthquake, *Proceedings of Behavior of Steel Structures in Seismic Area (STESSA),* Santiago, Chile.

Kohler, M. D., P. M. Davis, and E. Safak, 2005. Earthquake and ambient vibration monitoring of the steel frame UCLA Factor building, *Earthquake Spectra* **21** (3), 715-736.

Kohler, M., T. Heaton, R. Govindan, P. Davis, and D. Estrin, 2006. Using embedded wired and wireless seismic networks in the moment-resisting steel frame Factor building for damage identification, *Proceedings of the 4th China-Japan-US Symposium on Structural Control and Monitoring*, Hangzhou, China.

Kohler, M. D., T. H. Heaton, and S. C. Bradford, 2007. Propagating waves in the steel, moment-frame Factor building recorded during earthquakes, *Bulletin of the Seismological Society of American* **97** (4), 1334-1345.

Kohler, M. D., T. H. Heaton, and M. H. Cheng, 2013. The community seismic network and quake-catcher network: enabling structural health monitoring through instrumentation by community participants, *Proceedings of SPIE 8692*, San Diego, USA.

Kohler, M. D., T. H. Heaton, M. H. Cheng, and P. Singh, 2014. Structural health monitoring through dense instrumentation by community participants: the community seismic network, *Proceedings of the 10th US National Conference on Earthquake Engineering*, Alaska, USA.

Krishnan, S. and M. Muto, 2013. Sensitivity of the earthquake response of tall steel moment frame buildings to ground motion features, *Journal of Earthquake Engineering* **17** (5), 673-698.

Kubo, T., Y. Hisada, M. Murakami, F. Kosuge, and K. Hamano, 2011. Application of an earthquake early warning system and a real-time strong motion monitoring system in emergency response in a high-rise building, *Soil Dynamics and Earthquake Engineering* **31**, 231-239.

Lee, J. Y. and S. Y. Ahn, 2011. Finite element implementation for computer-aided education of structural mechanics: Frame analysis, *Comput. Appl. Eng. Educ*.

Ljing, L., 1999. System identification: theory for the user, Second edition, *Prentice Hall*, Upper Saddle River, NJ, USA.

Malhotra, P. K., 2006. Smooth spectra of horizontal and vertical ground motions, *Bulletin of the Seismological Society of America* **96** (2), 506-518.

Medina, R. and H. Krawinkler, 2005. Evaluation of drift demands for the seismic performance assessment of frames, *Journal of Structural Engineering* **131**, 1003-1013.

Michel, C., S. Hans, P. Guéguen, and C. Boutin, 2006. In Situ Experiment and Modelling of RC-structure using ambient vibration and Timoshenko beam, *Proceedings of 1st European Conference on Earthquake Engineering and Seismology (ECEES)*, Geneva, Switzerland.

Miranda, E., 1999. Approximate seismic lateral deformation demands in multistory buildings, *Journal of Structural Engineering, ASCE* **125** (4), 417-425.

Miranda, E. and C. J. Reyes, 2002. Approximate lateral drift demands in multi-story buildings with nonuniform stiffness. *J. Struct. Eng.* **128** (7), 840-849.

Miranda, E. and S. Taghavi, 2005. Approximate floor acceleration demands in multistory buildings. I: Formulation, *Journal of Structural Engineering* **131** (2), 203-211.

Okawa, I., T. Kashima, and S. Koyama, 2001. Earthquake recording for SSI study by BRI, *Proceedings of the 2nd UJNR Workshop on Soil-Structure Interaction*, Tsukuba, Japan.

Overschee, P. V. and B. D. Moor, 1994. N4SID: subspace algorithms for the identification of combined deterministic-stochastic systems, *Automatica* **30** (1), 75-93.

Prieto, G. A., J. F. Lawrence, A. I. Chung, and M. D. Kohler, 2010. Impulse response of civil structures from ambient noise analysis, *Bulletin of the Seismological Society of America* **100** (5A), 2322-2328.

Rahgozar, R., H. Safari, and P. Kaviani, 2004. Free vibration of tall buildings using Timoshenko beams with variable cross-section, *Proceedings of SUSI VIII*, Crete, Greece.

Rahmani, M. and M. I. Todorovska, 2013. 1D system identification of buildings during earthquakes by seismic interferometry with waveform inversion of impulse responses-method and application to Millikan Library, *Soil Dynamics and Earthquake Engineering* **47**, 157-174.

Roberts, M. W. and L. D. Lutes, 2003. Potential for structural failure in the seismic near field, *Journal of Engineering Mechanics* **129** (8), 927-934.

Romanowicz, B. A., M. P. Panning, Y-C. Gung, and Y. Capdeville, 2008. On the computation of long period seismograms in a 3-D earth using normal mode based approximations, *Geophysical Journal International* **175**, 520-536.

Rosat, S., S. Watada, and T. Sato, 2007. Geographical variations of the 0S0 normal mode amplitude: predictions and observations after the Sumatra-Andaman earthquake, *Earth Planets Space* **59**, 307-311.

Sasani, M., N. Makris, and B. A. Bolt, 2006. Damping in shear beam structures and estimation of drift response, *Journal of Engineering Mechanics* **132** (8), 851-858.

Skolnik, D., L. Ying, E. Yu, and J. W. Wallace, 2006. Identification, model updating, and response prediction of an instrumented 15-story steel frame building, *Earthquake Spectra* **22** (3), 781-802.

Snieder, R. and E. Safak, 2006. Extracting the building response using seismic interferometry: Theory and application to the Millikan Library in Pasadena, California, *Bulletin of the Seismological Society of America* **96** (2), 586-598.

Stewart, J. P. and G. L. Fenves, 1998. System identification for evaluating soil-structure interaction effects in buildings from strong motion recordings, *Earthquake Engng. Struct. Dyn.* **27**, 869-885.

Sutoyo, D., 2009. Hysteretic characteristics of wood-frame structures under seismic motions, *PhD thesis*, California Institute of Technology, Pasadena, California, USA.

Taghavi, S., 2006. Probabilistic seismic assessment of floor acceleration demands in multi-story buildings, *PhD thesis*, Stanford University, Stanford, California, USA.

Timoshenko, S., 1937. Vibration problems in engineering, 2nd edition, *D. Van Nostrand Company, Inc.*, Princeton, NJ.

Timoshenko, S., and J. N. Goodier, 1951. Theory of elasticity, 2nd edition, *McGraw-Hill Book Company, Inc.*, New York, NY.

Tipping, M. E., 2001. Sparse Bayesian learning and the relevance vector machine, *Journal of Machine Learning Research* **1**, 211-244.

Todorovska, M. I., 2009. Seismic interferometry of a soil-structure interaction model with coupled horizontal and rocking response, *Bulletin of the Seismological Society of America* **99** (2A), 611-625.

Ulusoy, H. S., E. Kalkan, J. P. B. Fletcher, P. Friberg, W. K. Leith, and K. Banga, 2012. Design and implementation of a structural health monitoring and alerting system for hospital buildings in the United States, *Proceedings of the 15th World Conference on Earthquake Engineering*, Lisbon, Portugal.

Wang, C. M., Y. Y. Zhang, and X. Q. He, 2007. Vibration of nonlocal Timoshenko beams, *Nanotechnology* **18**, 10.

Westergaard, H. M., 1933. Earthquake-shock transmission in tall buildings, *Engineering News Record* **III**, 654-656.

Wu, S., J. L. Beck, and T. H. Heaton, 2013. ePAD: Earthquake probability-based automated decision-making framework for earthquake early warning, *Computer-Aided Civil and Infrastructure Engineering* **28**, 737-752.

Wu, S., 2014. *PhD thesis*, California Institute of Technology, Pasadena, California, USA.

A p p e n d i x A

DERIVATION OF TIMOSHENKO BEAM WITH SOIL-STRUCTURE INTERACTION

Define μ as the angle of shear at the neutral axis in the same cross-section, Φ as the rotation due to bending (when shear stress is neglected), w is the deflection of the beam with respect to z-axis, then

$$\frac{\partial \mathrm{w}}{\partial \mathrm{x}} = \Phi + \mu \tag{A.1}$$

The coordinates of the Timoshenko beam is defined as shown in Figure 3.2.

By strain-displacement relation:

$$\dot{o}_{xx} = z\frac{\partial \Phi}{\partial x} \text{ and } \gamma_{xz} = -\Phi + \frac{\partial \mathrm{w}}{\partial \mathrm{x}} \tag{A.2}$$

$$\text{Strain energy } U\text{: } = \frac{1}{2}\int_0^L\int_A \left(\sigma_{xx}\,\varepsilon_{xx} + \sigma_{xz}\gamma_{xz}\right)dA\,dx$$

$$= \frac{1}{2}\int_0^L\int_A \left[\sigma_{xx} z\frac{\partial \Phi}{\partial \mathrm{x}} + \sigma_{xz}\left(-\Phi + \frac{\partial \mathrm{w}}{\partial \mathrm{x}}\right)\right]dA\,dx = \frac{1}{2}\int_0^L M\frac{\partial \Phi}{\partial x} + Q\left(-\Phi + \frac{\partial \mathrm{w}}{\partial \mathrm{x}}\right)dx \tag{A.3}$$

$$\text{Kinetic energy } T\text{: } = \frac{1}{2}\int_0^L \left[\rho A\left(\frac{\partial w}{\partial t}\right)^2 + \rho I\left(\frac{\partial \Phi}{\partial t}\right)^2\right]dx \tag{A.4}$$

By Hamilton's principle, $\int_{t_1}^{t_2}\delta\left(T - U\right)dt = 0$

$$\Rightarrow \int_{t_1}^{t_2}\int_{0}^{L}\left[\rho A\left(\frac{\partial w}{\partial t}\right)\delta\left(\frac{\partial w}{\partial t}\right)+\rho I\left(\frac{\partial \Phi}{\partial t}\right)\delta\left(\frac{\partial \Phi}{\partial t}\right)-M\frac{\partial \delta\Phi}{\partial x}-Q\left(-\delta\Phi+\frac{\partial \delta \mathrm{w}}{\partial \mathrm{x}}\right)\right]dx\,dt=0$$

Integrating by parts, and noting that:

$$\delta w(x,t_1)=\delta w(x,t_2)=\delta\Phi(x,t_1)=\delta\Phi(x,t_2)=0\,,\Rightarrow$$

$$\int_{t_1}^{t_2}\left\{\int_{0}^{L}\left[\left(\frac{\partial M}{\partial x}+Q-\rho I\left(\frac{\partial^2\Phi}{\partial t^2}\right)\right)\delta\Phi+\left(\frac{\partial Q}{\partial x}-\rho A\frac{\partial^2 w}{\partial t^2}\right)\delta w\right]dx-\left[M\,\delta\Phi\right]_0^L-\left[Q\,\delta w\right]_0^L\right\}dt=0\,,$$

δw and $\delta\Phi$ are arbitrary, except where the geometric boundary conditions are prescribed, where they are zero.

$$\Rightarrow \frac{\partial M}{\partial x}=-Q+\rho I\left(\frac{\partial^2\Phi}{\partial t^2}\right) \text{ and } \frac{\partial Q}{\partial x}=\rho A\frac{\partial^2 w}{\partial t^2} \tag{A.5}$$

From constitute relations,

$$\sigma_{xx}=E\dot{o}_{xx} \text{ and } \sigma_{xz}=kG\gamma_{xz} \tag{A.6}$$

$$\text{Multiply (A6a) by } z\,dA\text{, and integrate} \Rightarrow M=E\,I\frac{\partial\Phi}{\partial x} \tag{A.7}$$

$$\text{Multiply (A6b) by } dA\text{, and integrate} \Rightarrow Q=k\,G\,A\left(-\Phi+\frac{\partial w}{\partial x}\right) \tag{A.8}$$

The two governing equations now become:

$$E I \frac{\partial^2 \Phi}{\partial x^2} + k G A\left(-\Phi + \frac{\partial w}{\partial x}\right) - \rho I\left(\frac{\partial^2 \Phi}{\partial t^2}\right) = 0 \tag{A.9}$$

$$k G A\left(-\frac{\partial \Phi}{\partial x} + \frac{\partial^2 w}{\partial x^2}\right) - \rho A\left(\frac{\partial^2 \Phi}{\partial t^2}\right) = 0 \tag{A.10}$$

Assuming harmonic time solutions, $w(x,t) = \tilde{w}(x)e^{i\omega t}$ and $\Phi(x,t) = \tilde{\Phi}(x)e^{i\omega t}$,

$$\text{(A9) becomes: } E I \frac{\partial^2 \tilde{\Phi}}{\partial x^2} + k G A\left(-\tilde{\Phi} + \frac{\partial \tilde{w}}{\partial x}\right) + \rho I \omega^2 \tilde{\Phi} = 0 \tag{A.11}$$

$$\text{(A10) becomes: } k G A\left(-\frac{\partial \tilde{\Phi}}{\partial x} + \frac{\partial^2 \tilde{w}}{\partial x^2}\right) + \rho A \omega^2 \tilde{w} = 0 \tag{A.12}$$

Let $\bar{x} = \frac{x}{L}$ and $\bar{w} = \frac{\tilde{w}}{L}$, where $\bar{x}$ and $\bar{w}$ belongs to [0,1] and define dimensionless constant, $\lambda = \frac{\rho A L^4 \omega^2}{E I}$, $\Omega = \frac{E I}{k G A L^2}$, and $\xi = \frac{A L^2}{I}$. *Note that* λ is proportional to $\left(\frac{L}{d}\right)^2 L^2$, while Ω and ξ are proportional to $1/\left(\frac{L}{d}\right)^2$ and $\left(\frac{L}{d}\right)^2$, respectively.

$$\text{(A11) becomes: } \frac{E I}{L^2} \frac{\partial^2 \tilde{\Phi}}{\partial \bar{x}^2} + k G A\left(-\tilde{\Phi} + \frac{\partial \bar{w}}{\partial \bar{x}}\right) + \rho I \omega^2 \tilde{\Phi} = 0$$

$$\Rightarrow \Omega\frac{\partial^2\tilde{\Phi}}{\partial\bar{x}^2}+\left(-1+\frac{\lambda\Omega}{\xi}\right)\tilde{\Phi}+\frac{\partial\bar{w}}{\partial\bar{x}}=0 \qquad \text{(A.13)}$$

(A.12) becomes: $\frac{kGA}{L}\left(-\frac{\partial\tilde{\Phi}}{\partial\bar{x}}+\frac{\partial^2\bar{w}}{\partial\bar{x}^2}\right)+\rho A\omega^2 L\bar{w}=0 \Rightarrow \left(-\frac{\partial\tilde{\Phi}}{\partial\bar{x}}+\frac{\partial^2\bar{w}}{\partial\bar{x}^2}\right)+\lambda\Omega\bar{w}=0$ (A.14)

Decoupling the equations (A.13) and (A.14) to give the following 4th order differential equations,

$$\frac{\partial^4\bar{w}}{\partial\bar{x}^4}+\lambda\left(\Omega+\frac{1}{\xi}\right)\frac{\partial^2\bar{w}}{\partial\bar{x}^2}+\lambda\left(\frac{\lambda\Omega}{\xi}-1\right)\bar{w}=0 \qquad \text{(A.15)}$$

$$\text{and } \frac{\partial^4\tilde{\Phi}}{\partial\bar{x}^4}+\lambda\left(\Omega+\frac{1}{\xi}\right)\frac{\partial^2\tilde{\Phi}}{\partial\bar{x}^2}+\lambda\left(\frac{\lambda\Omega}{\xi}-1\right)\tilde{\Phi}=0 \qquad \text{(A.16)}$$

Consider (A.15), substitute $e^{n\bar{x}}$ for $\bar{w}$, and it becomes:

$$\Rightarrow n^4+\lambda\left(\Omega+\frac{1}{\xi}\right)n^2+\lambda\left(\frac{\lambda\Omega}{\xi}-1\right)=0$$

$$\Rightarrow n^2=\frac{1}{2}\left[-\lambda\left(\Omega+\frac{1}{\xi}\right)+\sqrt{\lambda^2\left(\Omega+\frac{1}{\xi}\right)^2-4\lambda\left(\frac{\lambda\Omega}{\xi}-1\right)}\right]$$

$$\text{or } \frac{1}{2}\left[-\lambda\left(\Omega+\frac{1}{\xi}\right)-\sqrt{\lambda^2\left(\Omega+\frac{1}{\xi}\right)^2-4\lambda\left(\frac{\lambda\Omega}{\xi}-1\right)}\right] \qquad \text{(A.17)}$$

Assume $\frac{\lambda\Omega}{\xi}<1$, i.e. $\omega^2<\frac{kGA}{\rho I}$. The solutions to Timoshenko beam become:

$$\bar{w} = C_1 \cosh\left(\alpha \bar{x}\right) + C_2 \sinh\left(\alpha \bar{x}\right) + C_3 \cos\left(\beta \bar{x}\right) + C_4 \sin\left(\beta \bar{x}\right) \tag{A.18}$$

$$\tilde{\Phi} = D_1 \sinh\left(\alpha \bar{x}\right) + D_2 \cosh\left(\alpha \bar{x}\right) + D_3 \sin\left(\beta \bar{x}\right) + D_4 \cos\left(\beta \bar{x}\right) \tag{A.19}$$

$$\text{where } \alpha = \sqrt{\frac{1}{2}\left[-\lambda\left(\Omega + \frac{1}{\xi}\right) + \sqrt{\lambda^2\left(\Omega + \frac{1}{\xi}\right)^2 - 4\lambda\left(\frac{\lambda\Omega}{\xi} - 1\right)}\right]} \tag{A.20}$$

$$\beta = \sqrt{\frac{1}{2}\left[-\lambda\left(\Omega + \frac{1}{\xi}\right) - \sqrt{\lambda^2\left(\Omega + \frac{1}{\xi}\right)^2 - 4\lambda\left(\frac{\lambda\Omega}{\xi} - 1\right)}\right]} \tag{A.21}$$

Substitute (A.18), (A.19) into (A.13) or (A.14), the coefficient relations are:

$$D_1 = C_1\psi_\alpha,\ D_2 = C_2\psi_\alpha,\ D_3 = C_3\psi_\beta, \text{ and } D_4 = -C_4\psi_\beta \tag{A.22}$$

$$\text{where } \psi_\alpha = \frac{\alpha^2 + \lambda\Omega}{\alpha} \text{ and } \psi_\beta = \frac{\beta^2 + \lambda\Omega}{\beta}$$

Finally, define the soil-structure interaction boundary conditions,

$$\text{At } \bar{x} = 0:\ kGA\left(-\tilde{\Phi} + \frac{\partial \bar{w}}{\partial \bar{x}}\right) - K_T \bar{w} = 0 \text{ and } EI\frac{\partial \tilde{\Phi}}{\partial \bar{x}} - K_R\tilde{\Phi} = 0 \tag{A.23}$$

$$\text{At } \bar{x} = 1:\ \bar{M} = \frac{M}{EI} = \frac{\partial \tilde{\Phi}}{\partial \bar{x}} = 0 \text{ and } \bar{Q} = \frac{Q}{kGA} = -\tilde{\Phi} + \frac{\partial \bar{w}}{\partial \bar{x}} = 0 \tag{A24}$$

Substitute (A.18) and (A.19) into (A.23) and (A.24), the coefficients of response solutions are obtained as follow,

$$\begin{bmatrix} -K_T & kGA(\alpha-\psi_\alpha) & -K_T & kGA(\beta-\psi_\beta) \\ EI\alpha\psi_\alpha & -K_R\psi_\alpha & EI\beta\psi_\beta & K_R\psi_\beta \\ \alpha\psi_\alpha\cosh(\alpha) & \alpha\psi_\alpha\sinh(\alpha) & \beta\psi_\beta\cos(\beta) & \beta\psi_\beta\sin(\beta) \\ (\alpha-\psi_\alpha)\sinh(\alpha) & (\alpha-\psi_\alpha)\cosh(\alpha) & -(\beta+\psi_\beta)\sin(\beta) & (\beta+\psi_\beta)\cos(\beta) \end{bmatrix} \begin{pmatrix} C_1 \\ C_2 \\ C_3 \\ C_4 \end{pmatrix} = 0$$

(A.25)

And the characteristic equation is:

$$\begin{vmatrix} -K_T & kGA(\alpha-\psi_\alpha) & -K_T & kGA(\beta-\psi_\beta) \\ EI\alpha\psi_\alpha & -K_R\psi_\alpha & EI\beta\psi_\beta & K_R\psi_\beta \\ \alpha\psi_\alpha\cosh(\alpha) & \alpha\psi_\alpha\sinh(\alpha) & \beta\psi_\beta\cos(\beta) & \beta\psi_\beta\sin(\beta) \\ (\alpha-\psi_\alpha)\sinh(\alpha) & (\alpha-\psi_\alpha)\cosh(\alpha) & -(\beta+\psi_\beta)\sin(\beta) & (\beta+\psi_\beta)\cos(\beta) \end{vmatrix} = 0 \quad \text{(A.26)}$$

Characteristic equation (A.26) is used to solve for natural frequencies ω, which are hidden in the variables α, β, ψ_α, and ψ_β. Once the natural frequencies are obtained, corresponding values of α, β, ψ_α, and ψ_β are put into equation (A.25) to solve for coefficients C_1, C_2, C_3, and C_4 in that mode. Finally, mode shapes are obtained from equation (A.18) using the corresponding coefficients.

Appendix B

EARTHQUAKE DATA

Table B.1: Earthquake records used in Section 5.2.6.

Earthquake No.	Location	Magnitude	Earthquake No.	Location	Magnitude	Earthquake No.	Location	Magnitude
1	Livermore	5.9	25	Willow Creek	5.4	49	Morgan Hill Area	4.1
2	Livermore	5.8	26	Loma Linda	3.6	50	San Leandro	3.6
3	Morgan Hill	6.2	27	Chino Hills	5.4	51	Newhall	4.1
4	Mt. Lewis	5.8	28	Trinidad	4.6	52	Beaumont	3.85
5	Palm Springs	6	29	Alamo	4	53	Berkeley	4
6	Whittier	5.9	30	Yucaipa	3.8	54	Ontario	3.6
7	Loma Prieta	6.9	31	Petrolia Offshore	4.9	55	El Cerrito	4
8	Sierra Madre	5.6	32	San Bernardino	4.45	56	Devore	3.82
9	Landers	7.3	33	Morgan Hill Area	4.3	57	Yorba Linda	4.06
10	Big Bear	6.5	34	Inglewood Area	4.7			
11	Northridge	6.7	35	Calexico Area	5.8			
12	Hector Mine	7.1	36	Milpitas Area	4.1			
13	Beverly Hills	4.2	37	Ferndale Area	6.5			
14	Gilroy	4.9	38	Banning Area	3.89			
15	Big Bear City	5.2	39	Beaumont Area	3.86			
16	Anza	5.2	40	Ferndale Area	5.9			
17	Crescent City	7.2	41	Barstow Area	5.1			
18	Piedmont	3.6	42	Redlands	3.87			
19	Ferndale offshore	5.4	43	Whittier Narrows	4.14			
20	Lafayette	4.2	44	Calexico Area	7.2			
21	Trinidad	5	45	Ocotillo Area	4.5			
22	Piedmont Area	4.2	46	Borrego Springs	4.43			
23	Chatsworth	4.4	47	Ocotillo Area	5.72			
24	Alum Rock Area	5.4	48	Borrego Springs	5.43			

Table B.2: The seismic records for the following buildings are used in Section 5.2.6. The records are extracted from the California Strong Motion Instrumentation Program (CSMIP) database (http://www.strongmotioncenter.org/).

Building No	Material	No. of Stories Above Ground	Design Year	Usage	Location	Structural model parameters (see text)	
						Fundamental period T_1	Lateral stiffness ratio α_0
1	Concrete	4	1974	Office	Palm Desert	0.6	1
2	Concrete	11	1971	Hospital	Newport Beach	0.76	1
3	Steel	14	1985	Office	El Segundo	1.93	3.125
4	Concrete	5	1968	Library	San Bernardino	0.5	1
5	Concrete	6	1970	Hotel	San Bernardino	0.42	1
6	Steel	5	1986	Hospital	San Bernardino	0.48	12.5
7	Concrete	13	1964	Commercial	Sherman Oaks	1.54	12.5
8	Steel	6	1976	Commercial	Burbank	1.13	12.5
9	Concrete	10	1974	Residential	Burbank	0.53	1
10	Concrete	7	1965	Hotel	Van Nuys	0.44	12.5
11	Concrete	5	1970	Warehouse	Los Angeles	1.2	12.5
12	Concrete	20	1967	Hotel	North Hollywood	2.05	12.5
13	Concrete	8	1967	Administrative	Los Angeles	1.33	1
14	Steel	12	1971	Commerce/Office	Pasadena	2.47	12.5
15	Steel	12	1971	Office	Pasadena	2.3	12.5
16	Concrete	9	1963	Commercial	Pasadena	1.52	12.5
17	Concrete	17	1980	Residential	Los Angeles	1.1	1
18	Steel	52	1988-90	Office	Los Angeles	1.75	3.125
19	Steel	5	1986	Hospital	Lancaster	0.72	12.5
20	Steel	54	1988	Office	Los Angeles	5.5	3.125
21	Steel	6	1988	Univ. Office	Los Angeles	0.8	3.125
22	Concrete	10	1964	Commercial	San Jose	0.93	12.5
23	Concrete	10	1971	Residential	San Jose	0.69	1
24	Steel	13	1972	Gov. Office	San Jose	1.84	12.5
25	Steel	5	1979	Hospital	San Jose	0.63	12.5
26	Concrete	10	1970	Commercial	Walnut Creek	0.78	3.125
27	Concrete	6	1966	Office	Hayward	0.66	1
28	Concrete	24	1964	Residential	Oakland	1.84	1
29	Concrete	4	1978	Hospital	Eureka	0.27	1